

Collisionless and Collisional Dynamics in Astrophysics

A dissertation submitted to

ETH Zurich

for the degree of

Doctor of Sciences

presented by

Marcel Zemp

Dipl. phys. ETH Zurich

born June 7, 1977

citizen of

Risch (ZG) and Escholzmatt (LU)

accepted on the recommendation of

Prof. Dr. C. Marcella Carollo, examiner

Prof. Dr. Ben Moore, co-examiner

Prof. Dr. George Lake, co-examiner

2006

Contents

Kurzfassung	ix
Abstract	xi
1 General introduction	1
1.1 Overview	1
1.2 Self-gravitating systems	2
1.2.1 Long range nature of gravity	2
1.2.2 Equations of motion	2
1.2.3 Collisionless versus collisional	3
1.2.4 Distribution function and Boltzmann equations	4
1.3 Numerical methods	5
1.3.1 Monte-Carlo methods	5
1.3.2 Dynamical evolution and symplectic integrators	7
1.3.3 Choice of time-steps	8
1.3.4 Acceleration calculation	8
1.3.5 PKDGRAV	15
1.4 Unifying both regimes	16
1.5 Content of this thesis	18
2 Multi-mass halo models	21
2.1 Introduction and motivation	21
2.2 Method	23
2.3 Tests	25
2.3.1 Two-shell models	25
2.3.2 Three-shell models	30
2.4 Preservation of cusp slope	32
2.5 Conclusions	35
3 An optimum time-stepping scheme	37
3.1 Introduction	37
3.2 Dynamical time-stepping	38
3.2.1 General idea and description	38
3.2.2 Implementation within a tree-code	39
3.3 Time-stepping criterion tests and behaviour	44
3.3.1 General properties	44
3.3.2 Elliptic 2-body orbits	48

3.3.3	Hyperbolic 2-body orbits	52
3.3.4	Cosmological structure formation	54
3.3.5	Dependence on parameters	56
3.3.6	Efficiency	57
3.4	Conclusions	61
4	Applications	65
4.1	Cusps in cold dark matter haloes	65
4.1.1	Introduction	65
4.1.2	Numerical methods	67
4.1.3	Results	68
4.2	Does the Fornax dwarf spheroidal have a central cusp or core?	74
4.2.1	Introduction	74
4.2.2	Numerical methods	75
4.2.3	Results	76
5	Summary and perspective	81
	Appendix	85
A	Hamiltonian formalism	87
B	Further projects	91
B.1	A universal velocity distribution of relaxed collisionless structures	91
B.1.1	Introduction	91
B.1.2	Numerical methods and results	91
B.2	Globular clusters, satellite galaxies and stellar haloes from early dark matter peaks	95
B.2.1	Introduction	95
B.2.2	The first stellar systems	96
B.2.3	Connection to globular clusters and halo stars	98
B.2.4	Connection to satellite galaxies and the missing satellites problem	100
	Bibliography	103
	Curriculum vitae	119
	Publications	121
	Acknowledgment	123

List of Figures

1.1	Comparison of a symplectic and a non-symplectic integrator	9
1.2	Compensating softening kernels	12
1.3	Geometrical configuration for multipole expansion	13
1.4	Quad-tree	15
1.5	Positions and orbital fits for seven stars in the Galactic centre	17
2.1	Mean particle separation function	22
2.2	Multi-mass stability tests: density profiles	26
2.3	Multi-mass stability tests: anisotropy profiles	28
2.4	Computer run time versus mass ratio	29
2.5	Three-shell multi-mass model	31
2.6	Equal profile mergers after 10 Gyr	33
2.7	Cusp-core merger after 10 Gyr	34
3.1	Viewing cone for add-up scheme	42
3.2	Time-step distribution for different density profiles	46
3.3	2-body orbits with different eccentricities	49
3.4	2-body orbits with eccentricity $e = 0.9$	50
3.5	Orbit of run p)	51
3.6	Orbit of run I)	52
3.7	Orbits of run J) and K)	53
3.8	Virgo cluster: density profiles	55
3.9	Virgo cluster: substructure mass function	56
3.10	Number of force evaluations	59
4.1	Logarithmic slope of the density profile of run DM25	69
4.2	Logarithmic slope of the density profile of run D5, DM25 and DM50	70
4.3	Density profiles in physical coordinates	72
4.4	Logarithmic slope of the extrapolated DM50 density profile	73
4.5	Radial distance of a single globular cluster from the centre of its host halo	77
4.6	Globular clusters in cuspy halo	79
4.7	Globular clusters in cored halo	80
B.1	Radial velocity distribution function	93
B.2	Tangential velocity distribution function	94
B.3	Galaxy at redshift $z = 12$ and $z = 0$	97

List of Figures

B.4	Radial distribution of old stellar systems compared with rare peaks within a $z = 0$ Λ CDM galaxy	99
-----	--	----

List of Tables

2.1	Summary of parameters for the different models	27
2.2	Summary of parameters for the two initial conditions used for the mergers	32
3.1	Number of force evaluations	60
3.2	Summary of elliptic 2-body orbit runs a) - p)	62
3.3	Summary of hyperbolic 2-body orbit runs A) - K)	63
4.1	Summary of cluster models	67

List of Tables

Kurzfassung

In dieser Doktorarbeit werden Methoden entwickelt, um astrophysikalische Prozesse zu studieren, welche Dynamik mit und ohne Kollisionen beinhaltet. Die Hauptanwendung, für die diese Methoden entwickelt wurden, ist das Studium von dynamischen Effekten, die bei Galaxien-Verschmelzungen mit super-massiven Schwarzen Löchern in den Zentren der jeweiligen Galaxien entstehen. Dies ist eine schwierige Problemstellung um mit N-body Methoden zu untersuchen, denn es enthält sowohl kollisionsfreie Dynamik als auch Dynamik mit Kollisionen. Ebenso müssen ein enormer Bereich in Raum und Zeit aufgelöst werden, um die wahren physikalischen Effekte zu sehen wenn man nicht numerischen Artefakten wie Relaxation in N-body Simulationen erliegen will.

In einer allgemeinen Einleitung 1 werden zuerst die physikalischen Grundlagen von selbst-gravitierenden Systemen diskutiert und eine kleine Übersicht über die heutzutage verwendeten numerischen Methoden gegeben.

In Kapitel 2 wird eine simple Methode (Multi-Massen-Technik) präsentiert, um Modelle von Halo-Profilen mit verschiedenen Massen und Auflösung zu generieren. Mit dieser Methode wird die Computer Laufzeit in Simulationen gegenüber Modellen mit nur einer fixen Auflösung drastisch reduziert. Dies erlaubt bei einer gegebenen Computer Laufzeit viel kleinere Skalen zu untersuchen. Als Anwendung bestätigen wir die Aussage von Dehnen [31], dass in Verschmelzungen von dunkle Materie Halos immer das steilste zentrale Profil eines Vorgängers erhalten bleibt. Für diese Anwendung werden hoch auflösende N-body Simulationen benötigt, wobei wir jeden in der Verschmelzung beteiligten Vorgänger mit ungefähr 5×10^7 Teilchen auflösen.

Als eine bedeutende neue Entwicklung wird in Kapitel 3 ein Zeit-Schritt Kriterium für N-body Simulationen präsentiert, das auf der wahren dynamischen Zeit eines Teilchens basiert. Dieses Kriterium erlaubt der jeweiligen Bahn eines Teilchens in allen Umgebungen korrekt zu folgen, da das Kriterium eine bessere Anpassungsfähigkeit als vorherige Kriterien hat. Zusätzlich wird eine kleinere Anzahl von Berechnungen der Kraft in Regionen mit einer kleineren Dichte benötigt und die Methode hängt nicht direkt von artifiziellen Parametern wie zum Beispiel der Softening-Länge ab. Daher kann diese Methode mehrere Größenordnungen schneller sein als konventionellen Methoden, welche zum Beispiel eine Kombination von Beschleunigung und Softening-Länge als Kriterium benutzen. Das neue Kriterium ist daher ideal um schwierige Probleme zu lösen, wie zum Beispiel die Dynamik in Zentren von dunklen Materie Halos zu studieren. Ebenso wird eine Exzentrizitätskorrektur für ein Leapfrog Integrationsschema hergeleitet, welches erlaubt Zweikörperinteraktionen mit Exzentrizität $e \rightarrow 1$ mit grosser Präzision zu verfolgen. Diese Neuentwicklung erlaubt es, einen grossen Bereich von Problemen zu studieren, welche Kollisionen enthalten als auch kollisionsfrei sind. Es werden Tests dieses neuen Schemas in N-body Simulationen von Zweikörperproblemen mit Exzen-

trizität $e \rightarrow 1$ (elliptisch und hyperbolisch), Gleichgewichts-Halo-Profilen und von kosmologischen Strukturbildungs-Simulationen präsentiert.

In Kapitel 4 werden die ersten Anwendungen dieser Neuentwicklungen präsentiert. In der ersten Anwendung wurde die Multi-Massen-Technik dazu verwendet in einer kosmologischen Simulation das Dichteprofil eines Galaxienhaufens bis runter zu einem Promille des virial Radius zu bestimmen. Das innere Profile des Galaxienhaufens wird gut durch ein Potenzgesetz der Form $\rho(r) \propto r^{-\gamma}$ beschrieben wobei $\gamma = 1.2$. Eine weitere Anwendung der Multi-Massen-Technik war der Test einer potentiellen Erklärung für die Position von fünf Globular Clusters bei der ungefähren Distanz von 1 kpc vom Zentrum der Zwerggalaxie Fornax. In einer Kosmologie mit dunkler Materie und dunkler Energie als Hauptbestandteile würden diese Globular Clusters innerhalb von ein paar Milliarden Jahren von der heutigen Position ins Zentrum sinken. Eine mögliche Lösung hierfür wäre, dass das dunkle Materie Halo der Fornax Zwerggalaxie einen Kern mit konstanter Dichte hat, denn in einem Kern konstanter Dichte wird die Zeit, die für ein Sinken zum Zentrum benötigt wird, viel länger als die Hubble-Zeit und die Globular Clusters bleiben beim Kernradius stehen. Um diese Hypothese zu testen waren hoch auflösende Modelle von dunkle Materie Halos nötig.

Zum Schluss wird eine Zusammenfassung präsentiert und ein Ausblick auf weitere Projekte in der Zukunft gegeben.

Abstract

This thesis develops numerical methods in order to study astrophysical processes that include collisionless and collisional dynamics. As a major application that involves such processes, the dynamical effects of merging galaxies with super-massive black holes in their centres were in mind when these methods were developed. This is a very difficult problem to simulate with N-body methods since it demands a combination of collisionless and collisional dynamics. It also involves an enormous spatial and temporal range in order to observe the real physical effects and not suffer from numerical artefacts like relaxation in the N-body simulations.

In a general introduction 1, we first discuss the basic physics of self-gravitating systems and present a short overview of some of the numerical methods used in the field of computational astrophysics today.

We then present in chapter 2 a simple way to model halo profiles with a multi-mass technique. This technique reduces the computer run time that would be needed by a single-mass model resolving the same scales by several factors and therefore allows to resolve smaller scales in N-body simulations for a given computer run time. As an application, we test and confirm the prediction by Dehnen [31], that in mergers of dark matter haloes always the cusp of the steepest progenitor of the merger is preserved. This application required high resolution N-body simulations where we model each merger progenitor with an effective number of particles of approximately 5×10^7 particles.

As a major new development, we present in chapter 3 a new time-stepping criterion for N-body simulations that is based on the true dynamical time of a particle. This allows us to follow the orbits of particles correctly in all environments since it has better adaptivity than previous time-stepping criteria used in N-body simulations. Furthermore, it requires far fewer force evaluations in low density regions of the simulation and has no dependence on artificial parameters such as, for example, the softening length. This can be orders of magnitude faster than conventional ad-hoc methods that employ combinations of acceleration and softening and is ideally suited for hard problems, such as obtaining the correct dynamics in the very central regions of dark matter haloes. We also derive an eccentricity correction for a general leapfrog integration scheme that can follow gravitational scattering events for orbits with eccentricity $e \rightarrow 1$ with high precision. These new approaches allow us to study a range of problems in collisionless and collisional dynamics from few-body problems to cosmological structure formation. We present tests of the time-stepping scheme in N-body simulations of 2-body orbits with eccentricity $e \rightarrow 1$ (elliptic and hyperbolic), equilibrium haloes and a hierarchical cosmological structure formation run.

In chapter 4, we present the first applications of these new developments that already led to new insights and physical results. In one application, the multi-mass technique

was used in a cosmological structure formation run in order to resolve the resulting density profile of a high resolution cluster down to one per mill of the virial radius. The inner density profile of this cluster halo is well fit by a power law $\rho(r) \propto r^{-\gamma}$ down to the smallest resolved scale with $\gamma = 1.2$. This means that the dark matter profiles still obey a power law scaling down to one per mill of the virial radius. Another application of the multi-mass models was to test a potential explanation of the presence of the five globular clusters at approximately 1 kpc distance from the centre of the Fornax dwarf spheroidal galaxy. In a cuspy cold dark matter halo as predicted from large scale structure formation simulations in a lambda cold dark matter (Λ CDM) cosmology, the globulars would sink to the centre from their current positions within a few Gyr, presenting a puzzle as to why they survive at their present positions. A possible solution to this timing problem is to adopt a cored dark matter halo for the Fornax dwarf spheroidal. In a cored dark matter halo, the sinking time becomes many Hubble times and the globular clusters effectively stall at the dark matter core radius. In order to perform these simulations and test this hypothesis, high resolution multi-mass models were needed to obtain the required spatial resolution.

Finally, we summarise and give a perspective on future projects in chapter 5.

Chapter 1

General introduction

1.1 Overview

In astrophysics, a variety of self-gravitating systems exist. Such systems range from the Keplerian 2-body system, the stability of the solar system, core collapse in globular clusters, galaxy mergers up to the formation process of large scale structure in the universe. Computational methods like N-body simulations are a powerful tool to study such self-gravitating systems. The ultimate goal would be to study the evolution of the universe from early initial conditions after the big bang until the present with all the relevant physics involved but the available computer resources have so far allowed only the study of certain aspects of the full picture.

Hence, two communities emerged out of this. The first concentrated on small astrophysical systems like star clusters where time-scales are short and the dynamics of the system is mainly collisional. In contrast, the long-term and large scale structure formation, that is governed by the dynamical evolution of collisionless dark matter particles, is the working field of the other community. Both communities developed their own methods and specific techniques in order to treat the individual numerical problems optimally.

But many systems in astrophysics can not be fully described by only one regime. For example, the dynamics of super-massive black holes in the centre of a galaxy-galaxy merger remnant is dominated by collisional dynamics whereas the large scale shape of the resulting structure is a result of the collisionless dynamics of the dark matter. With the ever increasing computer resources, a combination of these two regimes becomes feasible. This thesis project had therefore the aim to develop the numerical techniques in order to perform N-body simulations that include collisionless as well as collisional dynamics.

This chapter gives the reader an introduction to the basic physics of self-gravitating systems and a short overview of some of the numerical methods used in the field of computational astrophysics today. A more detailed motivation for combining the collisionless and collisional regime is given towards the end of the introduction.

1.2 Self-gravitating systems

1.2.1 Long range nature of gravity

The nature of the gravity force makes a self-gravitating system behave completely different than for example a neutral gas. Generally, the electromagnetic forces between two gas molecules are small since the gas is neutral on large scales. As a consequence the molecules move at nearly constant speed for long periods until they collide with another molecule where they feel a strong acceleration due to the close interaction. Thus, only forces on short length scales that arise from collisions are important and we can neglect long range forces since the gas is neutral and the two different electromagnetic charges compensate on these scales.

In contrast, gravity is always attractive since there is only one charge in gravity; there is only positive mass as far as we know. Let's consider a homogeneous system with density ρ . The force from a cone segment on a particle at its apex with mass dm_C at distance r with thickness dr and solid angle $d\Omega$ around the particle is given by

$$dm_C = \rho r^2 dr d\Omega . \quad (1.1)$$

Therefore, the contribution from this cone segment to the total force on that particle results in

$$dF = G \frac{m dm_C}{r^2} = G m \rho dr d\Omega . \quad (1.2)$$

For a homogeneous system, the force per unit length dF/dr from that cone segment is therefore independent of radius and force contributions arising from all scales are important. Of course, if the system is perfectly spherical around the particle and homogeneous, no net force will act on the particle. But inhomogeneities on all scales can result in a net force on any particle.

1.2.2 Equations of motion

Let's assume a self-gravitating system is described by a smooth distribution of mass given by the density $\rho(\mathbf{x}', t)$ and our goal is to calculate the acceleration on a particle at a position \mathbf{x} . By Newton's inverse-square law, we can express the total acceleration by integrating over the whole volume and obtain

$$\mathbf{a}(\mathbf{x}, t) = G \int \frac{\mathbf{x}' - \mathbf{x}}{|\mathbf{x}' - \mathbf{x}|^3} \rho(\mathbf{x}', t) d^3 \mathbf{x}' . \quad (1.3)$$

Here, G is Newton's constant of gravity. We can define a scalar function $\Phi(\mathbf{x}, t)$ by

$$\Phi(\mathbf{x}, t) \equiv -G \int \frac{\rho(\mathbf{x}', t)}{|\mathbf{x}' - \mathbf{x}|} d^3 \mathbf{x}' . \quad (1.4)$$

This function $\Phi(\mathbf{x}, t)$ is called the gravitational potential and with

$$\nabla \left(\frac{1}{|\mathbf{x}' - \mathbf{x}|} \right) = \frac{\mathbf{x}' - \mathbf{x}}{|\mathbf{x}' - \mathbf{x}|^3} , \quad (1.5)$$

we find

$$\mathbf{a}(\mathbf{x}, t) = -\nabla\Phi(\mathbf{x}, t) . \quad (1.6)$$

Here, the gradient operator ∇ is always meant with respect to \mathbf{x} .

With

$$\nabla \left(\frac{\mathbf{x}' - \mathbf{x}}{|\mathbf{x}' - \mathbf{x}|^3} \right) = \nabla^2 \left(\frac{1}{|\mathbf{x}' - \mathbf{x}|} \right) = -4\pi\delta(\mathbf{x}' - \mathbf{x}) , \quad (1.7)$$

where $\delta(\mathbf{x}' - \mathbf{x})$ is the Dirac delta-function we can now write

$$\nabla \mathbf{a}(\mathbf{x}, t) = G \int (-4\pi\delta(\mathbf{x}' - \mathbf{x})) \rho(\mathbf{x}', t) d^3\mathbf{x}' = -4\pi G \rho(\mathbf{x}, t) . \quad (1.8)$$

By substituting from equation (1.6), we get the Poisson equation

$$\nabla^2\Phi(\mathbf{x}, t) = 4\pi G \rho(\mathbf{x}, t) . \quad (1.9)$$

The equations of motion are now given by

$$\dot{\mathbf{x}}(\mathbf{x}, t) = \mathbf{v}(\mathbf{x}, t) \quad (1.10)$$

$$\ddot{\mathbf{x}}(\mathbf{x}, t) = \dot{\mathbf{v}}(\mathbf{x}, t) = \mathbf{a}(\mathbf{x}, t) = -\nabla\Phi(\mathbf{x}, t) \quad (1.11)$$

$$\nabla^2\Phi(\mathbf{x}, t) = 4\pi G \rho(\mathbf{x}, t) . \quad (1.12)$$

In order to calculate the trajectory $\mathbf{x}(t)$ of the particle, this system of coupled second-order differential equations in space and time has to be solved. Generally, this can only be solved with numerical methods for an arbitrary configuration $\rho(\mathbf{x}, t)$.

1.2.3 Collisionless versus collisional

Of course, real astrophysical systems are not perfectly smooth but they consist of discrete particles like stars, black holes or dark matter particles that mutually interact via gravity. The relaxation is a measure for the effect that a particle is not moving in a smooth potential but through a potential that is generated by the discrete configuration of the individual particles in the system. Since each individual particle is slightly perturbed by the mutual interactions with all the other particles, its velocity will deviate from the value it would have in a smooth potential due to the discreteness of the system.

As a measure for the speed of this relaxation process, we define the relaxation time T_{relax} by the time where the change of the velocity is of order of the velocity itself, which results in

$$T_{\text{relax}} = \frac{N}{8 \ln \Lambda} T_{\text{cross}} , \quad (1.13)$$

where T_{cross} is the crossing time needed for the particle to cross the system and

$$\ln \Lambda \equiv \ln \left(\frac{b_{\text{max}}}{b_{\text{min}}} \right) \quad (1.14)$$

is called the Coulomb logarithm and b_{max} respectively b_{min} are the minimum respectively maximum impact parameters of the particle under consideration. T_{relax} is the time-scale where the system loses its memory of its initial state.

For galaxies with $N \approx 10^{11}$ stars and an age of approximately 10 Gyr (which corresponds to a few hundred crossing times), the relaxation time-scale for the whole system is much longer than the age of the universe and close encounters are entirely unimportant. Also for dark matter haloes relaxation is completely negligible. If dark matter consists of neutralinos then their expected mass is of order of a few hundred GeV/c² [44] which corresponds to a total number of $N \approx O(10^{67})$ particles within a Milky Way size dark matter halo ($1 \text{ GeV/c}^2 = 8.963 \times 10^{-58} \text{ M}_\odot^1$).

On the other hand, for globular clusters with $N \approx 10^5$ stars and a crossing time of $T_{\text{cross}} \approx 10^5 \text{ yr}$, the relaxation process can be important over the cluster lifetime of approximately 10 Gyr. This is especially true in the centre of the globular cluster where the local relaxation time-scale is much smaller and can lead to core collapse.

In summary, self-gravitating systems with a relaxation time-scale much longer than the time interval of interest (which is at maximum the age of the universe) can be called collisionless. Systems with a (local) relaxation time of the order of the time interval of interest are called collisional, i.e. close particle encounters play an important role.² Also if the smoothness of the potential breaks down and local fluctuations, arising from a few particles like e.g. super-massive black holes, dominate the dynamics, the interactions have to be treated in the collisional regime.

1.2.4 Distribution function and Boltzmann equations

We can generalize the description of a self-gravitating system by introducing the distribution function or phase-space density $f(\mathbf{x}, \mathbf{v}, t)$ where $f(\mathbf{x}, \mathbf{v}, t)d^3\mathbf{x}d^3\mathbf{v}$ is the mass in the phase-space volume $d^3\mathbf{x}d^3\mathbf{v}$ at the phase-space point (\mathbf{x}, \mathbf{v}) at time t .

If we know the configuration at a time t_0 , either by $\rho(\mathbf{x}, t_0)$ and the velocity field or by $f(\mathbf{x}, \mathbf{v}, t_0)$, the equations of motion allow us to calculate the state of the system at any later time. Hence, we're interested in the flow of the points in phase-space. We can generalise the coordinates in phase-space by introducing a new coordinate vector $\mathbf{w} \equiv (\mathbf{x}, \mathbf{v}) \equiv (w_1, \dots, w_6)$ and describe the velocity of this flow in phase-space by $\dot{\mathbf{w}} = (\dot{\mathbf{x}}, \dot{\mathbf{v}}) = (\mathbf{v}, -\nabla\Phi(\mathbf{x}, t))$.

In a collisionless system, this flow is mass conserving and therefore obeys a continuity equation

$$\frac{\partial f(\mathbf{w}, t)}{\partial t} + \sum_{i=1}^6 \frac{\partial (f(\mathbf{w}, t) \dot{w}_i)}{\partial w_i} = 0 . \quad (1.15)$$

By using Hamilton's equations

$$\dot{x}_i = \frac{\partial H(\mathbf{x}, \mathbf{v}, t)}{\partial v_i} \quad (1.16)$$

$$\dot{v}_i = -\frac{\partial H(\mathbf{x}, \mathbf{v}, t)}{\partial x_i} = -\frac{\partial \Phi(\mathbf{x}, t)}{\partial x_i} \quad (1.17)$$

¹ M_\odot stands for the mass of the Sun and is a standard mass unit in astrophysics. $\text{M}_\odot = 1.989 \times 10^{30} \text{ kg}$.

²Collisional does not mean real physical collisions; one should always think of close encounters here.

where the appropriate Hamiltonian³

$$H(\mathbf{x}, \mathbf{v}, t) \equiv \frac{1}{2}|\mathbf{v}|^2 + \Phi(\mathbf{x}, t) \quad (1.18)$$

describes the energy per unit mass, we can write

$$\sum_{i=1}^6 \frac{\partial \dot{w}_i}{\partial w_i} = \sum_{i=1}^3 \left(\frac{\partial \dot{x}_i}{\partial x_i} + \frac{\partial \dot{v}_i}{\partial v_i} \right) = \sum_{i=1}^3 \left(\frac{\partial}{\partial x_i} \left(\frac{\partial H}{\partial v_i} \right) - \frac{\partial}{\partial v_i} \left(\frac{\partial H}{\partial x_i} \right) \right) = 0 . \quad (1.19)$$

Therefore, the continuity equation simplifies to

$$\frac{\partial f(\mathbf{w}, t)}{\partial t} + \sum_{i=1}^6 \dot{w}_i \frac{\partial f(\mathbf{w}, t)}{\partial w_i} = \frac{df(\mathbf{w}, t)}{dt} = 0 . \quad (1.20)$$

The above equation (1.20) is called the collisionless Boltzmann equation and it describes the evolution of an incompressible fluid in phase-space that is evolved under a Hamiltonian flow. The collisionless Boltzmann equation is a special case of Liouville's theorem under the assumption that the number of particles is large $N \gg 1$ and we can neglect two-particle and higher order correlations. For further details and an explicit derivation see also Binney and Tremaine [15, chapter 8].

If collisions between particles are important in the astrophysical system under study, then the phase-space density around a particle will change and we have to modify the collisionless Boltzmann equation (1.20) by

$$\frac{df(\mathbf{w}, t)}{dt} = \frac{\partial f(\mathbf{w}, t)}{\partial t} + \sum_{i=1}^6 \dot{w}_i \frac{\partial f(\mathbf{w}, t)}{\partial w_i} = \Gamma(f(\mathbf{w}, t)) , \quad (1.21)$$

where $\Gamma(f(\mathbf{w}, t))$ is a collision term that describes the rate of change of $f(\mathbf{w}, t)$ due to particle encounters. Equation (1.21) is called the Boltzmann equation.

1.3 Numerical methods

1.3.1 Monte-Carlo methods

A very efficient method in order to solve the Boltzmann equations (1.20) and (1.21) (depending on whether the system is collisional or collisionless) together with the Poisson equation (1.9) are Monte-Carlo methods where one represents the astrophysical system under study with N bodies. Monte-Carlo methods can be loosely described as statistical simulation methods, where statistical simulation is defined in quite general terms to be

³This form of the Hamiltonian is only correct in the collisionless regime since it neglects possible interactions between particles. The correct interactions can only be described in the full $6N$ dimensional phase-space by the N -particle distribution function where the full Hamiltonian correctly describes the mutual interactions between the particles. For more details see also Binney and Tremaine [15, chapter 8]

any method that utilizes sequences of random numbers to perform a simulation. The method is named after the capital of the principality Monaco that is famous for being a centre for gambling and had its origin from research during the Manhattan project (development of the atomic bomb) of the second world war where such methods were used for a direct simulation of the probabilistic problems concerned with random neutron diffusion in fissile material.

The basic idea of Monte-Carlo methods can be illustrated by the following procedure that allows to calculate π in a Monte-Carlo fashion. Imagine a square with area $A_S = d^2$ and inscribed a circle with area $A_C = \left(\frac{d}{2}\right)^2 \pi = \frac{\pi}{4} A_S$. Now place N points randomly and independent within that square. By counting the number N_C which fall within the circle, we can express π as

$$\pi = 4 \frac{A_C}{A_S} = 4 \frac{N_C}{N} \quad (1.22)$$

since the probability that a point lies in a certain area is proportional to that area. Since the points are generated randomly and independent, this process follows Poisson statistics and the fractional error is of order $1/\sqrt{N}$. The big advantage in Monte-Carlo method is that the error does not depend on the number of dimensions of the problem but only on the number of points N . Therefore this method can outperform other methods in multi-dimensional problems.

In astrophysical systems, the real numbers of particles are up to the order of $O(10^{67})$ particles for example for dark matter haloes (see also section 1.2.3). This enormous number is clearly not possible to simulate with any computer in the near future. One therefore samples the astrophysical system that is described by a distribution function $f(\mathbf{x}, \mathbf{v}, t)$ with N bodies, where N is much less than the number of constituents in the real system, that have mass m_i , position \mathbf{x}_i and velocity \mathbf{v}_i ($i = 1 \dots N$). In principle, the continuous distribution function $f(\mathbf{x}, \mathbf{v})$ is replaced with a discretised version $f_d(\mathbf{x}, \mathbf{v})$ which consists of a set of Dirac delta-functions

$$f(\mathbf{x}, \mathbf{v}) \rightarrow f_d(\mathbf{x}, \mathbf{v}) = \sum_{i=1}^N m_i \delta(\mathbf{x}_i - \mathbf{x}) \delta(\mathbf{v}_i - \mathbf{v}) . \quad (1.23)$$

Initial conditions are set-up by treating the distribution function at a fixed time t_0 as a probability distribution, i.e. one selects coordinates (\mathbf{x}, \mathbf{v}) with a probability proportional to $f(\mathbf{x}, \mathbf{v}) = f(\mathbf{x}, \mathbf{v}, t_0)$. The real astrophysical system is now represented in a Monte-Carlo fashion by N bodies and this method is therefore also called N-body technique.

Generally, by sampling the real astrophysical system with N bodies, the discretised variables give us an estimate (or expectation value) of the real, continuous variables. For example the discretised potential $\Phi_d(\mathbf{x})$ gives us an estimate of the real, continuous potential $\Phi(\mathbf{x})$ and therefrom also an estimate of the acceleration $\mathbf{a}_d(\mathbf{x})$. The fractional error between the real variables and the estimated variables is of order $1/\sqrt{N}$.

We get from the Poisson equation (1.9) or directly from equation (1.4)

$$\Phi_d(\mathbf{x}) = -G \sum_{i=1}^N \frac{m_i}{|\mathbf{x}_i - \mathbf{x}|} \quad (1.24)$$

and the equations of motion in the N-body realisation have to be solved with the discretised potential which is in this way calculated from the Poisson equation (1.9) by a Monte-Carlo sampling. The form of the potential (1.24) has the drawback that singularities appear at the positions \mathbf{x}_i of the particles due to the discreteness of the system. This leads to large scatter in the estimate of the gravitational potential (or equivalently the acceleration) [89]. This can be cured by softening the potential and a detailed discussion of this technique is given in section 1.3.4.

1.3.2 Dynamical evolution and symplectic integrators

If the N-body system is evolved by the Hamiltonian phase-flow defined by equations (1.16) and (1.17), then this mapping preserves the structure of phase-space, i.e. it preserves the Poincaré invariants, hence phase-space volume and the orientation of the volume described by the distribution function in phase-space. A map that preserves the structure of phase-space is called a symplectic⁴ or canonical map. This can be seen in the sense that starting with an N-body realisation at time t_0 of $f(\mathbf{x}, \mathbf{v}, t_0)$ and evolving the N-body system under a symplectic map, then at any later time $t > t_0$, the N-body system is a realisation of $f(\mathbf{x}, \mathbf{v}, t)$ at that time t .

Hence, it is desirable to have a numerical time integration scheme that also has this preservation property. Such a scheme is called a symplectic integrator. It is the exact solution to a discrete Hamiltonian N-body system that is close to the continuous system that is described by $f(\mathbf{x}, \mathbf{v}, t)$. For example, if the Hamiltonian is time-independent such a symplectic integrator would preserve the energy of the discrete system. This approximate energy of the N-body system oscillates about the true energy of the continuous system without any numerical dissipation. The difference between the discrete, approximate Hamiltonian and the continuous one can be seen as a small perturbation given by the truncation error of the integrator, where this error term is also a Hamiltonian. See also appendix A for more details.

A commonly used symplectic integration scheme is the leapfrog integrator. It works as follows: during a time-step ΔT , first the velocities are updated (kick mode) with a time step of $\Delta T/2$ then the new positions are calculated (drift mode) using the new velocities with a time-step of ΔT and finally the velocities are updated to the final values at ΔT with again a half-step of $\Delta T/2$ but with the acceleration calculated from the new positions. This scheme can be written as

$$\mathbf{v}(t + \Delta T/2) = \mathbf{v}(t) + \Delta T/2 \mathbf{a}(t) \quad (1.25)$$

$$\mathbf{x}(t + \Delta T) = \mathbf{x}(t) + \Delta T \mathbf{v}(t + \Delta T/2) \quad (1.26)$$

$$\mathbf{v}(t + \Delta T) = \mathbf{v}(t + \Delta T/2) + \Delta T/2 \mathbf{a}(t + \Delta T) \quad (1.27)$$

and is called the kick-drift-kick mode. The leapfrog scheme can also be formulated in the drift-kick-drift mode, where one drifts first for a half-step, then updates the velocities

⁴The term symplectic was first used by the mathematician Hermann Weyl in his book *The classical Groups* [164]. Symplectic is the Greek adjective corresponding to the Latin word complex and also means twining or plaiting together.

by a full step and then drifts again for a half-step. The leapfrog scheme is symplectic for fixed time-steps ΔT . For further details see also Yoshida [171].

Figure 1.1 shows a comparison of a symplectic and a non-symplectic integrator from Quinn et al. [128]. The figure shows the radial separation r and the radial velocity v_r of an eccentricity $e = 0.5$ Kepler 2-body orbit calculated by a second order leapfrog scheme and a fourth order Runge-Kutta integrator. In both integrations, 24 fix time-steps per orbit were taken and in total 16 orbits were calculated. The solid line is the exact solution, the filled squares show the points of the leapfrog integrator and the crosses are from the Runge-Kutta integrator. The leapfrog integrator oscillates about the true solution and it remains always on a one dimensional surface which indicates that it is indeed conserving an energy-like quantity. That the orbit is constrained to a one dimensional surface shows that there exists an isolating integral of motion. The orbit calculated with the Runge-Kutta scheme becomes more circular and the integrator performs very bad given that this scheme is a fourth order integration using four times as many force evaluation as the leapfrog scheme.

The symplectic leapfrog scheme is therefore an ideal choice to integrate discrete Hamiltonian N-body systems since it can also be formulated in comoving coordinates as a symplectic integrator for cosmological structure formation simulations [128] and is relatively easy to implement in computer programs.

1.3.3 Choice of time-steps

The leapfrog scheme described above is only symplectic for fixed time-steps, i.e. only if all the particles have the same time-step in the N-body simulation. But in order to follow the dynamics correctly in dense regions, this would mean that for all particles very small time-steps should be set. This is computationally very expensive and is therefore not efficient for high resolution simulations.

A solution for this problem is to use variable time-steps for each particle. But by using adaptive individual time-steps for each particle according to some selection criterion, the symplectic behaviour is lost [128, 140].

Adaptive methods show significant speed-ups over fixed-step integrations for the price of accuracy. By choosing the time-step criterion carefully and controlling the errors, we can pass over to an approximate symplectic behaviour of the integration scheme so that it is stable enough for time-scales that are not many orders of magnitudes longer than the dynamical time of the system. For a detailed discussion of time-stepping schemes and criteria see chapter 3.

1.3.4 Acceleration calculation

Softened accelerations

The form of the discrete gravitational potential of equation (1.24) has the drawback that it is singular close to individual particles which leads to large scatter of the estimated variables like potential or acceleration. This can also lead to numerical problems during

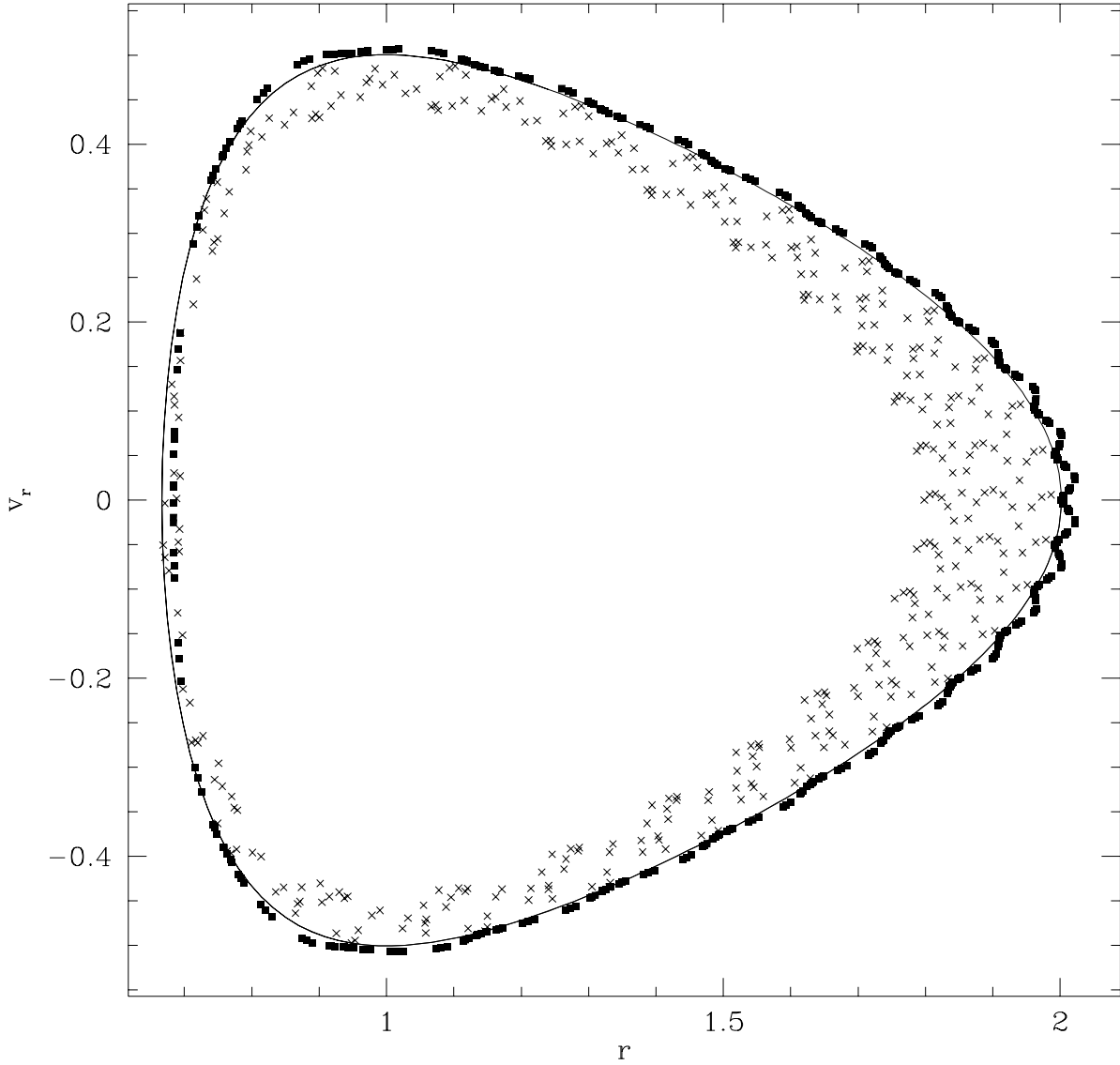


Figure 1.1: A comparison of a symplectic and a non-symplectic integrator. The figure shows the radius r and the radial velocity v_r of a eccentricity $e = 0.5$ Kepler orbit calculated by a second order leapfrog scheme and a fourth order Runge-Kutta integrator. In both integrations, 24 fix time-steps per orbit were taken and in total 16 orbits were calculated. The solid line is the exact solution, the filled squares show the points of the leapfrog integrator and the crosses are from the Runge-Kutta integrator. Figure taken from Quinn et al. [128]

the integration. A technique to avoid these problems is the implementation of a softening parameter ϵ like

$$\hat{\Phi}_d(\mathbf{x}) = -G \sum_{i=1}^N \frac{m_i}{\sqrt{|\mathbf{x}_i - \mathbf{x}|^2 + \epsilon^2}} . \quad (1.28)$$

This type of softening is called the Plummer softening and the singularities at the particle positions \mathbf{x}_i are cancelled. For collisionless systems it also has the advantage that this smoothing of the potential suppresses small-scale fluctuations arising from close particle encounters due to the discreteness of the N-body realisation. Since in collisionless systems such small scale fluctuations are unphysical, it is therefore important to use a softened potential. In collisional systems, of course, one chooses the softening length ϵ as small as possible or even zero and tries to cure the singularities with other numerical techniques such as regularisation [1, 2].

Another problem with the simple Plummer softening is that it affects the potential on all scales. Hence, it is much more useful to use a compact softening. We can write a more general form for the softened potential as

$$\hat{\Phi}_d(\mathbf{x}) = -G \sum_{i=1}^N \frac{m_i}{\epsilon} \phi \left(\frac{|\mathbf{x}_i - \mathbf{x}|}{\epsilon} \right) . \quad (1.29)$$

This form separates the two aspects of the softening method: a) the softening kernel $\phi(r)$ which determines the functional form of the modified gravity and b) the softening length ϵ . The Plummer softening corresponds to

$$\phi(r) = \frac{1}{\sqrt{r^2 + 1}} . \quad (1.30)$$

The corresponding softened quantities for the acceleration $\hat{a}_d(\mathbf{x})$ and density $\hat{\rho}_d(\mathbf{x})$ are given by

$$\hat{a}_d(\mathbf{x}) = G \sum_{i=1}^N \frac{m_i}{\epsilon^2} \phi' \left(\frac{|\mathbf{x}_i - \mathbf{x}|}{\epsilon} \right) \frac{\mathbf{x}_i - \mathbf{x}}{|\mathbf{x}_i - \mathbf{x}|} \quad (1.31)$$

$$\hat{\rho}_d(\mathbf{x}) = \sum_{i=1}^N \frac{m_i}{\epsilon^3} \eta \left(\frac{|\mathbf{x}_i - \mathbf{x}|}{\epsilon} \right) , \quad (1.32)$$

where

$$\eta(r) = -\frac{1}{4\pi r^2} \frac{\partial}{\partial r} \left(r^2 \frac{\partial \phi(r)}{\partial r} \right) \quad (1.33)$$

is the kernel density and ' denotes derivative with respect to r . The kernel density for the Plummer softening would be

$$\eta(r) = \frac{3}{4\pi} \frac{1}{(r^2 + 1)^{5/2}} . \quad (1.34)$$

There are many possible choices for the functional form of the softening kernel $\phi(r)$. If the kernel density has compact support, then the gravity is not modified on distances larger than r_0 from the particle, i.e. $\eta(r) = 0$ for $r \geq r_0$ and the accelerations are perfectly Newtonian for distances larger than r_0 from the particle. Kernel densities that have negative values near their outer edge correct for the underestimation of the acceleration near the origin and are therefore called compensating kernels. Hence, compact and compensating kernels are the best choice one can make in order to soften the potential and accelerations.

Following Dehnen [30], figure 1.2 shows different compact and compensating kernels $K_0 - K_3$ compared with the Plummer scheme and the true Newtonian case. The functional form of the kernel K_n is given by

$$K_n = \frac{(2n+5)!}{(n+1)!(n+2)! 2^{2n+6} \pi} (5 - (2n+7)r^2) (1-r^2)^n \Theta(1-r^2) \quad (1.35)$$

where Θ is the Heaviside step function. Plotted are the potential (top panel), acceleration (middle panel; called force in the figure since here force denotes the force per mass) and the density (bottom panel). The functions were scaled so that the maximum force equals unity. The figure nicely illustrates the negative densities near the outer edge of the kernels. The compact kernels join smoothly the Newtonian curves at the edge whereas the Plummer scheme also modifies the gravity on larger scales. For a detailed discussion about the optimal softening scheme see also Dehnen [30] from which figure 1.2 originates.

Direct method

A straightforward method to calculate the acceleration at position \mathbf{x} would be the direct summation over all N particles in the N-body realisation

$$\mathbf{a}_d(\mathbf{x}) = G \sum_{i=1}^N m_i \frac{\mathbf{x}_i - \mathbf{x}}{|\mathbf{x}_i - \mathbf{x}|^3} . \quad (1.36)$$

In order to calculate the accelerations on all the N particles one needs exactly

$$\sum_{i=1}^{N-1} i = \frac{1}{2} N(N-1) \quad (1.37)$$

times to evaluate an acceleration. Hence, this method is of order $O(N^2)$ and the number of particles one can use to represent the astrophysical system is limited by the immense costs in evaluating forces in this approach. Normally only collisional systems that also have a small number of particles like globular clusters or star clusters are simulated with this technique. By designing special hardware that allows the calculation of the acceleration directly on the computer chip, the direct approach can be made practical for moderately large N ($O(N) \approx 10^6 - 10^7$). This computer chip architecture is called GRAPE which stands for GRAVity piPE and the operations needed for the calculation of the acceleration are directly hard-wired on the chip [96].

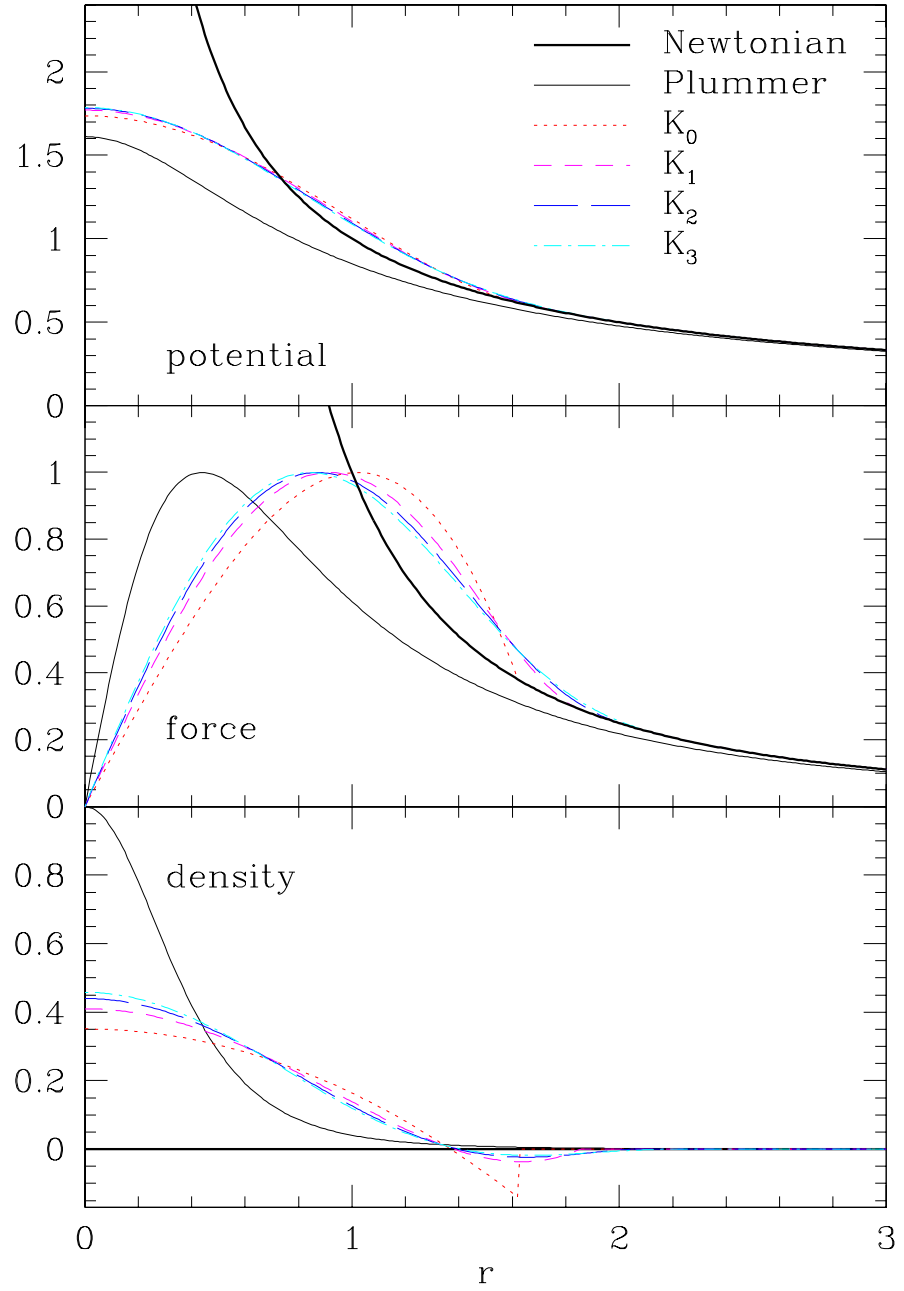


Figure 1.2: Different compact and compensating kernels $K_0 - K_3$ are plotted and compared with the Plummer scheme and the true Newtonian case. Plotted are the potential (top panel), acceleration (middle panel; called force in the figure since here force denotes the force per mass) and the density (bottom panel). For further details see main text. Figure taken from Dehnen [30].

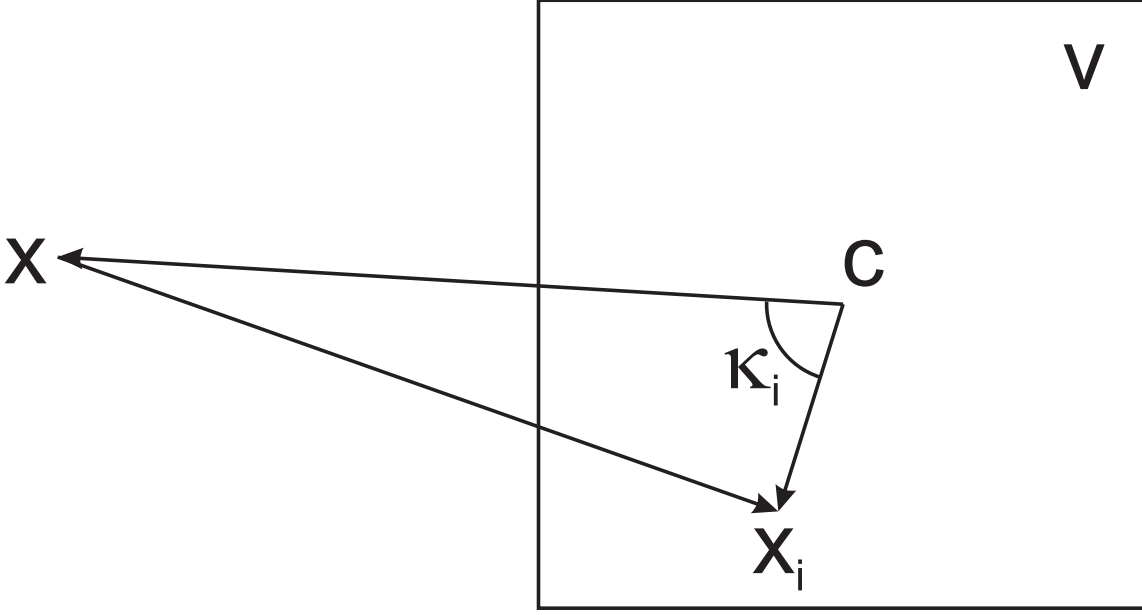


Figure 1.3: Geometrical configuration for multipole expansion.

Hierarchical methods

By expanding the discrete gravitational potential around a point \mathbf{c} and only accounting the contribution to the potential of particles in a volume V around the point \mathbf{c} , we can write a multipole expansion in cartesian coordinates

$$\Phi_d(\mathbf{x}) = -G \sum_{i \in V} \frac{m_i}{|\mathbf{x} - \mathbf{c}|} \sum_{n=0}^{\infty} \left(\frac{|\mathbf{x}_i - \mathbf{c}|}{|\mathbf{x} - \mathbf{c}|} \right)^n P_n(\cos(\kappa_i)) \quad (1.38)$$

where $P_n(\cos(\kappa_i))$ are Legendre polynomials. We have assumed that $|\mathbf{x}_i - \mathbf{c}| < |\mathbf{x} - \mathbf{c}|$ and the angles κ_i are defined by

$$\cos(\kappa_i) = \frac{(\mathbf{x}_i - \mathbf{c}) \cdot (\mathbf{x} - \mathbf{c})}{|\mathbf{x}_i - \mathbf{c}| |\mathbf{x} - \mathbf{c}|} . \quad (1.39)$$

Figure 1.3 shows the geometrical configuration.

For $n = 0$ we have $P_0(\cos(\kappa_i)) = 1$ and the leading term in this series is given by

$$\Phi_d^0(\mathbf{x}) = -G \frac{1}{|\mathbf{x} - \mathbf{c}|} \underbrace{\sum_{i \in V} m_i}_{m_d^0} , \quad (1.40)$$

where m_d^0 is called the monopole moment (or simply the total mass in the volume V).

For $n = 1$ we have $P_1(\cos(\kappa_i)) = \cos(\kappa_i)$ and this term is given by

$$\begin{aligned}\Phi_d^1(\mathbf{x}) &= -G \sum_{i \in V} \frac{m_i}{|\mathbf{x} - \mathbf{c}|} \frac{|\mathbf{x}_i - \mathbf{c}|}{|\mathbf{x} - \mathbf{c}|} \cos(\kappa_i) \\ &= -G \frac{(\mathbf{x} - \mathbf{c})}{|\mathbf{x} - \mathbf{c}|^3} \underbrace{\sum_{i \in V} m_i (\mathbf{x}_i - \mathbf{c})}_{\mathbf{m}_d^1}\end{aligned}\tag{1.41}$$

where \mathbf{m}_d^1 is called the dipole moment. We see that the higher order terms decay rapidly with respect to the dominant monopole term. Higher order multipoles are called quadrupole ($n = 2$), octupole ($n = 3$), hexadecapole ($n = 4$) etc.

By dividing up the space in different regions, we can approximate the contribution from a distant region V around \mathbf{c} to the potential at a point \mathbf{x} by using a multipole expansion and use only the leading terms in the expansion (1.38). By the superposition principle, we can calculate the total potential at point \mathbf{x} by summing up over all regions. The error by truncating the multipole expansion at some order can be controlled by the following criterion

$$\max_{i \in V} (|\mathbf{x}_i - \mathbf{c}|) < |\mathbf{x} - \mathbf{c}| \theta \tag{1.42}$$

where θ is called the opening angle. The geometrical interpretation is that the size of the region V (which we can measure by selecting $\max_{i \in V} (|\mathbf{x}_i - \mathbf{c}|)$) is not allowed to be larger than the distance $|\mathbf{x} - \mathbf{c}|$ to that region times the opening angle θ ; on the sky at position \mathbf{x} , the region is not allowed to appear larger than the size controlled by the opening angle θ .

A common method to divide up the simulation space into different regions is to create a tree-structure by recursively subdividing the whole simulation space into smaller and smaller subregions called cells. The standard method developed by Barnes and Hut [8] starts with a cubic cell with side length L that contains the whole simulation space. This cell is called the root cell. If a cell contains more than one particle it is subdivided into eight sub-cells of side length $L/2$. This procedure is applied recursively until each cell only contains one particle. This tree-structure is therefore called an oct-tree. Now, the simulation space is partitioned into cells of different sizes each containing only one particle and these cells are the leaves of the tree (sometimes also called buckets). The average size of a leaf cell that contains only one particle is of the order of the interparticle distance $h \propto N^{-1/3}$ and the typical number of subdivisions required to reach such a leaf cell from the root cell (that is the height of the tree) is of order $O(\log_2 N^{-1/3}) = O(\log N)$ and the time needed to construct the tree is of order $O(N \log N)$.

If one wants to calculate the acceleration of a particle at position \mathbf{x} in the simulation the following tree-walk procedure is applied. If a cell satisfies the condition (1.42) where \mathbf{c} is the centre-of-mass of the cell under consideration, the interaction via multipole expansion with this cell is accepted. If the cell fails the above criterion (1.42), then its eight sub-cells are checked if they fulfill equation (1.42). This procedure is repeated recursively with all sub-cells. So, by starting at the root cell of the tree which contains the

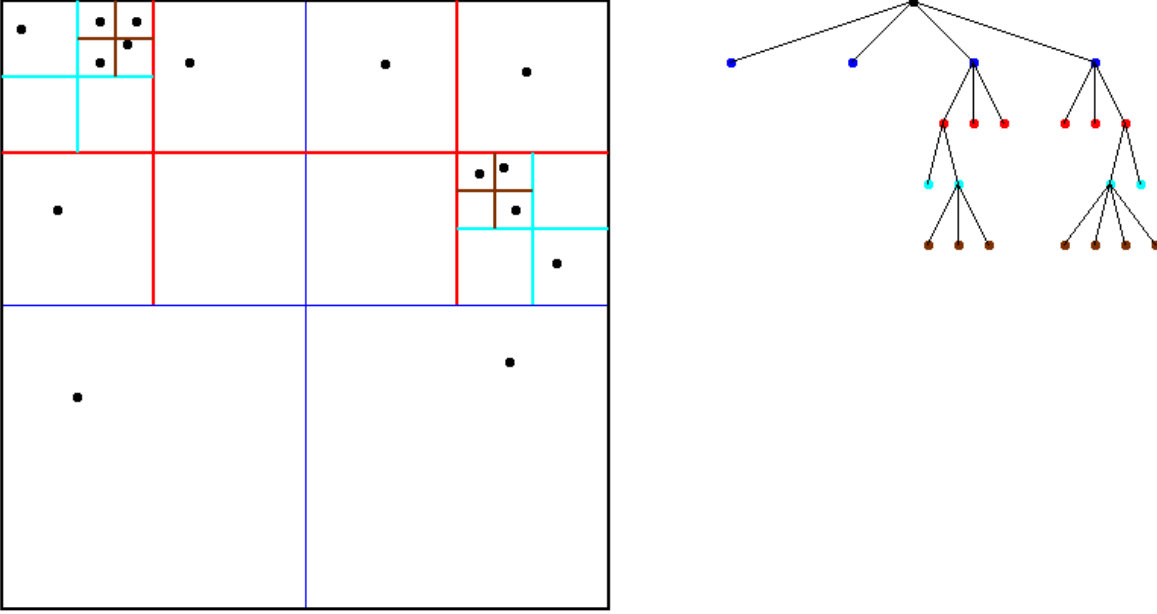


Figure 1.4: Quad-tree: the two dimensional version of the oct-tree in three dimensions. Each leaf cell contains only one particle. Left: the spatial configuration of the splittings. Right: Data structure represented as tree. Figure taken from Demmel [32].

whole simulation space one walks down the tree until one accepts a refined enough cell for the interaction with the particle at \mathbf{x} . If a leaf cell fails to fulfill the opening criterion, then its contribution to the acceleration is calculated directly as described in section 1.3.4. As a result, the acceleration for a particle consists of a far-field part calculated from the multipoles and a near-field part calculated directly by particle-particle interactions. By following this procedure, the number of interactions for calculating the acceleration for a particle is of order $O(\log N)$ for large N and the total cost scales like $O(N \log N)$.

Figure 1.4 shows the two dimensional version of the oct-tree. Each leaf cell contains only one particle. The left panel shows the partitioning of space down to the leaves of the tree. On the right, the tree data structure is shown.

There exist many possible tree-structures like e.g. k -D tree [11] or binary tree [144] which mainly differ in the partitioning procedure. With tree-codes it is nowadays possible to simulate of the order $O(10^{10})$ particles as was done in the Millennium Simulation Project that simulated the evolution of the matter distribution in a cubic region of the universe of two billion light-years on a side from redshift $z = 127$ to the present [99, 143].

1.3.5 PKDGRAV

Throughout this thesis the state-of-the-art gravity code PKDGRAV was used. PKDGRAV stands for Parallel K-D tree GRAVity code and was developed by Joachim Stadel

[144] and Thomas Quinn. The code uses a binary tree⁵ for the partitioning of space and a fourth order multipole expansion (i.e. terms up to the hexadecapole ($n \leq 4$) in expansion (1.38) are included) in order to calculate the accelerations from distant mass in the simulations. Nearby contributions from leaf cells that fail to fulfill the opening criterion are calculated directly. Potentials and accelerations are softened for distances smaller than two softening lengths from a particle with the compact and compensating softening kernel K_1 described in section 1.3.4. The code is fully parallelised and the time integration is done by a symplectic second order kick-drift-kick leapfrog scheme as described in section 1.3.2.

1.4 Unifying both regimes

It is becoming apparent that many problems involve both high accuracy orbit calculations to follow collisional scattering events and the need to simulate many particles in the collisionless mean field limit.

For example, observations show that many galaxies contain a super-massive black hole in their centre with masses correlated to the total bulge mass or dark matter halo mass [47, 58]. The nearest known super-massive black hole is located at the centre of our own galaxy, the Milky Way. Figure 1.5 shows astrometric positions and orbital fits for seven stars around the central super-massive black hole in the centre of the Milky Way. The proper-motion measurements have uncertainties that are comparable to or smaller than the size of the points, and are plotted in the reference frame in which the central super-massive black hole is at rest. On the plane of the sky, three of these stars show orbital motion in the clockwise direction (S0-1, S0-2, and S0-16), and four of these stars have counterclockwise motion (S0-4, S0-5, S0-19, and S0-20). Overlaid are the best-fitting simultaneous orbital solutions, which assume that all the stars are orbiting the same central point mass. Most of these stars are on orbits with very high eccentricity $e \rightarrow 1$. The dynamics of these stars constrain the mass of the super-massive black hole to $3.7(\pm 0.2) \times 10^6 M_\odot$ [42, 59, 60, 135].

Super-massive black holes are fascinating objects in our universe that can be used to test general relativity and structure formation in the universe [159]. They can also play an important role in influencing the local environment through dynamical processes as well as regulating galaxy formation through feedback processes [101, 102, 103, 104, 106, 138, 172]. Super-massive black holes also provide a natural explanation for the energy output of quasars, but how these black holes grow in a relatively short time scale in order to explain the quasar activity at high redshift ($4 < z < 6$) is still unclear [73, 160, 162]. At high redshifts it is thought that galaxy formation proceeds through a succession of merger events. If the proto-galaxies host black holes at their centres then they may also merge hierarchically to form a super-massive black hole. Gas accretion onto the central object may also play an important role in accelerating its growth [160, 161].

⁵PKDGRAV originally used a balanced k -D tree. However, for gravity calculations the balanced k -D tree can behave pathologically in certain cases and it was replaced by a spatial binary tree structure [144].

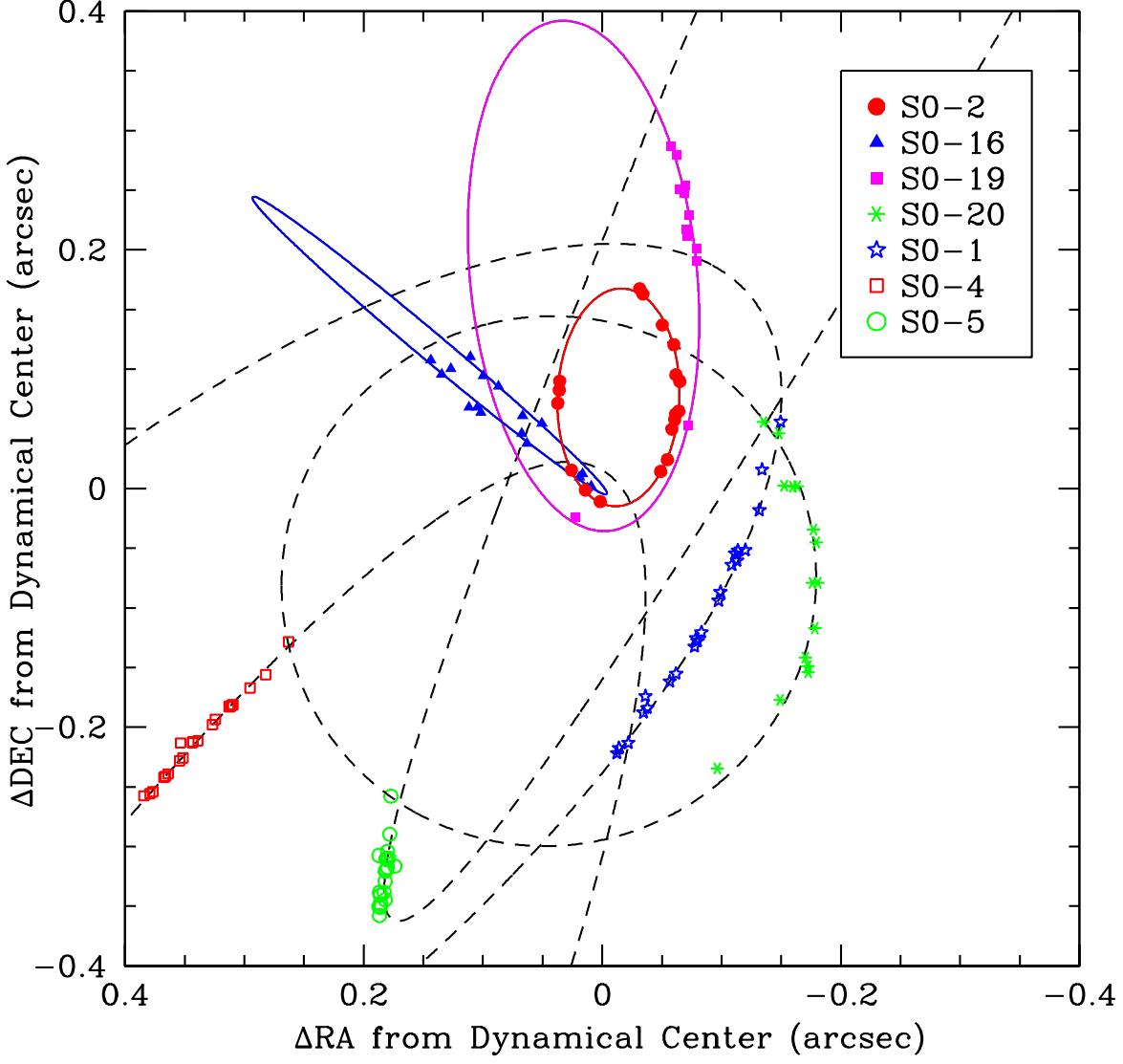


Figure 1.5: Astrometric positions and orbital fits for seven stars around the central super-massive black hole in the centre of our own galaxy, the Milky Way. For further details see main text. Figure taken from Ghez et al. [60].

Hence, understanding the combined formation, dynamics and evolution of these black holes, the dark matter haloes and the stellar systems that they are embedded within, requires a unification of the two N-body regimes discussed above.

This means the interaction between collisionless particles like dark matter and stars is still treated in the mean field limit and the short range forces are softened in order not to suffer from artificial gravitational scattering. In regions where the potential is dominated by e.g. a super-massive black hole, it is important to follow the 2-body orbits around the black holes correctly.

We can define the gravitational influence radius of a single super-massive black hole as the distance within which the potential is dominated by the super-massive black hole, rather than by the smooth background potential created by all the other particles [102, 103]. A standard definition for the radius of influence r_{infl} of a single super-massive black hole is the solution to

$$r = \frac{GM_{\text{SMBH}}}{\sigma^2(r)} , \quad (1.43)$$

where $\sigma(r)$ is the one dimensional velocity dispersion of the surrounding system and M_{SMBH} is the mass of the super-massive black hole. This equation can often only be solved numerically. Hence, an alternative definition of the radius of influence is frequently used where r_{infl} is given by the radius that encloses two times the super-massive black hole mass,

$$M(r_{\text{infl}}) = 2M_{\text{SMBH}} , \quad (1.44)$$

where $M(r)$ is the cumulative mass of the surrounding system assuming spherical symmetry. If the density profile of the surrounding structure is that of a singular isothermal sphere given by [15]

$$\rho(r) = \frac{\sigma^2}{2\pi Gr^2} , \quad (1.45)$$

where the velocity dispersion is constant and independent of radius, the two definitions in equations (1.43) and (1.44) are equivalent. If we calculate the radius of influence for the dark matter in a Milky Way size halo we get of the order of a few dozen pc⁶ and for the central stellar bulge in the Milky Way a few pc.

This is a very difficult dynamical problem with spatial scales ranging from pc to Mpc (as a typical separation of two galaxies) and time-scales ranging from a few yr for an orbit around the super-massive black hole to a few Gyr which is the time-scale needed for the merger of the two galaxies.

1.5 Content of this thesis

The main goal of this doctorate thesis was the development of the N-body tools that can follow the evolution of dark matter haloes on Mpc scales, which host central super-massive black holes that can modify structure and dynamics on pc scales. This problem

⁶pc stands for parsec and is a widely used length unit in astrophysics. 1 pc = 3.086×10^{16} m.

not only includes a wide spatial range of six orders of magnitudes but also a huge temporal range of approximately nine orders of magnitude.

Chapter 2

In order to resolve pc scales in a dark matter halo, of order $O(10^{10})$ particles would be needed. This is clearly not feasible with today's supercomputers and one has to make certain approximations. Here, we present a newly developed multi-mass technique for building dark matter haloes for N-body simulations. With this technique we only resolve the very central part of a dark matter structure with the effectively needed resolution and use lower resolution in low density regions of the simulations, i.e. the outskirts of the haloes. This technique pushes the resolution scale to much smaller scales for given computational costs.

Chapter 3

In order to follow the dynamics correctly, the development of a physically motivated time-stepping scheme was needed. Previous time-stepping schemes based on the acceleration of the particles and which are commonly used in N-body simulations were not able to follow the very active dynamics in the centres of galaxies and in certain cases even delivered unphysical time-steps. Additionally, the acceleration based scheme is not suitable for high resolution simulations since it has a bad scaling with the number of particles used in the N-body realisation. We developed a scheme based on the true dynamical time of a particle and implemented this within the tree-code PKDGRAV. This scheme always sets a physically motivated time-step for a particle in the N-body simulation. It also shows the optimal scaling with the number of particles used in the N-body simulations. The detailed ideas and implementation scheme is presented in this chapter.

Chapter 4

Here, we present applications of the new developments that were already carried out so far. In the first application, the multi-mass technique was used in a cosmological structure formation run in order to resolve the resulting density profile of a high resolution cluster down to one per mill of the virial radius. This resolution corresponds to one billion particles within the virial radius and is the N-body simulation with the highest resolution so far performed. The second application used multi-mass models in order to test a potential explanation of the presence of the five globular clusters at approximately 1 kpc distance from the centre of the Fornax dwarf spheroidal galaxy. For this purpose, cuspy and cored dark matter haloes with an effective resolution of order of $O(10^8)$ particles were used.

Chapter 5

A summary and a perspective on future projects and applications are then presented in chapter 5.

Chapter 2

Multi-mass halo models

2.1 Introduction and motivation

Resolution is a key issue in N-body simulations. In state-of-the-art N-body simulations today, structures can be fully resolved down to the scale of a fraction of a per cent of the virial radius. But there are many problems, where higher resolution in central regions of structures is needed.

For example, the question if the central dark matter density profile of haloes that form in cosmological N-body simulations is cuspy or cored needs at least a resolution of approximately $10^{-3} r_{\text{vir}}$ to be answered. Another example are flat/cored central halo profiles: in order to resolve structures with cored central profiles, a lot of particles are needed since in flat profiles the resolution scaling with the number of particles is the slowest (see below for more details about the scaling of resolution with the number of particles). One further problem that was especially in mind when developing the multi-mass technique, was the dynamics of super-massive black hole binaries in the centre of remnants of galaxy mergers. There, the relevant scales are of order of a few pc $\approx 10^{-6} - 10^{-5} r_{\text{vir}}$ for Milky Way size dark matter haloes.

We illustrate the resolution problem in more detail with a commonly used family of spherically symmetric density profiles used for haloes in N-body simulations: the so called $\alpha\beta\gamma$ -models family [29, 71, 176]. An $\alpha\beta\gamma$ -model density profile is given by

$$\rho(r) = \frac{\rho_0}{\left(\frac{r}{r_s}\right)^\gamma \left(1 + \left(\frac{r}{r_s}\right)^\alpha\right)^{\left(\frac{\beta-\gamma}{\alpha}\right)}}, \quad r \leq r_{\text{vir}}, \quad (2.1)$$

where γ determines the inner and β the outer slope of the density profile whereas α controls the transition between the inner and outer region. The normalisation is given by ρ_0 and r_s is the scale radius defined by $r_s \equiv r_{\text{vir}}/c$ (c is called concentration). The two most famous models that belong to this family are the Moore [110] profile with $(\alpha, \beta, \gamma) = (1.5, 3.0, 1.5)$ and NFW [116] profile with $(\alpha, \beta, \gamma) = (1.0, 3.0, 1.0)$.

The resolution scale mainly depends on the number of particles N_{vir} that samples the structure chosen by the simulator. We can define the mean particle separation as a function of radius in such a structure by

$$h(r) \equiv \sqrt[3]{\frac{m}{\rho(r)}}, \quad (2.2)$$

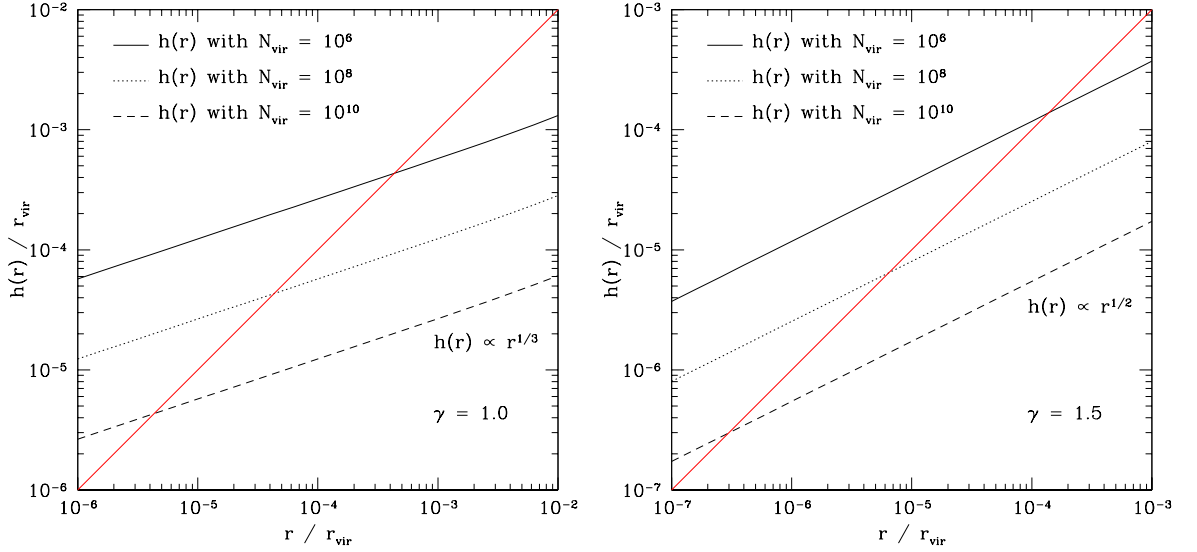


Figure 2.1: Mean particle separation function for a dark matter halo with central slope $\gamma = 1.0$ (left) respectively $\gamma = 1.5$ (right). We used values of $N_{\text{vir}} = (10^6, 10^8, 10^{10}) = (\text{solid, dotted, dashed})$ to evaluate the function. The crossing with the diagonal line corresponds to $h(r) = r$, i.e. the crossing radius is r_{imp} .

where m is the mass per particle. For single-mass models, the mass per particle is simply given by $m = M_{\text{vir}}/N_{\text{vir}}$ and we get for the asymptotic scaling in the central part of the structure $h(r) \propto r^{\gamma/3}$.

In figure 2.1 we plot the mean particle separation for a dark matter halo with central slope $\gamma = 1.0$ (left) respectively $\gamma = 1.5$ (right) with $M_{\text{vir}} = 10^{12} M_{\odot}/h = 1.429 \times 10^{12} M_{\odot}$ ($h = 0.7$)¹. The concentrations were chosen so that the radius where the maximum circular velocity is reached are equal, i.e. $c_{1.0} = 10$ and $c_{1.5} = 5.779$ [173]. We used the following values for the number of particles within the virial volume $N_{\text{vir}} = (10^6, 10^8, 10^{10}) = (\text{solid, dotted, dashed})$ to evaluate the function given by equation (2.2). The innermost particle in a model sampled with N_{vir} particles is approximately located where we have $h(r) = r$ (r is the distance from the geometrical centre). This sets the smallest scale in the physical problem and we call this radius r_{imp} , i.e. $h(r_{\text{imp}}) = r_{\text{imp}}$. But of course one particle is not enough to resolve that scale. If we say we need at least of the order of ≈ 100 particles in the innermost bin so that the bin is well resolved, then each $h(r)$ function gets a shift of factor $\sqrt[3]{100} \approx 4.6$ upwards in figure 2.1². Generally, the scaling of r_{imp} is given by

$$r_{\text{imp}} \propto {}^{3-\gamma}\sqrt{m} \propto {}^{3-\gamma}\sqrt{\frac{1}{N_{\text{vir}}}}. \quad (2.3)$$

¹ h denotes the Hubble constant H in units of $100 \text{ km s}^{-1} \text{ Mpc}^{-1}$. $H = 100 h \text{ km s}^{-1} \text{ Mpc}^{-1}$

²Apart from a geometrical factor that is of the order of unity for the two profiles with $\gamma = 1.0$ respectively $\gamma = 1.5$, this corresponds to the radius that includes 100 times the mass of one particle.

in the region where the slope of the profile is close to $-\gamma$ in the $\alpha\beta\gamma$ -profiles (the inner region). Equation (2.3) illustrates the resolution gain by increasing the number of particles N_{vir} and its dependence on the central density profile slope γ .

By inspecting figure 2.1, we see that we need more than approximately of order $O(10^{10})$ particles in the centre in order to resolve scales of $10^{-6} - 10^{-5} r_{\text{vir}}$ which correspond to approximately 1 pc in physical units in this model. It is worth remarking, that with the same number of particles N_{vir} much smaller scales are resolved in the steeper profile with $\gamma = 1.5$ than in the $\gamma = 1.0$ profile although the concentration was lower. Generally, the steeper the central profile, the more the particles are concentrated. Nonetheless, this enormous amount of particles per dark matter halo is hardly doable today - even with large supercomputers like zBox2³, a large 125 nodes cluster with in total 500 64 bit cpus on quad-boards. But since we only need this high resolution at the very centre of the dark matter halo, our solution to this problem is the usage of haloes with shells of different resolution, i.e. we use light particles with a small mean particle separation in the centre and heavy particles in the outer parts of the halo.

2.2 Method

The technique for generating multi-mass equilibrium haloes is based on the method presented in Kazantzidis et al. [80]. We give here a short review of the procedure.

We can choose the density profile from the $\alpha\beta\gamma$ -models family given by equation (2.1) for $r \leq r_{\text{vir}}$ with concentration c , profile slopes α , β and γ , virial mass M_{vir} , and number of particles N_{vir} as input parameters. This determines the normalisation ρ_0 and the scale radius r_s for a chosen cosmology. Beyond the virial radius, an exponential cut-off is applied. For further details see Kazantzidis et al. [80] and Zemp [173]. The particle positions are initialised from the cumulative mass function $M(r)$. With the particle's positions, the acceptance-rejection technique [87] is used to determine its velocity from the distribution function and the velocity structure is chosen to be isotropic. This procedure leads to perfectly stable equilibrium models as was shown in Kazantzidis et al. [80]. These models do not show the flattening in the central part of the halo during evolution as it is obtained in the case of the assumption of a local Maxwellian velocity distribution.

In the multi-mass case, one has the choice to introduce different spherical shells with different particle masses, i.e. the central shell is populated by light particles and the outer shell is populated by heavy particles. Initially, the different species are strictly separated but with time the different species mix and form stable sub-profiles while leaving the total mass profile unchanged.

Of course this technique introduces some further numerical artefacts as e.g. heating of the light particles by the heavy particles or mass segregation of the heavy outer particles. The dynamical friction force that a particle of mass M experiences in a sea of

³www.zbox2.org

light particles with mass $m \ll M$ is [15, 21]

$$F_{\text{df}} \propto M^2 \quad (2.4)$$

and the time-scale for this particle to reach the centre of the structure is

$$T_{\text{df}} \propto M^{-1} . \quad (2.5)$$

Hence, by choosing moderate mass ratios we can reduce the effect of mass segregation. By scaling the softening lengths of the heavy particles as a function of their mass, also artificial 2-body scattering can be reduced. For further details about the scaling of the softening, see section 2.3.

An additional dynamical effect that restricts the resolution is the relaxation of the system [16, 35, 125]. We define the local relaxation time as (see also equation (1.13))

$$T_{\text{relax}}(r) \equiv \frac{N(r)}{8 \ln \Lambda} T_{\text{dyn}}(r) , \quad (2.6)$$

where

$$T_{\text{dyn}}(r) \equiv 2\pi \sqrt{\frac{r^3}{GM(r)}} \quad (2.7)$$

is the dynamical or orbital time at radius r and

$$\ln \Lambda = \frac{r_{\text{half}}}{\epsilon} \quad (2.8)$$

is the Coulomb logarithm where r_{half} is the half mass radius of the system and ϵ is the softening of the particles. This specific choice for the Coulomb logarithm was motivated by studies of Diemand et al. [35]. Here, $M(r)$ is the cumulative mass function and $N(r) \equiv M(r)/m$ denotes the number of particles within r . An alternative definition can be obtained by replacing $\ln \Lambda$ by $\ln N(r)$ but both versions of the local relaxation time give similar estimates. Expression (2.6) for the local relaxation time with $\ln \Lambda = \ln N(r)$ is in spherically symmetric structures equivalent to the empirical expression found by Power et al. [125].

The local dynamical time allows us to define down to what radius r_{res} the system is well resolved. Below that scale the structure may suffer from relaxation, particles are scattered out and therefore undesired flattening of the profile can happen. If the simulation time is T_{S} , we can solve

$$T_{\text{S}} = T_{\text{relax}}(r) \quad (2.9)$$

for the radius which we call $r_{\text{res}}(T_{\text{S}})$ and express it as a function of simulation time T_{S} . This is rather a conservative definition of the resolution scale. On scales smaller than this radius, the dynamics can be affected by physical relaxation which is in most cases only due to the lack of resolution. This is not a numerical effect since a real astrophysical system with the same number of particles like in the simulation would behave similarly.

The problem is that in the near future we can not simulate of the order of $O(10^{70})$ dark matter particles like the real astrophysical system would have. Therefore, this effect due to under-resolving the system with not enough particles will always be a limitation to N-body simulations.

In principle, the only known dynamically stable system in the universe is the Keplerian 2-body system.⁴ Dynamical effects like relaxation or evaporation will sooner or later lead to the disruption of any system. It is therefore always a question within what time-scale the system is stable. The time-scale of interest is normally of order of the age of the universe and for most cases the astrophysical systems can be regarded as perfectly stable within that time-scale. This is different in N-body simulations. Here, one just tries to generate models that show the desired stability behaviour during the time-scale of interest with the least amount of particles needed. It is therefore clear that the artificial N-body models show these disruption effects much sooner since they are not modeled with the true number of particles like the real astrophysical system one wants to study.

In section 2.3, we show that by a careful choice of parameters like mass ratio between the different species and softening length, these effects on global characteristics like the radial density profile are small. The multi-mass technique is therefore an efficient method to perform high resolution N-body simulations.

2.3 Tests

2.3.1 Two-shell models

We performed a series of runs in order to show how the multi-mass model works and to illustrate the limits of this method. In this series we chose four different profiles from the $\alpha\beta\gamma$ -family described by equation (2.1). We chose for the different haloes a virial mass of $M_{\text{vir}} = 10^{12} M_{\odot}/h = 1.429 \times 10^{12} M_{\odot}$ ($h = 0.7$) which corresponds to a virial radius of $r_{\text{vir}} \approx 289$ kpc and a virial density $\rho_{\text{vir}} = 1.408 \times 10^4 M_{\odot} \text{ kpc}^{-3}$ (spherical overdensity $\approx 100 \rho_{\text{crit}}$ in a standard Λ CDM-cosmology [45]). The following density profile parameters were the same for all models: outer profile $\beta = 3$, transition coefficient $\alpha = 1$ and concentration $c = r_{\text{vir}}/r_s = 20$ (r_s is the scale radius). We varied the inner profile form $\gamma = 0.0 \dots 1.5$ and chose for the shell radius the scale radius, i.e. $r_{\text{shell}} = r_s$. We resolved the density profile within r_{shell} always with 300000 particles and changed the number of particles in the outer shell for the other runs so that the mass ratio had the following values $1 \times 10^0, 3 \times 10^0, 1 \times 10^1, 3 \times 10^1, 1 \times 10^2, 3 \times 10^2, 1 \times 10^3$. The choice of softening for the light particles ϵ_{light} and the total number of particles N_{vir} in the case of equal mass particles in the inner and outer shell as well as the estimated resolution scale after 10 Gyr, $r_{\text{res}}(10 \text{ Gyr})$, are given in table 2.1. The softening lengths of the heavy particles were scaled like r_{imp} (equation 2.3), i.e.

$$\epsilon_{\text{heavy}} = \epsilon_{\text{light}} \sqrt[3-\gamma]{\frac{m_{\text{heavy}}}{m_{\text{light}}}} = \epsilon_{\text{light}} \sqrt[3-\gamma]{R_{\text{M}}} \quad (2.10)$$

⁴This is only true in the Newtonian regime. In General Relativity, not even a 2-body orbit is dynamically stable and the orbit decays due to the emission of gravitational radiation [5, 41, 74].

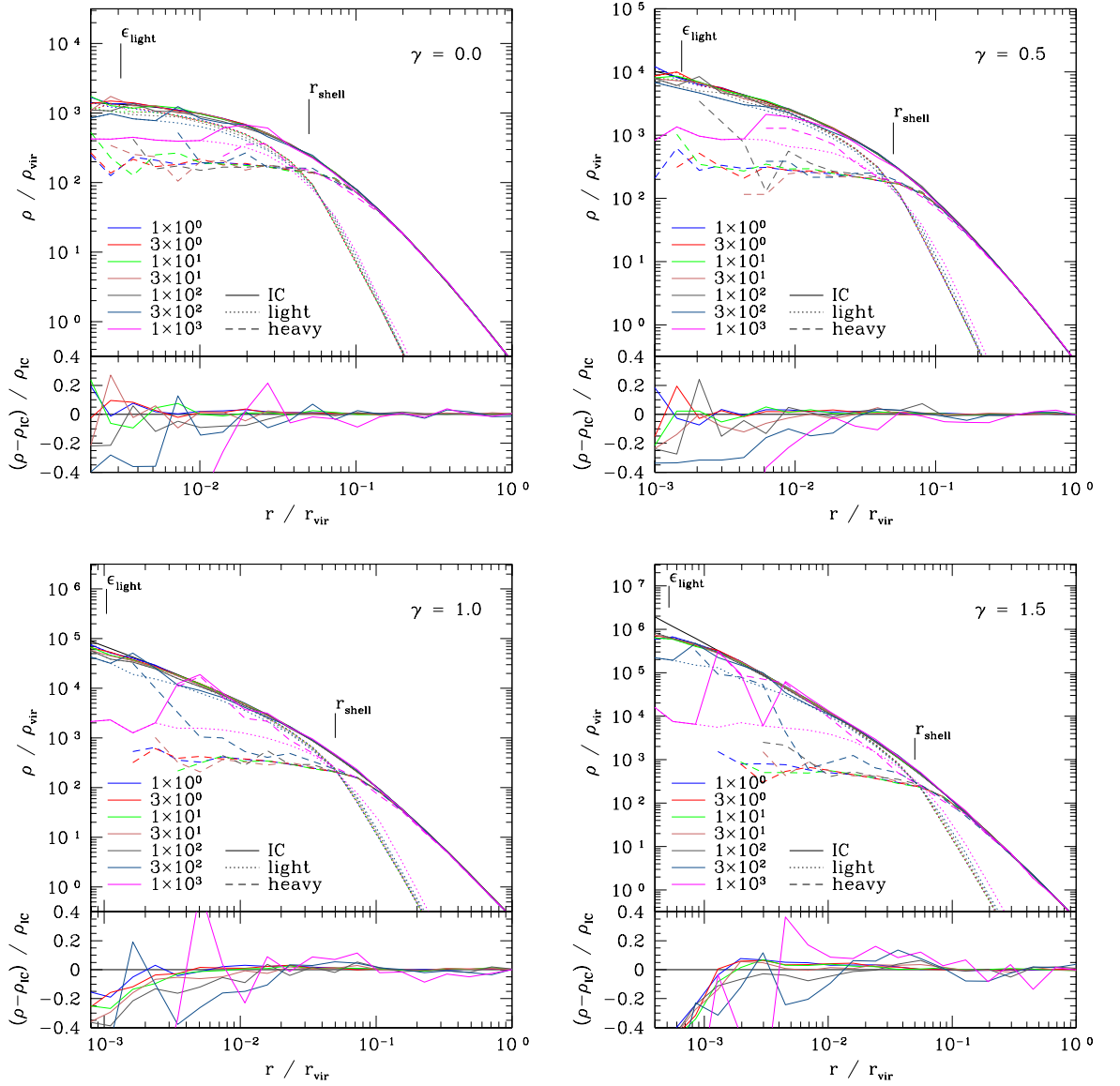


Figure 2.2: Multi-mass stability tests for mass profiles with different inner slope $\gamma = 0.0 \dots 1.5$. Each run was evolved for 10 Gyr. The top panels for each slope γ show the total density profile and the sub-profiles [(light,heavy) = (dotted,dashed)] for the different mass ratio runs normalised to the virial density $\rho_{\text{vir}} = 1.408 \times 10^4 \text{ M}_{\odot} \text{ kpc}^{-3}$. The lower panel shows the relative change of the total profile with radius $(\rho - \rho_{\text{IC}}) / \rho_{\text{IC}}$ normalised to the profile of the initial conditions ρ_{IC} .

γ	0.0	0.5	1.0	1.5
ϵ_{light}	0.9 kpc	0.45 kpc	0.3 kpc	0.15 kpc
	$\approx 3.1 \times 10^{-3} r_{\text{vir}}$	$\approx 1.6 \times 10^{-3} r_{\text{vir}}$	$\approx 1.0 \times 10^{-3} r_{\text{vir}}$	$\approx 5.2 \times 10^{-4} r_{\text{vir}}$
N_{vir}	7.215×10^6	4.880×10^6	3.250×10^6	2.112×10^6
$r_{\text{res}}(10 \text{ Gyr})$	$\approx 1.42 \text{ kpc}$	$\approx 1.35 \text{ kpc}$	$\approx 1.25 \text{ kpc}$	$\approx 1.15 \text{ kpc}$
	$\approx 4.9 \times 10^{-3} r_{\text{vir}}$	$\approx 4.7 \times 10^{-3} r_{\text{vir}}$	$\approx 4.3 \times 10^{-3} r_{\text{vir}}$	$\approx 4.0 \times 10^{-3} r_{\text{vir}}$

Table 2.1: Summary of parameters for the different models. The rows are softening of the light particles, ϵ_{light} , total number of particles in the equal mass case, N_{vir} , and estimated resolution radius after 10 Gyr, $r_{\text{res}}(10 \text{ Gyr})$.

where R_{M} is the mass ratio of the heavy to the light particles. Each of these 28 models was evolved in isolation for 10 Gyr in order to test the stability of the structures with PKDGRAV (see section 1.3.5). In order to follow the dynamics in the centre correctly, we used the dynamical time-stepping scheme developed by Zemp et al. [174] (see chapter 3).

In figure 2.2, we present the density profiles of these runs after 10 Gyr. For moderate mass ratios R_{M} up to 10-30 (or even $R_{\text{M}} \approx 100$ for steep central profiles) the effects on the total density profile are small and the profile remains stable down to the level of a few ϵ_{light} . Such deviations are anyway expected since the forces in PKDGRAV are softened if two particles have separations of order of their softening length. By comparing the equal mass cases for the two steepest central profiles, we see that the flattening effect due to relaxation sets in at a factor 2-3 times smaller radius than the estimated value $r_{\text{res}}(10 \text{ Gyr})$, confirming that it is rather a conservative estimate.

The same behaviour is also seen in the anisotropy profiles. In figure 2.3, we plot the velocity anisotropy parameter defined by

$$\beta(r) \equiv \frac{1}{2} \frac{\sigma_{\text{tan}}(r)}{\sigma_{\text{rad}}(r)}, \quad (2.11)$$

where $\sigma_{\text{tan}}(r)$ is the tangential velocity dispersion and $\sigma_{\text{rad}}(r)$ is the radial velocity dispersion in a spherical coordinate system as a function of radius r . For isotropic systems we obtain $\beta(r) = 1$.⁵ We see again that for moderate mass ratios up to approximately 30 the velocity anisotropy profile stays isotropic.

Figure 2.2 also illustrates that the different species form stable sub-profiles. The shell radius was chosen in a zone where the local density profile is steep so that the transition region is small and in the inner or outer region the light respectively heavy particles dominate. Only for very high mass ratios, the total density profile is strongly perturbed by heating effects of the heavy particles and the heavy particles sink to the centre due to the better efficiency of dynamical friction. But for moderate mass ratios, these effects are small and expected only for much longer time-scales.

⁵This definition deviates from the standard definition normally used e.g. in Binney and Tremaine [15]. Normally, $\beta_{\text{std}} = 1 - \beta$ but since we plot the relative change with respect to the isotropic initial conditions (which would be $\beta_{\text{std}} = 0$) we used this alternative definition.

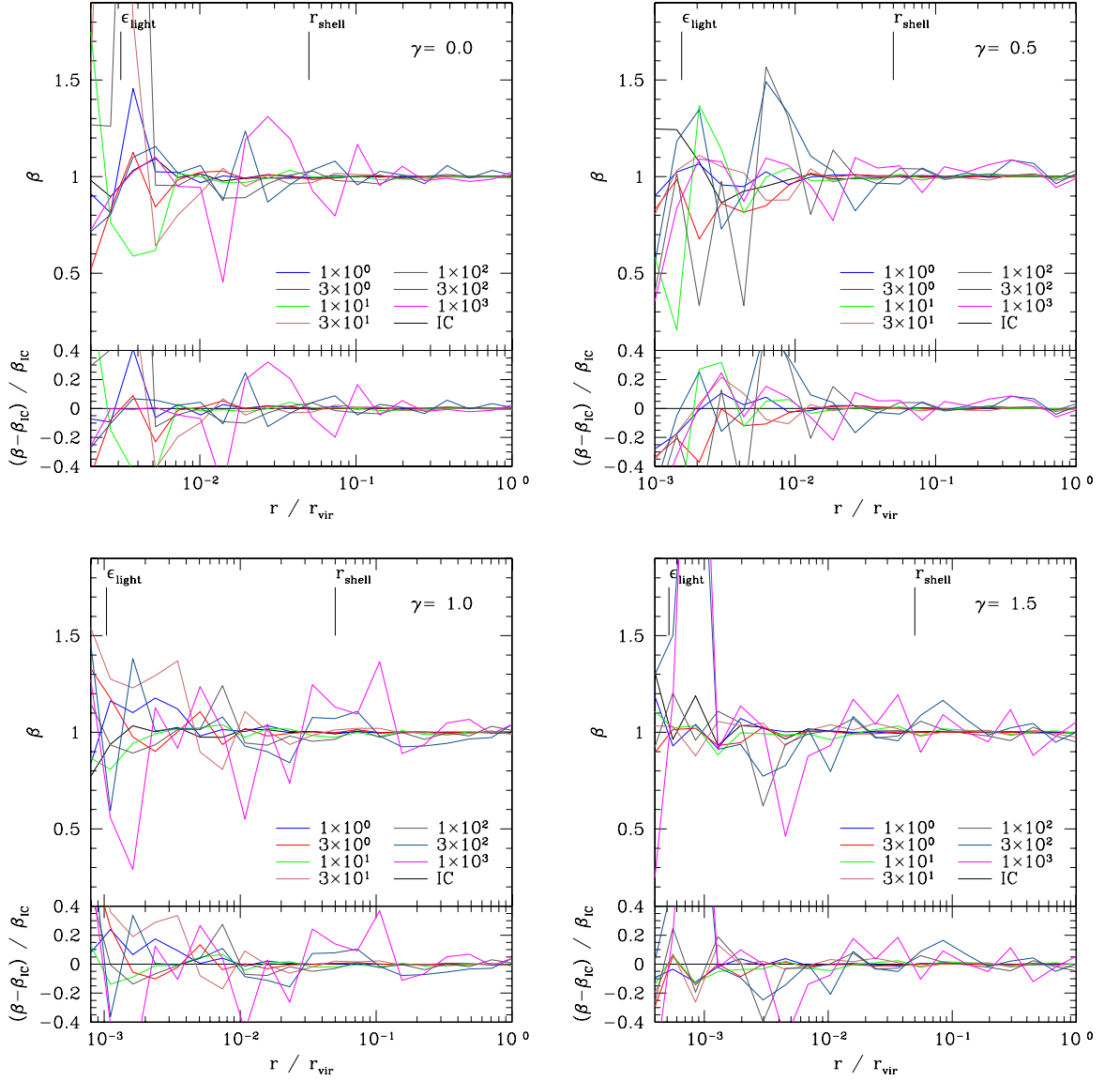


Figure 2.3: Multi-mass stability tests for mass profiles with different inner slope $\gamma = 0.0 \dots 1.5$. Each run was evolved for 10 Gyr. The top panels for each slope γ show the anisotropy profile for the different mass ratio runs. The lower panel shows the relative change of the total profile with radius $(\beta - \beta_{\text{IC}}) / \beta_{\text{IC}}$ normalised to the profile of the initial conditions β_{IC} .

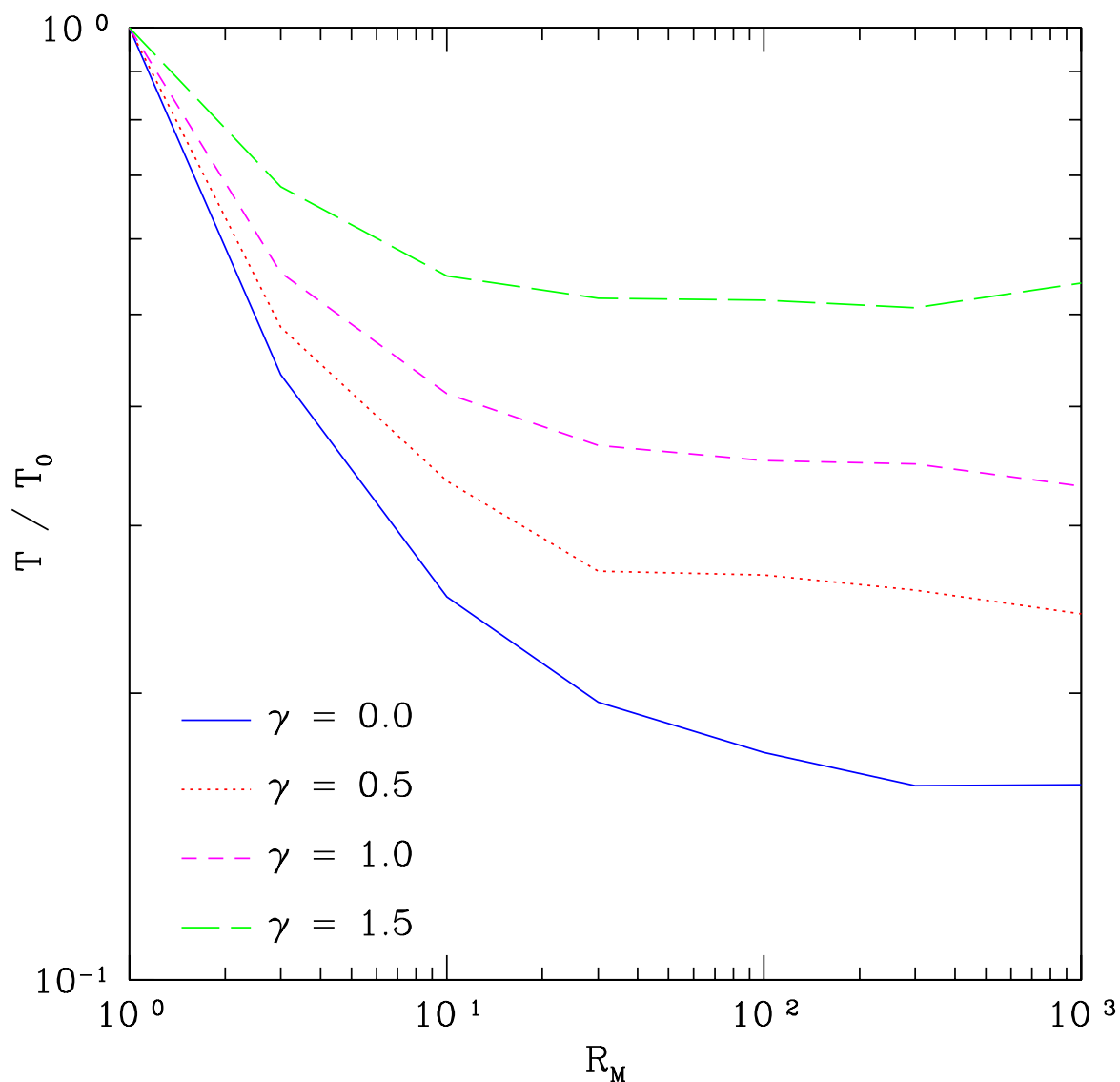


Figure 2.4: The computer run time T needed for the 10 Gyr stability run described in the text is plotted as a function of mass ratio R_M for the different central profiles γ . T_0 is the computer run time needed for the equal mass run. A substantial fraction of time is gained in all cases. Most of the time gain is already obtained for small mass ratios.

The main advantage of these multi-mass models is the speed up gain. In figure 2.4, we plot the computer run time T needed for the 10 Gyr stability test run described above as a function of mass ratio R_M . We normalise with the time T_0 needed by the equal mass run. Figure 2.4 illustrates that we gain a substantial fraction of computer run time in all cases. Most of the gain is already obtained for small mass ratios R_M . For example, the run with inner slope $\gamma = 0.0$ and mass ratio $R_M = 10$ is approximately four times faster than the same run without multi-mass refinement and does not show any perturbation effect of the multi-mass technique on the density profile. Therefore, the usage of too high mass ratios is not recommended since most of the computational work in the simulation comes from the central part and too high mass ratios only lead to larger perturbations of the models.

The steeper the central profile, the less is the computer run time gain. This is due to the fact that most of the work in the N-body simulation for steep profiles is concentrated in the centre. In the centre, the particles are on very small time-steps compared to the less dense, outer regions of a dark matter halo in an N-body simulation and as a consequence a lot of expensive force calculations are needed. It is especially dramatic if one does the dynamics correct by using a dynamical time-stepping criterion rather than the ad-hoc criterion based on the acceleration which can even lead to completely wrong and unphysical time-steps in high resolution N-body simulations. See also chapter 3 for more details about this. That is simply the price one has to pay for correct physics! Using a hierarchy of trees where one freezes part of the simulation during the N-body run could be a promising solution in order to perform high resolution N-body simulations in the future and is under development.

2.3.2 Three-shell models

This method also works for three shells with different mass resolutions. In figure 2.5, we present a profile with central slope $\gamma = 1.0$ that has the same general specifications like virial mass, virial radius, virial density, concentration as the models described in section 2.3. The shell radii were set at $r_{\text{shell},1} = 2$ kpc respectively $r_{\text{shell},2} = 10$ kpc. We put in each shell 3×10^6 particles resulting in mass ratios of $m_{\text{medium}}/m_{\text{light}} \approx 13.53$, $m_{\text{heavy}}/m_{\text{light}} \approx 245.9$ and $m_{\text{heavy}}/m_{\text{medium}} \approx 18.17$. This configuration corresponds to an effective resolution in the centre of $N_{\text{vir}}^{\text{eff}} = 7.8 \times 10^8$ particles. The softening of the lightest species was $\epsilon_{\text{light}} = 0.05$ kpc $\approx 1.7 \times 10^{-4} r_{\text{vir}}$. The softening length of the other particles was scaled according to relation (2.10).

Figure 2.5 illustrates that the total profile of the three-shell model is stable over 10 Gyr down to approximately $3 \times 10^{-4} r_{\text{vir}}$. The total profile fluctuates only a few per cent over 3.5 orders of magnitude in space. This was only possible by using the multi-mass technique where we used in total approximately only 10^7 particles in order to generate a model that has an effective central resolution of $N_{\text{vir}}^{\text{eff}} = 7.8 \times 10^8$ particles.

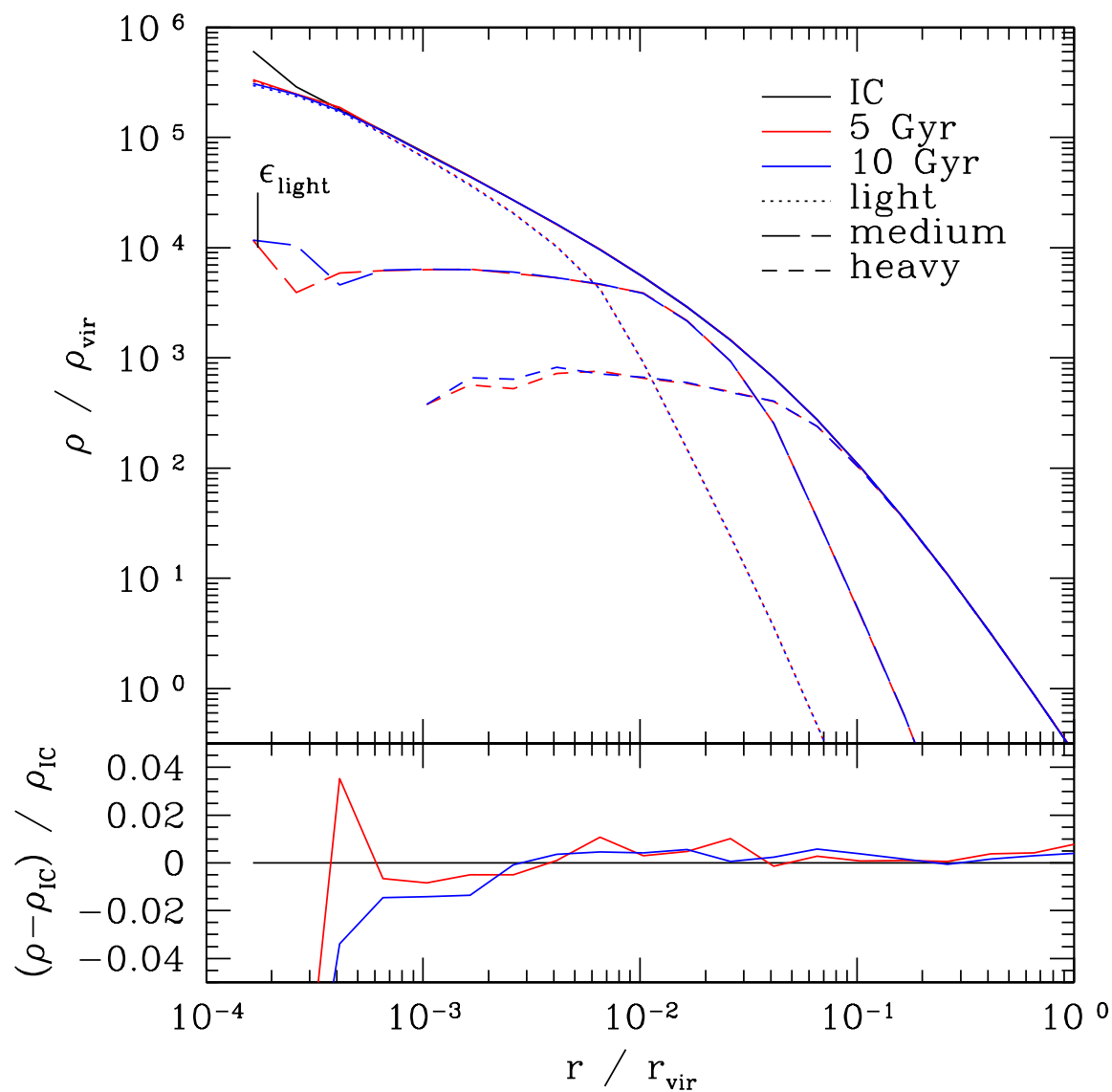


Figure 2.5: The total profile of the three-shell model is stable over 10 Gyr down to approximately $3 \times 10^{-4} r_{\text{vir}}$. Fluctuations in the total profile are on a few per cent level.

γ	0.0	1.0
ϵ_{light}	0.48 kpc	0.3 kpc
	$\approx 1.7 \times 10^{-3} r_{\text{vir}}$	$\approx 1.0 \times 10^{-3} r_{\text{vir}}$
$N_{\text{vir}}^{\text{eff}}$	4.812×10^7	5.232×10^7
$r_{\text{res}}(10 \text{ Gyr})$	$\approx 0.77 \text{ kpc}$	$\approx 0.40 \text{ kpc}$
	$\approx 2.6 \times 10^{-3} r_{\text{vir}}$	$\approx 1.4 \times 10^{-3} r_{\text{vir}}$

Table 2.2: Summary of parameters for the two initial conditions used for the mergers. The rows are softening of the light particles, ϵ_{light} , effective number of particles in the haloes, $N_{\text{vir}}^{\text{eff}}$, and estimated resolution radius after 10 Gyr, $r_{\text{res}}(10 \text{ Gyr})$.

2.4 Preservation of cusp slope

Dehnen [31] showed that in a merger of self-gravitating cusps with different central slopes the merger remnant has always the slope of the steepest progenitor. In other words the steepest cusp slope should be preserved.

Collisionless mergers of dark matter haloes were already studied in earlier work [e.g. 4, 16, 114] but none of these studies had the resolution of the simulations presented here. We do not find any discrepancies between this work and the earlier studies and see this therefore more as a confirmation that the multi-mass technique works in the extreme dynamics of a dark matter halo merger event.

We initially set-up two dark matter halo models with different central slope. Both profiles were from the $\alpha\beta\gamma$ -model family (see equation (2.1)) and had a virial mass of $M_{\text{vir}} = 10^{12} M_{\odot}/h = 1.429 \times 10^{12} M_{\odot}$ ($h = 0.7$) which corresponds to a virial radius of $r_{\text{vir}} \approx 289 \text{ kpc}$, a virial density $\rho_{\text{vir}} = 1.408 \times 10^4 M_{\odot} \text{ kpc}^{-3}$ and a concentration of $c = 20$. That are the same general specifications as the models described in section 2.3. The outer slope was fixed to $\beta = 3$, the transition coefficient was set to $\alpha = 1$ in both cases. One profile had an inner slope of $\gamma = 0.0$ and a shell radius of $r_{\text{shell}} = r_s = 14.47 \text{ kpc}$. The other profile had a central slope of $\gamma = 1.0$ and a shell radius of $r_{\text{shell}} = 5 \text{ kpc}$. In both cases, a mass ratio of $R_M = 20$ between heavy and light particles was chosen. For softening and effective number of particles see also Table 2.2. The softening lengths of the heavy particles were scaled according to relation (see also equation 2.10)

$$\epsilon_{\text{heavy}} = \epsilon_{\text{light}} \sqrt[3-\gamma]{\frac{m_{\text{heavy}}}{m_{\text{light}}}} = \epsilon_{\text{light}} \sqrt[3-\gamma]{R_M} . \quad (2.12)$$

The resolution is clearly limited by the centrally flat ($\gamma = 0.0$) model since here much more particles are needed to resolve a given scale compared to steeper profiles. To resolve the same scale with the steep profile much less particles would be needed, but since we would not like to have too high mass ratios between any species of particles involved in the merger we adjusted the number of particles in the profile with $\gamma = 1.0$ so that its particles had similar masses as the particles in the $\gamma = 0.0$ model.

We evolved both haloes in isolation for 10 Gyr in order to test the stability again. In total three mergers were performed: a cusp-cusp, a core-core and a cusp-core merger

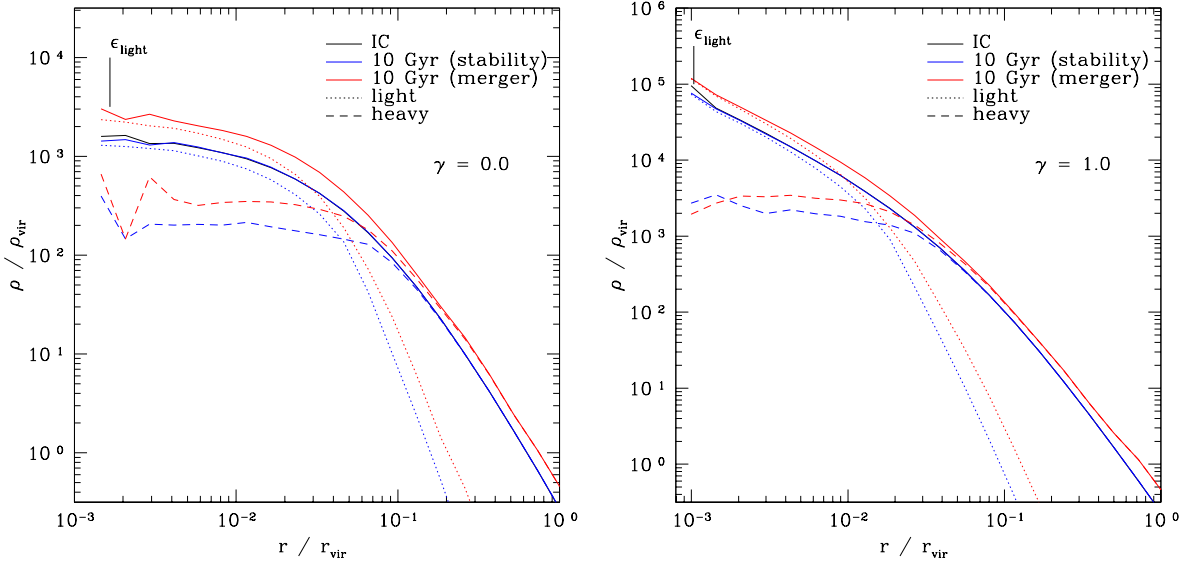


Figure 2.6: Equal profile mergers, left: $\gamma = 0.0$ and right: $\gamma = 1.0$. The profiles are stable over 10 Gyr and the central profile is conserved in both cases.

where cusp means $\gamma = 1.0$ and core is equivalent to the $\gamma = 0.0$ model described above. The following merger set-up was used. We placed the two haloes $600 \text{ kpc} \approx 2 r_{\text{vir}}$ apart and the two haloes had an initial relative radial velocity of $v_{\text{rad}} \approx 150 \text{ km s}^{-1}$ and a relative tangential velocity of $v_{\text{tan}} \approx 50 \text{ km s}^{-1}$. Assuming the two haloes were point masses, this set-up correspond to an eccentricity $e \approx 0.95$ of the orbit consistent with values in cosmological N-body simulations [81]. With this set-up the merger time needed by the two haloes to merge completely was approximately 7 Gyr. We let all three runs evolve to 10 Gyr so that the merger remnant had time to relax.

Figure 2.6 shows the stability of both models and the equal profile mergers after 10 Gyr. Down to a few softening length of the light particles no significant deviations can be seen in the stability tests. The merger remnant has the same profile as the two progenitors except that the local density more or less doubles. We normalise the plots by the values r_{vir} and ρ_{vir} of the progenitor haloes. The deviations in the outer part of the profiles are due to a slightly triaxial shape of the halo there. The remnant just did not have enough time to fully relax in this region.

In figure 2.7, we present the profile of the cusp-core merger after 10 Gyr. The central slope of the steepest progenitor is perfectly preserved and the cored progenitor only contributes significantly in the outer region of the total density profile.

We can therefore confirm the earlier findings that core-core mergers lead to a cored merger remnant while cusp-cusp mergers lead to a cuspy merger remnant with high resolution multi-mass N-body simulations. In cusp-core merges the merger remnant has a final profile corresponding to the steepest progenitor which is in excellent agreement with the prediction by Dehnen [31].

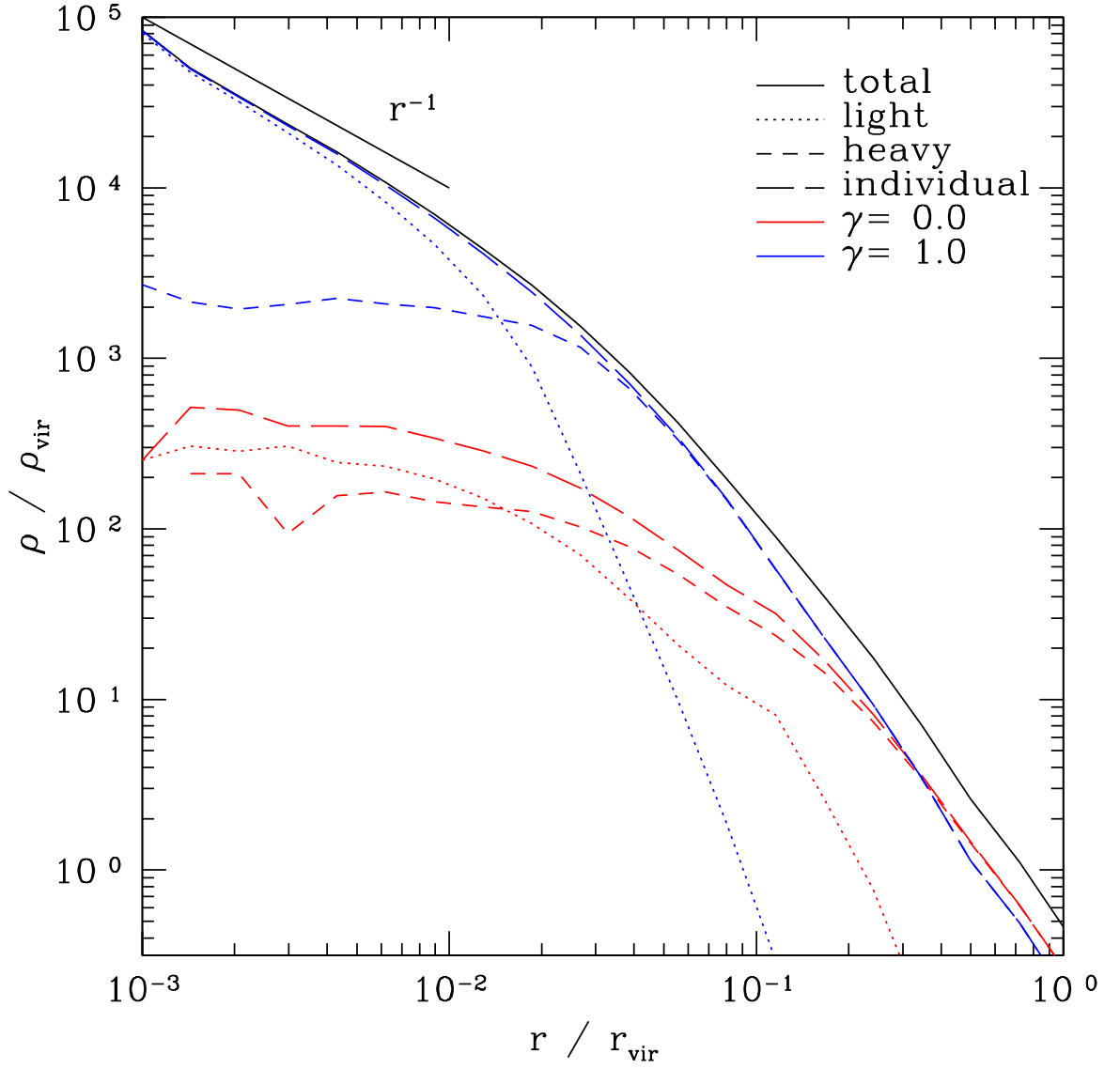


Figure 2.7: Cusp-core merger after 10 Gyr. The central cusp is preserved. Plotted are also the sub-profiles of each particle species in the simulation and the individual profiles of the two progenitors with central slope $\gamma = 0.0$ respectively $\gamma = 1.0$.

2.5 Conclusions

The multi-mass technique for modelling haloes is a simple method in order to perform high-resolution N-body simulations. The following rules of thumb should lead to well behaving structures:

- The mass ratios between particles of neighbouring shells should not be too high. We recommend from $R_M \approx 20 - 30$ for flat profiles up to maximum $R_M \approx 100$ for steep profiles.
- The softening length should scale according to the mass of the particle, i.e. high mass particles should have bigger softening than low mass particles in order to prevent heavy scattering.
- The shell radii should be set at places where the local density profile is steep so that the transition region where different species contribute equally is as small as possible.
- The density profiles are only stable down to the radius r_{res} which depends on the time T_S the simulator wants to simulate. Below that scale, relaxation will lead to flattening of the density profile. For a given computer run time T_S , this implies a minimum effective number of particles.

The multi-mass technique can lead to a significant gain in computer run time for a given resolution scale and is therefore ideally suited for many applications in N-body simulations.

Chapter 3

An optimum time-stepping scheme for N-body simulations¹

3.1 Introduction

Achieving spatial adaptivity in the evaluation of forces in N-body simulations is a well studied problem with many effective approaches based on the use of tree structures and multipole expansions or nested grids and FFT techniques. Such adaptivity in space also comes with a desire to achieve adaptivity in the time integration of these simulations since a large dynamic range in density implies a large dynamic range in time-scales for self gravitating systems ($T \sim 1/\sqrt{G\rho}$). Two very different problems present themselves when trying to achieve this. First, there are no practical (explicit), general purpose (applicable to a wide range of astrophysical problems), adaptive integration techniques known for the N-body problem which are symplectic. By this we mean that the numerical integration is an exact Hamiltonian phase flow very close to the phase flow of the continuous system under study. This is a very desirable property for following systems for longer than a single dynamical time. Such exact preservation of the geometrical properties of the dynamical system is possible for fixed time-step schemes. For general N-body simulations with adaptive time-stepping we have to resort to approximate symplectic behaviour or preservation of time symmetry (a property which is known to lead to very good integration methods). The second problem is that of continuously determining the appropriate time-step for each particle in the simulation so that the error in the integration remains within tolerance while performing the fewest possible force evaluations and minimising the computational overhead. Resolving this second problem is the main focus of this chapter and can be considered independently from methods symmetrizing the time-stepping scheme such as presented in in work by Stadel [144] and Makino et al. [97].

There are several known time-step criteria based on different properties of the simulation (e.g. local density $\rho(r)$, potential $\Phi(r)$, softening ϵ , acceleration a , jerk \dot{a} or even the velocity v of the particle) that are used in state-of-the-art numerical codes [1, 125, 128, 141, 144]. Some of them have a physical motivation, others are just a clever combination of physical properties in order to obtain a criterion which has the physical unit of time. All are an attempt to find an inexpensive way of determining an

¹This chapter is a slightly modified version of Zemp et al. [174].

appropriate time-step for each particle in the simulation. For cosmological simulations, the ad-hoc time-step criterion based on the acceleration and the gravitational softening of the particle ($T \sim \sqrt{\epsilon/a}$) has proven very successful, despite the fact that it is not directly related to the dynamical time in these simulations. One reason why this time-step criterion is thought to work well is that it results in a very tight time-step distribution with very infrequent changes in the time-step of a particle in block time-stepping schemes (power of 2 step sizes; see also section 3.2.2). This hides the evils due to the first problem since the behaviour is more like that of a fixed time-stepping scheme than for other criteria. The price however is that more time-steps are taken in lower density regions of the simulation than would seem to be necessary. Furthermore, while still adequate for the type of simulations that have been performed up to now, which adapt the softening and mass of particles in the highest density regions and thus reduce the time-step somewhat artificially in those regions, this time-stepping scheme is no longer effective in simulations covering a much larger dynamic range.

In state-of-the-art computer simulations, structures can be resolved by $N_{\text{vir}} \approx O(10^7)$ which results in a resolution scale of $r_{\text{res}} \approx O(10^{-3} r_{\text{vir}})$. By comparing the dynamical scales at r_{vir} and r_{res} , we get $T_{\text{dyn}}(r_{\text{vir}})/T_{\text{dyn}}(r_{\text{res}}) \approx O(10^3)$ or even larger for future high resolution simulations. This large dynamical range in time-scales demands an acutely adaptive criteria so that the dense, dynamical active regions are resolved correctly while the simulations remain fast.

However, in a general simulation, such as those used for cosmological structure formation, it is not straightforward to determine the dynamical time of a given particle. This depends on the dominant structure responsible for the orbit of a particle which needs to be quickly determined at each time-step as the particle is advanced. In this chapter we develop a new fast method of determining each particle's true dynamical time using information directly computed in the force evaluation stage of the simulation. This is quite different from using the local dynamical time which fails dramatically under many circumstances, e.g. consider using the local density near the earth to estimate its time-step!

3.2 Dynamical time-stepping

3.2.1 General idea and description

In order to advance a particle in a numerical simulation, we have to choose a particular time-step for each individual particle. Let us consider a particle on a circular orbit in a system with spherical symmetric density profile $\rho(r)$. The dynamical time $T_{\text{dyn}}(r)$ (or orbital time) of this particle at radius r under spherical symmetry is given by

$$T_{\text{dyn}}(r) \equiv 2\pi \frac{1}{\sqrt{G\rho_{\text{enc}}(r)}} , \quad (3.1)$$

where

$$\rho_{\text{enc}}(r) \equiv \frac{M(r)}{r^3} \quad (3.2)$$

is the enclosed density within the radius r and $M(r)$ is the total mass within radius r . The natural choice for a time-step of a particle would therefore be $\Delta T \propto T_{\text{dyn}}$ were we not faced with the difficulty of determining the enclosed density.

For a particle in a given landscape of cosmic structure, the enclosed density should be set, roughly speaking, by the structure that the particle is orbiting about. Within collisionless cosmological simulations this could be some super-cluster scale structure, or an individual dark matter halo, or some substructure within a dark matter halo. Ideally, we would scan the whole sky of the particle and determine the structure that gives the dominant contribution to its acceleration. From this dominating structure, we could determine the enclosed density and hence find the dynamical time of the particle.

Here we have to distinguish two different regimes. First, we have the mean field regime, i.e. particles move in a (slowly) varying potential that is determined by the total mass distribution. The individual particles are only weakly influenced by their direct neighbours and their motions are dictated by the sum of more distant particles. This is ensured by appropriately softening the short range force thereby placing an upper limit on the contribution from an individual particle. In this regime we want the enclosed density to be set by the globally dominating structure. The second regime is the gravitational scattering regime where we would like to follow large angle scattering due to gravitational interactions, i.e. orbits with eccentricity $e \rightarrow 1$. Here it is important to get the contributions from the closest neighbours which dictate the orbital evolution when they are very close and when there is little or no force softening. This means that the enclosed density is often set by some locally dominating particle.

The determination of the enclosed density is quite easy for some simple configurations like the 2-body problem or a particle orbiting an analytically given spherical symmetric structure. However, the generalisation to any given configuration in an N-body simulation is not so straightforward and we present a simple way in which this can be achieved within a tree based gravity code. The specific implementation within other code-types may look somewhat different but the general scheme and spirit of the method stays the same.

3.2.2 Implementation within a tree-code

We use the tree-code PKDGRAV written by Stadel [144, see also section 1.3.5] which allows for an adaptive time-stepping mechanism where each particle can be on a different time-step. The time-steps of the particles are quantized in fractions of powers of two of a basic time-step T_0 (block time-stepping). Therefore, particles on rung n have an individual time-step of

$$\Delta T = \frac{T_0}{2^n}, \quad (3.3)$$

where T_0 is the basic time-step of the simulation and can be chosen by the simulator. As stated previously, our time-stepping criterion is given by,

$$\Delta T_D = \frac{T_0}{2^n} \leq \eta_D \frac{1}{\sqrt{G\rho_{\text{enc}}(r)}}, \quad (3.4)$$

where η_D is a free parameter. Therefore, we need to calculate the enclosed density ρ_{enc} for each particle from information that is available in a tree-code in order to determine its rung.

In hierarchical tree-codes, at every time-step two interaction lists are generated for each particle: a list of multipoles and a list of particles that interact with the given particle. The tree structure in such codes is a hierarchical representation of the mass in the simulation with each subvolume, or cell, being a node in this tree. As we proceed from the root to the leaves of this data structure we get an ever finer mass representation of the simulation. The forces from more distant cells are calculated by using the multipole expansion of the gravitational potential. This expansion makes it clear that a finer mass representation, or smaller cell, is required for nearby regions than for more distant ones if we want uniform relative errors for each multipole contribution to the force. In its simplest form this is realised by a tree-walk algorithm which, for a given cell, decides whether the use of a multipole expansion for this cell satisfies a given error tolerance. If not, this cell is opened and its two or more children are considered in the same way. The opening radius of a cell which sets an error tolerance is defined by

$$r_{\text{open}} = \frac{2}{\sqrt{3}} \frac{r_{\text{max}}}{\theta}, \quad (3.5)$$

where θ is the opening angle and r_{max} is the distance from the centre of mass of the cell to the most distant corner of the cell. The numbers are only geometric factors so that in the case of a cubic cell with homogeneous density $2/\sqrt{3} r_{\text{max}}$ corresponds to the side length of the cube. A cell may only be accepted as a multipole interaction if the particle for which we are calculating the force is further from the centre of mass of the cell than this radius. If a leaf cell (called buckets) needs to be opened, then we calculate the interactions with each of its particles directly (no multipole expansion is used in this case).

At the end of this procedure each particle in the simulation has two interaction lists: 1) a cell list which can be thought of as the long range contributions to gravity and 2) a particle list which accounts for the short range gravitational interactions. The acceleration and the potential energy of each particle are calculated from these two interaction lists. The opening angle varies the ratio of directly calculated forces to those calculated via multipole expansions. It therefore controls force errors and also determines the primary cost of a simulation. For the calculation of the dynamical time of a particle, we generate an additional list of cells containing only the buckets opened by the above procedure which provides a reduced representation of the particle list. The cell list and this additional list, which we call the particle-bucket list, form a complete tiling of the entire simulation volume except for the local bucket of the particle itself, which is not included.

Mean field regime algorithm

We only need to calculate the time-step of a particle when we evaluate the force acting on it. The dynamical time of a particle is then determined according to the following

scheme:

1. Pick out the 0.5 percentile highest values of ρ_{enc} from both the cell and particle-bucket interaction lists. We regard this subset of cells as the centres of dominant contributions to the acceleration of the particle, otherwise called maxima. Once we have added the contributions of the mass surrounding each of these centres we can make a final determination of which is the dominating region and hence set the correct dynamical time-step. The enclosed density for a cell is defined by,

$$\rho_{\text{enc}} = \frac{M_C}{|\mathbf{r}_{\text{PC}}|^3} , \quad (3.6)$$

where M_C is the total mass of the cell and \mathbf{r}_{PC} the vector from the location of the particle to the centre of mass of the cell.

2. For each of these centres, add up all the ρ_{enc} values from the other cells in the list that satisfy both of the following criteria:

$$|\mathbf{r}_{\text{PC}}| \leq 2 |\mathbf{r}_{\text{PCmax}}| \quad (3.7)$$

$$0.75 \leq \frac{\mathbf{r}_{\text{PCmax}} \cdot \mathbf{r}_{\text{PC}}}{|\mathbf{r}_{\text{PCmax}}| |\mathbf{r}_{\text{PC}}|} , \quad (3.8)$$

where \mathbf{r}_{PC} is the vector from the location of the particle to the centre of mass of the cell and $\mathbf{r}_{\text{PCmax}}$ is the vector from the particle to one of the maxima. That means, we add up all the ρ_{enc} values of cells that lie within a spherical viewing cone of opening angle $2\alpha = 2 \arccos(0.75) \approx 83^\circ$ around a maximum cell (C_{max}) with the particle (P) being the apex extending to $2 |\mathbf{r}_{\text{PCmax}}|$.² See also figure 3.1 for the geometric configuration. If the particle would orbit a perfectly spherically symmetric halo at radius r then the dynamical relevant mass would lie in the sphere of radius r centred at the geometric centre of the halo. Therefore, the angle α is chosen so that the volume of the sphere

$$V_S = \frac{4\pi}{3} r^3 \quad (3.9)$$

equals the volume of the spherical cone

$$V_C = \frac{2\pi}{3} (2r)^3 [1 - \cos(\alpha)] \quad (3.10)$$

resulting in

$$\frac{V_S}{V_C} = \frac{1}{4[1 - \cos(\alpha)]} = 1 . \quad (3.11)$$

This is reached for $\cos(\alpha) = 0.75$.

²Adding up the ρ_{enc} values shows less scattering in the determined time-steps than adding up first the masses of the cells and then dividing by the total volume. It also correctly accounts for softened contributions to the force from the region close to P since the ρ_{enc} contributions are reduced there.

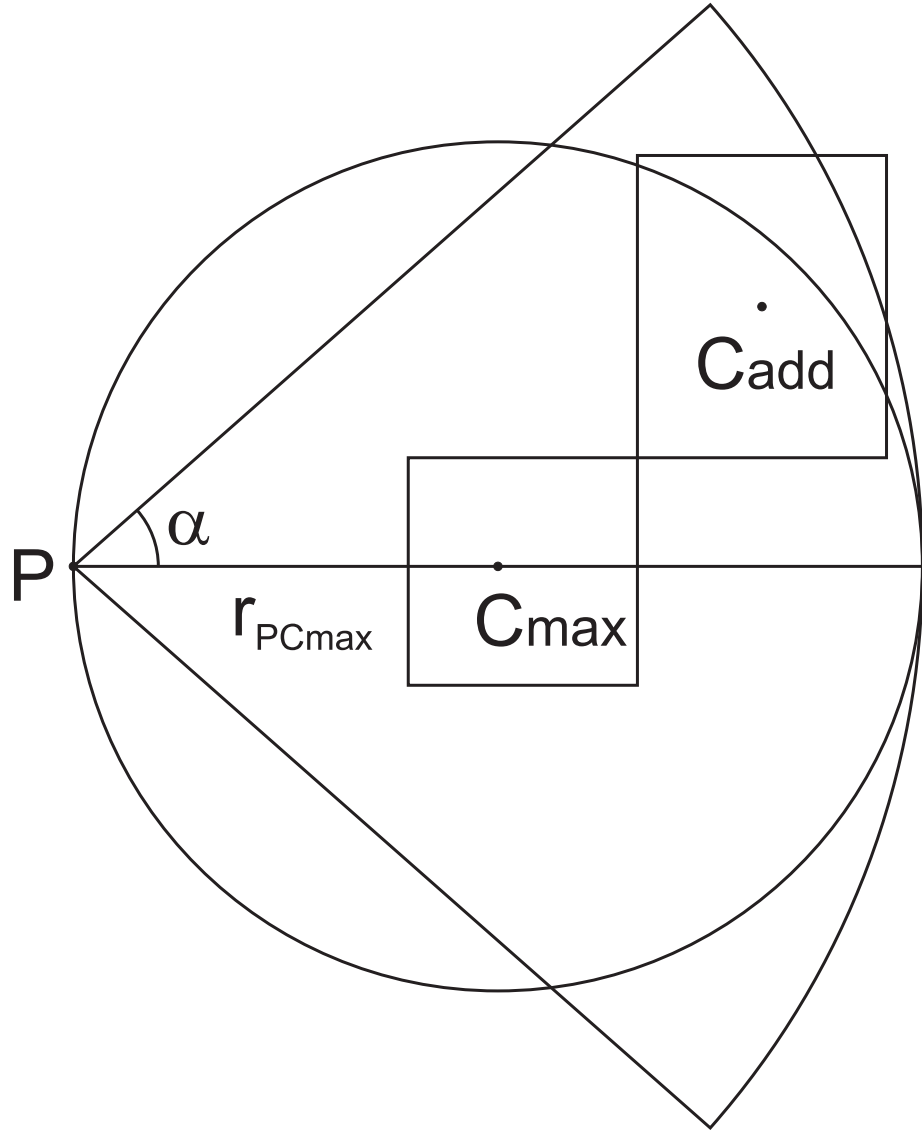


Figure 3.1: Viewing cone for the allowed region of cells to be accepted by the time-step criterion. C_{\max} is the location of the maximum cell. We accept all cells that are within the cone of opening angle $2\alpha \approx 83^\circ$ with the particle (P) being the apex extending to $2 |r_{PC_{\max}}|$.

3. We now have a summed ρ_{enc} of mass contributions about each maximum. Only the largest of these, $\rho_{\text{enc,MF}}$, is used in determining the dynamical time-step of the particle.
4. Add the local density ρ_{local} to the enclosed density $\rho_{\text{enc,MF}}$ of the particle. We do this in order to account for possible contributions from the local bucket of the particle.

As prefactor we use a value of $\eta_{\text{D}} = 0.03$. This choice is motivated by studies of Stadel [144] and is further discussed in section 3.3.5.

Error terms in leapfrog schemes

In computer simulations, the system is not evolved by the true Hamiltonian but by the approximate Hamiltonian

$$H_{\text{A}} = H_0 + \Delta T^2 H_2 + \Delta T^4 H_4 + O(\Delta T^6) . \quad (3.12)$$

In PKDGRAV, particles are evolved by using a kick-drift-kick leapfrog scheme. This means

$$H_0 = H_{\text{D}} + H_{\text{K}} = H \quad (3.13)$$

$$H_2 = \frac{1}{12} \{ \{ H_{\text{K}}, H_{\text{D}} \}, H_{\text{D}} \} - \frac{1}{24} \{ \{ H_{\text{D}}, H_{\text{K}} \}, H_{\text{K}} \} \quad (3.14)$$

where we have split the true Hamiltonian H into a drift (H_{D}) and kick (H_{K}) part. A detailed derivation and an expression for H_4 is given in appendix A. Therefore, the dominant error term is the second order term $E_2 = \Delta T^2 H_2$.

For a 2-body problem, the Hamiltonian is given by

$$H = \underbrace{\frac{p_r^2}{2\mu} + \frac{p_\varphi^2}{2\mu r^2}}_{H_{\text{D}}} - \underbrace{\frac{A}{r}}_{H_{\text{K}}} \quad (3.15)$$

where

$$\mu \equiv \frac{M_1 M_2}{M_1 + M_2} \quad (3.16)$$

is the reduced mass and $A = GM_1 M_2$ and where M_1 and M_2 denote the masses of the two particles. The problem is described by the two coordinates r and φ and their conjugate momenta

$$p_r = \mu \dot{r} \quad (3.17)$$

$$p_\varphi = \mu r^2 \dot{\varphi} = L \quad (3.18)$$

Since the coordinate φ is cyclic, its conjugate momentum is an integral of motion, i.e., the angular momentum,

$$L^2 = \mu a A (1 - e^2), \quad (3.19)$$

is conserved. Here $a = \frac{A}{-2E}$, i.e. $|a|$ is the semimajor axis of the ellipse ($e < 1$) or hyperbola ($e > 1$) and E is the total energy of the orbit. By using a symmetrised time-step,

$$\Delta T = \eta_D \sqrt{\frac{r^3}{G(M_1 + M_2)}} = \eta_D \sqrt{\frac{r^3 \mu}{A}}, \quad (3.20)$$

we can calculate the higher order error term E_2 of the approximate Hamiltonian for a 2-body problem and evaluate it at pericentre of the particle's orbit,

$$E_2^{\text{peri}} = \Delta T^2 H_2 = \frac{1}{24} \frac{(1 + 2e) \eta_D^2 A}{(1 - e) a}. \quad (3.21)$$

We see that the error depends on eccentricity e of the orbit. This allows us to correct for the second order error and control the error at pericentre.

Gravitational scattering regime algorithm

The value of ρ_{enc} is determined in exactly the same way as described in section 3.2.2. However, in order to account for gravitational scattering events we need to consider the close particle interactions in our determination of the dynamical time in more detail. The procedure here is the following: we go through the particle interaction list and pick out the highest value of

$$\rho_{\text{enc,GS}} = C(e) \frac{M_P + M_I}{|\mathbf{r}_{\text{PP}}|^3}, \quad (3.22)$$

where M_P is the mass of the particle, M_I is the mass of the particle in the interaction list, \mathbf{r}_{PP} is the particle-particle distance and

$$C(e) \equiv \frac{1 + 2e}{|1 - e|} \quad (3.23)$$

is the additional factor that corrects for eccentricity of the orbit. The symmetrisation in $\rho_{\text{enc,GS}}$ is to cover cases where unequal mass particles are involved in the interaction. In such cases the heavier particle would be on a much larger time-step than the interacting partner, resulting in momentum conservation problems and unphysical behaviour when the mass ratio is large. The eccentricity of two interacting particles is given by

$$e \equiv \sqrt{1 + \frac{2EL^2}{\mu A^2}}. \quad (3.24)$$

We then compare the two values of $\rho_{\text{enc,MF}}$ and $\rho_{\text{enc,GS}}$. The larger of these two is used when we want to follow gravitational scattering effects.

3.3 Time-stepping criterion tests and behaviour

3.3.1 General properties

In order to see how the dynamical time-step criterion works, we present the time-step distribution in four dark matter haloes, of the $\alpha\beta\gamma$ -models family given by equation (2.1)

3.3 Time-stepping criterion tests and behaviour

with $\gamma = 1.5, 1.0, 0.5$ & 0.0 where γ is the inner slope of the density profile $\rho(r) \propto r^{-\gamma}$. The outer slope is always $\beta = -3$. All haloes have a virial mass of $M_{\text{vir}} = 10^{12} h^{-1} M_{\odot} = 1.429 \times 10^{12} M_{\odot}$ ($h = 0.7$) and are represented by $N_{\text{vir}} \approx 7.5 \times 10^6$ particles within the virial radius. This virial mass corresponds to a virial radius of $r_{\text{vir}} \approx 289$ kpc. We fix the concentration of the profile with central slope $\gamma = 1.0$ to $c_{1.0} = 10$ and the concentrations of the other profiles were chosen so that the maximum circular velocity is reached at the same radius in all haloes. The softening of the particles was $\epsilon = 0.1$ kpc $\approx 3.5 \times 10^{-4} r_{\text{vir}}$ in all haloes.

We compare our new time-step criterion based on the dynamical time with the standard criterion commonly used in N-body simulations. The standard criterion for selecting time-steps in N-body simulations is based on the acceleration of the particle. The rung, n , and time-step taken, ΔT_{S} , for the standard criterion is given by,

$$\Delta T_{\text{S}} = \frac{T_0}{2^n} \leq \eta_{\text{S}} \sqrt{\frac{\epsilon}{|a(r)|}}, \quad (3.25)$$

where ϵ is the softening and a the acceleration of the particle. By default, a value $\eta_{\text{S}} = 0.2$ is generally used. In spherically symmetric systems, we can calculate the radius r_{eq} where the dynamical and standard criteria give the same time-step

$$\Delta T_{\text{D}}^2(r_{\text{eq}}) = \Delta T_{\text{S}}^2(r_{\text{eq}}) \quad (3.26)$$

$$\eta_{\text{D}}^2 \frac{r_{\text{eq}}^3}{GM(r_{\text{eq}})} = \eta_{\text{S}}^2 \frac{\epsilon r_{\text{eq}}^2}{GM(r_{\text{eq}})} \quad (3.27)$$

which results in

$$r_{\text{eq}} = \frac{\eta_{\text{S}}^2}{\eta_{\text{D}}^2} \epsilon, \quad (3.28)$$

independent of the form of the density profile.

In figure 3.2 we plot the time-step criterion distribution of the particles for all haloes as a function of distance from the centre of the halo. Between solid and long dashed lines the values for the dynamical time-step criterion (blue) and following the short dashed line the standard time-step criterion values (red). For a better overview, we only plot 0.1 per cent of the particles randomly selected from the total number of particles in each halo.

As we can see in figure 3.2, the standard criterion follows closely the theoretical curve (short dashed) with $|a(r)|$ calculated numerically. The dynamical time-step criterion also follows closely a band between $\eta_{\text{D}} = 0.02 \dots 0.03$ (long dashed and solid lines) for the theoretical curve with $\rho_{\text{enc}} = \frac{M(r)}{r^3}$. The radius of equal time-steps with the parameters above results in $r_{\text{eq}} = 4.444$ kpc $\approx 1.5 \times 10^{-2} r_{\text{vir}}$.

On the right side of each plot in figure 3.2, we also plot the time-step distribution in three bins at $r_i = r_{\text{vir}}, 10^{-1} r_{\text{vir}}, 10^{-2} r_{\text{vir}}$ of width 0.002 in logarithmic scale. For the dynamical time-stepping scheme, most of the particles lie in the band between the two curves. Of course, we expect a spread in our criterion since our add-up scheme does not recognize perfectly the geometry of the surrounding structure. We note however that

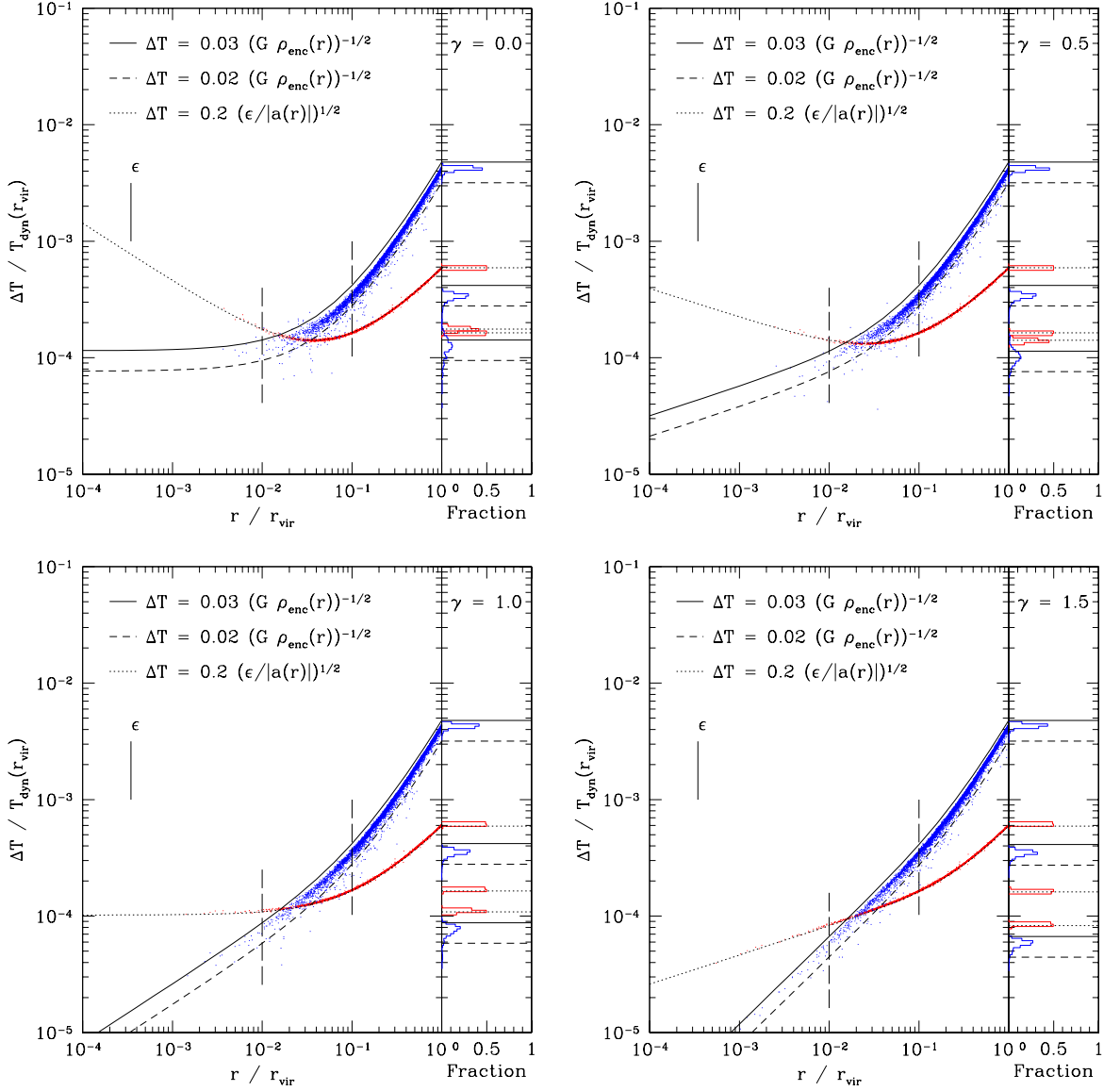


Figure 3.2: We plot the time-step criterion distribution for four profiles with central slope ranging from $\gamma = 0.0 \dots 1.5$. The results for the dynamical and standard time-stepping criteria are shown. Time-steps are in units of the dynamical time at the virial radius $T_{\text{dyn}}(r_{\text{vir}}) \approx 12$ Gyr. For further details see main text.

the add-up scheme is generally more conservative for the choice of time-step at a given radius than the analytical value. In the two flat cases ($\gamma = 0.0$ and $\gamma = 0.5$), the bin at $10^{-2} r_{\text{vir}}$ is close to the resolution limit of the halo and the distribution is therefore quite noisy and relatively broad. Most of the effect due to this broader distribution at small radii is absorbed by the block time-step scheme's way of discretizing the actual time-step taken (see also equation 3.4); the time-step value provided by the criterion is just an upper limit.

With a rather conservative choice of $\eta_D = 0.03$, we sample the orbit of a particle on a circular (tangential) orbit with at least $2\pi/\eta_D \approx 200$ steps. The second curve (short dashed) used a value of $\eta_D = 0.02$ which corresponds to $2\pi/\eta_D \approx 300$ steps per circular orbit.

The situation is a bit more complicated for particles on perfect radial orbits. For a homogeneous sphere, the particle will oscillate through the centre of the sphere and describe therefore a harmonic oscillator with period $T = \sqrt{3\pi/(G\rho)}$ where ρ is the homogeneous density of the sphere.³ If we take this value with $\rho_{\text{enc}} = \rho$ we get for a complete radial orbit between $\sqrt{3\pi}/0.03 \approx 100$ and $\sqrt{3\pi}/0.02 \approx 150$ steps per oscillation. Since our time-step criterion is very adaptive with radius, the dynamical time will decrease in a steep density profile when the particle approaches the centre, so that the effective number of steps is even higher.

The main disadvantage of the standard time-step criterion (3.25) is the bad adaptivity with radius, i.e. the particles are distributed over relatively few rungs. Especially in the profile with $\gamma = 1.0$, the particles inside about ten per cent of the virial radius are all on the same time-step. For flatter central profiles with $\gamma < 1$ where $\rho(r) \propto r^{-\gamma}$, the time-steps even increase inside the radius where the acceleration has its maximum, in clear contradiction to the behaviour of the dynamical time! With the asymptotic scaling of the cumulative mass function under spherical symmetry in the central region

$$M(r) \equiv 4\pi \int_0^r \rho(r) r^2 dr \propto r^{3-\gamma} \quad (\gamma < 3), \quad (3.29)$$

we can calculate the asymptotic radial behaviour in the central region of the standard time-stepping criterion

$$\Delta T_S \propto \sqrt{\frac{1}{|a(r)|}} \propto \sqrt{\frac{r^2}{M(r)}} \propto r^{\frac{\gamma-1}{2}} \quad (\gamma < 3), \quad (3.30)$$

where γ is the inner slope of the density profile, i.e. $\rho(r) \propto r^{-\gamma}$. In contrast, the dynamical time-stepping scheme has the following dependence

$$\Delta T_D \propto \sqrt{\frac{r^3}{M(r)}} \propto r^{\frac{\gamma}{2}} \quad (\gamma < 3). \quad (3.31)$$

³Note that Binney and Tremaine [15] defines the dynamical time as the time needed by the particle to reach the centre which means $T_{\text{dyn}} \equiv \frac{1}{4}T = \sqrt{3\pi/(16G\rho)}$.

The standard criterion can only obtain the correct choice of time-step in the central regions by shifting the above relation, either by choosing a small softening for these particles, or by reducing η_S . This automatically leads to an immense computational expense due to the overly conservative time-steps in the outer parts of the halo or even wrong physical behaviour due to the choice of too small softening for the physical problem (e.g. undesired scattering of particles). The radial scaling of the standard criterion makes it ill suited to the study of the centre of galaxies and in other situations where a very large dynamic range in density needs to be evolved correctly. The dynamical time-stepping technique we present is a much more universal approach to choosing time-steps in self-gravitating systems, since the basic parameters of the method, such as the angle for adding up mass contributions, once determined, are kept fixed for different simulations.

3.3.2 Elliptic 2-body orbits

In order to quantify the performance of our adaptive dynamical time-stepping criterion in the scattering regime, we performed a series of simulations studying the behaviour of high eccentricity 2-body Kepler orbits. After choosing the masses M_1 and M_2 of the two bodies, all other quantities are fixed, i.e. the orbital time of the Kepler orbit is given by,

$$T_K \equiv \sqrt{\frac{a^3(2\pi)^2\mu}{GM_1M_2}} = 2\pi\sqrt{\frac{a^3}{G(M_1 + M_2)}} \quad (3.32)$$

and the initial total energy is calculated by,

$$E_0 \equiv -\frac{GM_1M_2}{2a}. \quad (3.33)$$

We chose a unit system where Newton's gravitational constant $G \equiv 1$ and we fix the orbit in the same way, i.e. the semi-major axis is always $a \equiv 1$. The softening ϵ of the two particles was set to $0.1 d_{\text{peri}}$ in all cases where $d_{\text{peri}} \equiv a(1 - e)$ is the periapsis distance of the Kepler orbit. PKDGRAV treats the forces completely Newtonian if the two particles have a distance larger than 2ϵ which is therefore always the case in these test runs. Initially, the particles were set in a coordinate system where the centre of mass is at rest at the origin and the two particles were at apoapsis configuration along the x -axis. A short summary of the parameters can be found in table 3.2.

We let each run evolve for $1000 T_K$ (T_K was also the basic or longest time-step in the block time-stepping scheme, T_0), measured the total energy E_{1000} after the end of the run and calculated the relative energy shift $(E_{1000} - E_0)/|E_0|$. These values are also listed in table 3.2. From table 3.2, we see that even for a high eccentricity ($e = 0.999$) orbit we still have relative energy conservation on the level of $\approx 10^{-6}$ per orbit. The general behaviour can also be seen in figure 3.3 where we plot the orbit from 0 to T_K and the orbit from $999 T_K$ to $1000 T_K$ for each of the different runs i) - l). The two orbits lie nearly on top of each other except for the $e = 0.99$ case, where the energy gain in the integration was the largest, we can see a small deviation. When we compare the

3.3 Time-stepping criterion tests and behaviour

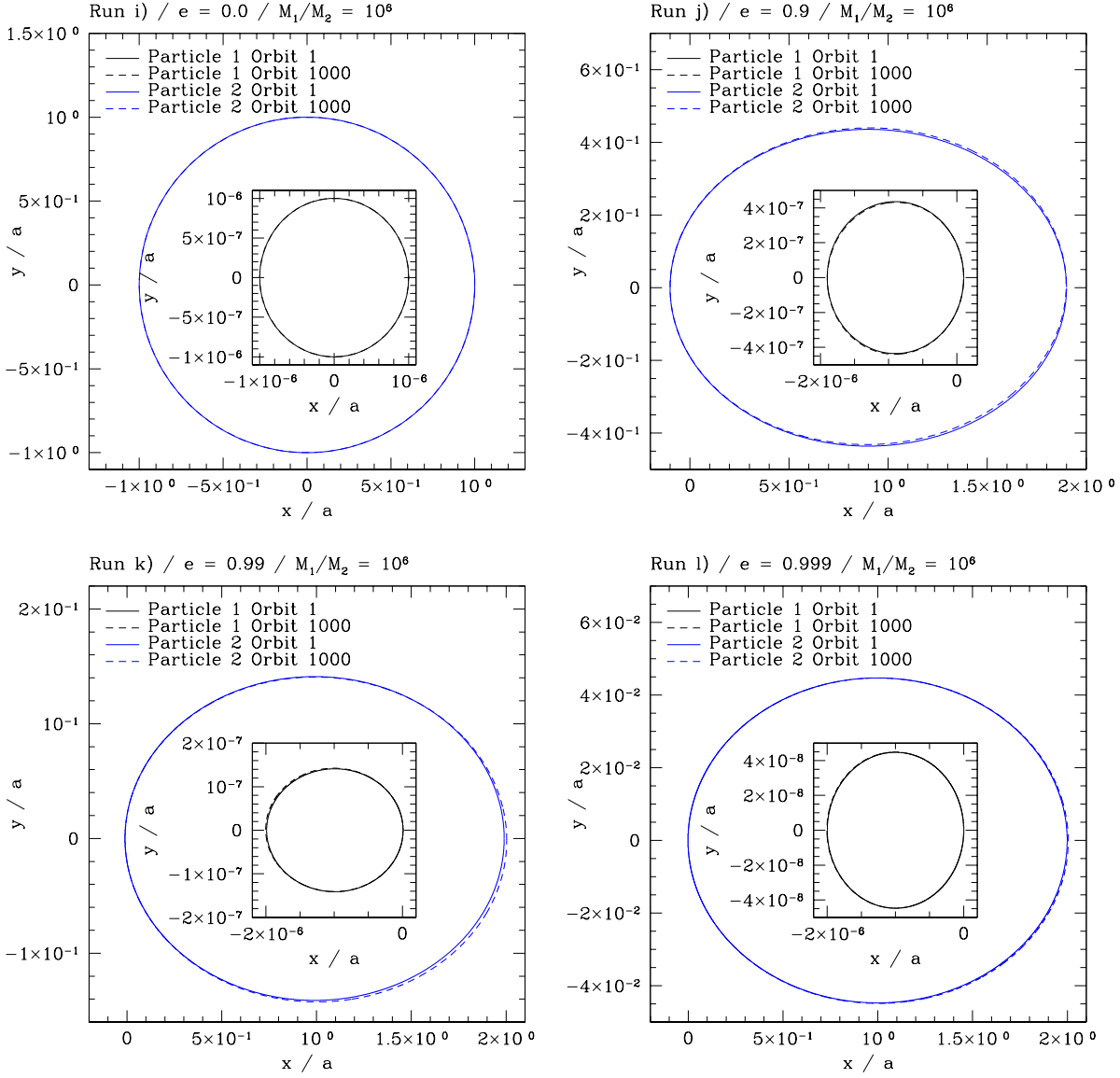


Figure 3.3: Top left: run i), top right: run j), bottom left: run k), bottom right: run l) from table 3.2. We plot the orbit from 0 to T_K (orbit 1) and the orbit from $999 T_K$ to $1000 T_K$ (orbit 1000) for each run. All runs used the dynamical time-stepping scheme with eccentricity correction. We deliberately did not plot the scaling of the two axes constrained in order to make the small deviations visible.

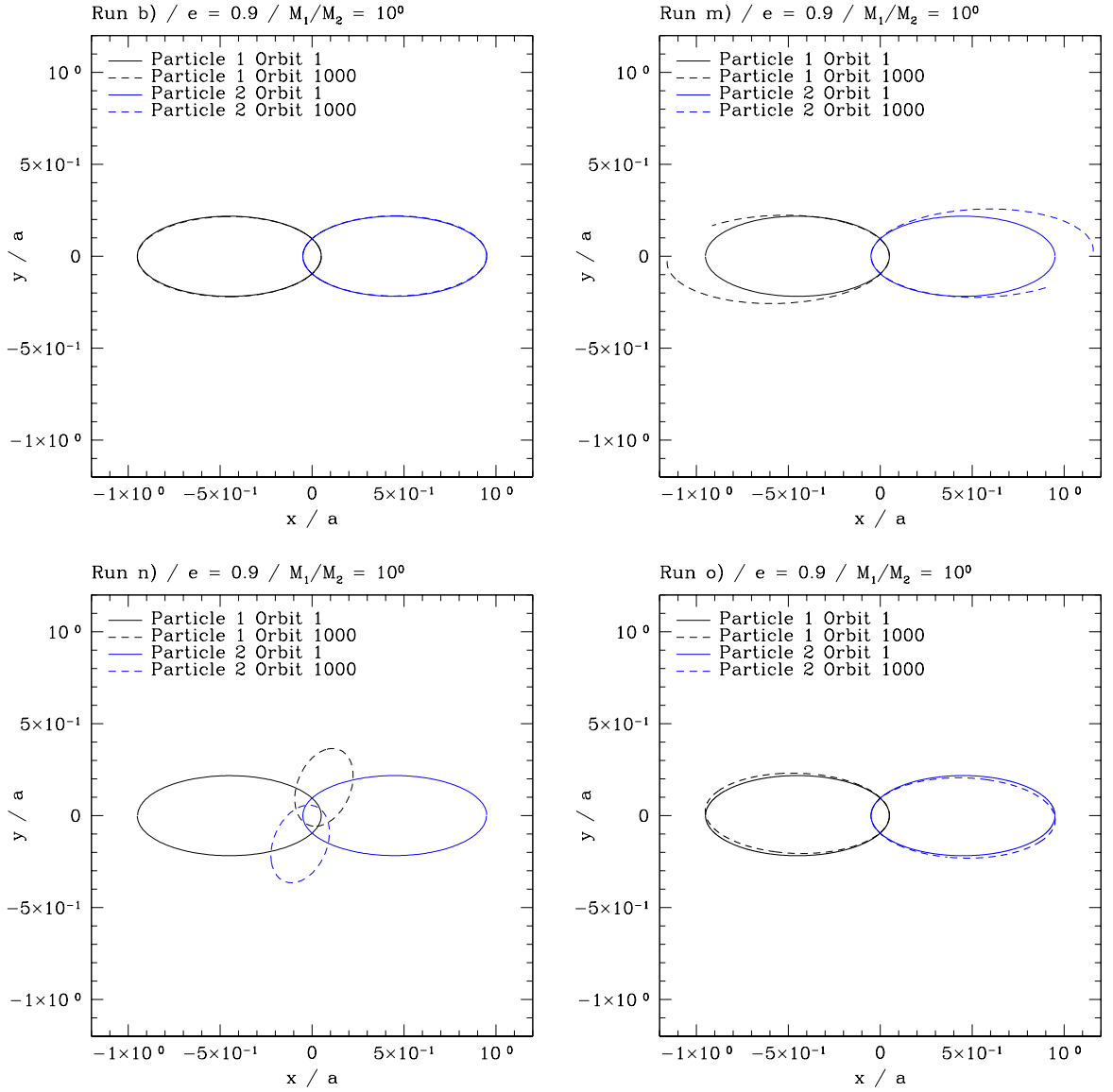


Figure 3.4: Top left: run b), top right: run m), bottom left: run n), bottom right: run o) from table 3.2. Run b) shows the dynamical time-stepping case with eccentricity correction. The orbit is perfectly followed. In run m), we can nicely see the energy gain visually due to the lack of the eccentricity correction in the time-step criterion. Run n) where we tried to resolve a $e = 0.9$ orbit analogue to run b) with the standard time-step criterion. In run o), we see a run where we used a smaller value of $\eta_s = 0.029$ so that the standard criterion initially makes an equal number of steps per orbit as the dynamical time-stepping scheme in run b). For further details see main text.

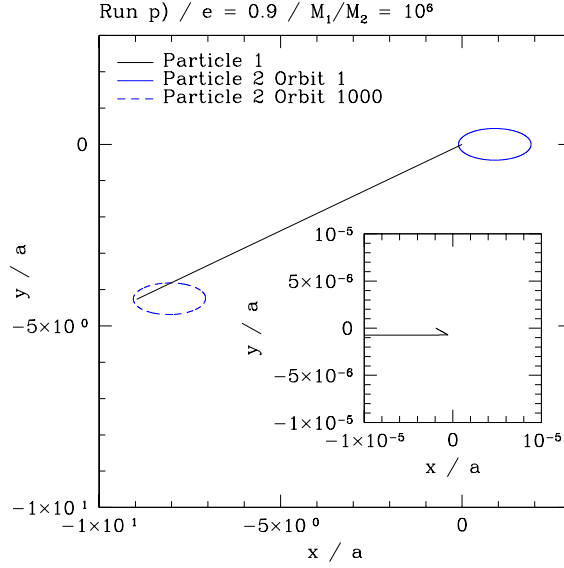


Figure 3.5: Run p) where we tried to resolve an $e = 0.9$, high mass ratio orbit with the standard time-stepping criterion. The heavy particle gets an immense kick and the total energy becomes positive. Thus, the heavy particle drags the light particle with it and the whole system drifts apart. The standard criterion therefore fails completely to follow the orbit correctly.

runs with different mass ratios, we see that the relative energy conservation is nearly the same, i.e. the relative energy conservation depends only on the geometry of the orbit.

In order to illustrate the robustness of our method we have performed some further tests. In run m), we switched off the eccentricity correction in the symmetrised dynamical time-stepping (3.22), i.e. $C(e) = 1$. We see that the energy gain over 1000 T_K is ≈ 240 times larger than in the corresponding run b) with eccentricity correction. This can also be seen visually in figure 3.4. Due to the energy gain, the orbits of both particles become wider.

In run n) we tried to resolve the orbit with the standard time-stepping criterion given by equation (3.25). This criterion depends on the softening length ϵ of the particle and is therefore certainly not ideal in the gravitational scattering regime. We've chosen the same value as in run b) where we had $\epsilon = 0.1 d_{\text{peri}} = 0.01$. From figure 3.4 we see immediately when comparing run n) and b) that the standard criterion can not capture the dynamics of the orbit. The orbits of the two particles become more circular and we get a rotation of the whole system. If we had chosen a somewhat larger softening, so that it is still smaller than half the periapsis distance, it would even look worse since the standard time-stepping scheme directly depends on the softening length ϵ while the dynamical time-stepping scheme would still perform equally well since it has no such dependence.

Of course, the dynamical time-stepping criterion with eccentricity correction uses a lot more steps per orbit than the standard criterion with $\eta_S = 0.2$. Therefore we tried

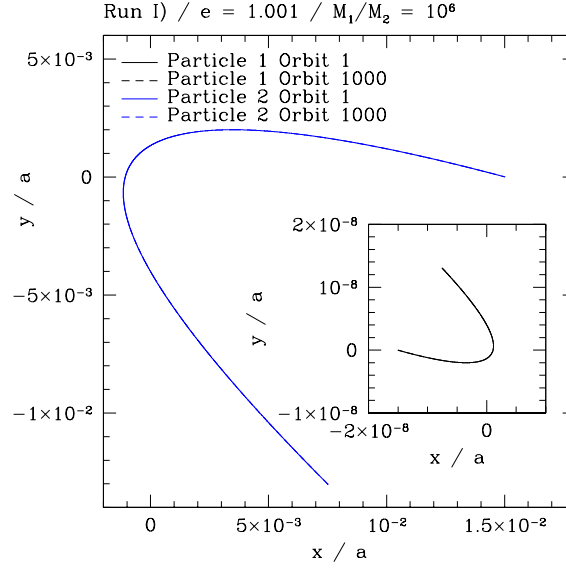


Figure 3.6: The most extreme case, run I), with mass ratio of 10^6 and eccentricity $e = 1.001$. The dynamical time-stepping scheme with eccentricity correction is used. There is no significant evolution over 1000 repeated pericentre passages.

in run o) a run with an equal number of steps per orbit as run b). This is reached for a value $\eta = 0.029$. The energy conservation is still not as good as in the case of the dynamical time-stepping with eccentricity correction b) and there is a small amount of precession of the periapsis.

The whole situation becomes even worse when we try to resolve 2-body orbits with unequal mass particles. Since the standard time-stepping is not symmetric due to the asymmetry in acceleration, it is not able to resolve a high mass ratio 2-body orbit correctly and fails completely. This is shown in figure 3.5. Although the light particle makes $N = 3197$ steps in the first orbit (here N in run p) denotes only the number of steps of the light particle in table 3.2), the heavy particle takes a much larger first step than the light particle. Of course when then the light particle approaches, the heavy particle gets an immense kick, the total energy becomes positive and the whole system drifts apart.

3.3.3 Hyperbolic 2-body orbits

In a similar way, we also tested the new dynamical time-stepping scheme for hyperbolic orbits. Initial conditions were set up such that the line connecting the two particles encloses an angle of $\frac{\pi}{6}$ with the semi-major axis (symmetry axis) of the hyperbola. The time for the particle to reach the periapsis of the orbit is given by

$$T_H = \int_{\frac{\pi}{6}}^{\pi} \frac{\mu r^2(\phi)}{L} d\phi \quad (3.34)$$

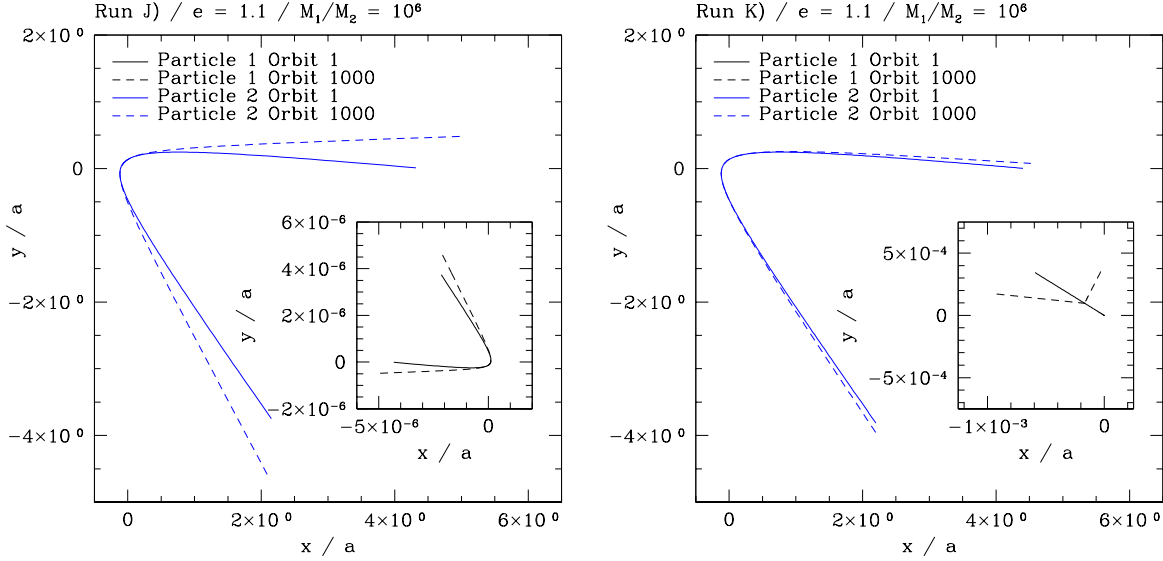


Figure 3.7: Left: run J), right: run K) from table 3.3. In run J) we see the energy gain if the orbit is not followed correctly by not using the eccentricity correction in the dynamical time-stepping scheme. On the right, we see run K) where we used the standard time-stepping scheme. The heavy particle is wandering around in a much larger area than allowed, as can be seen by comparing the scales of the two inset plots.

where $r(\phi)$ describes the angle dependent relative separation of the two bodies. The initial conditions used the same unit system as the elliptic orbit tests and we again set the softening to $0.1 d_{\text{peri}}$ where $d_{\text{peri}} \equiv a(e - 1)$ for hyperbolic orbits. A summary of the different runs can be found in table 3.3.

In order to get an integrated effect, we mirrored the velocities of the particles after $2 T_H$ and let the runs evolve in total for $2000 T_H$ in order to get 1000 pericentre passages.

In figure 3.6, we plot the most extreme case, run I), with mass ratio of 10^6 and eccentricity $e = 1.001$. Over 1000 pericentre passages, there is no visible evolution of the orbit and the relative energy change is of order $O(10^{-5})$ per orbit. For the other cases with lower eccentricities and mass ratios, the new dynamical time-stepping scheme works optimally and we do not show the other orbits here.

We tried again to resolve high mass ratio orbits without eccentricity correction (run J) and the standard time-stepping scheme (run K). The results can be seen in figure 3.7. If we do not correct for the eccentricity (as in run J), the particles gain energy and the orbits become wider. In run K) we see the behaviour of the standard time-stepping scheme. Due to the large mass ratio, the acceleration of the light particle is quite large and therefore it follows a qualitatively correct orbit due to the small time-steps. This is similar to the case p) of the elliptic 2-body orbits where the light particle describes an elliptical orbit about the massive particle, even though this massive particle gets a spurious kick. Once again, the massive particle has a completely incorrect orbit

wandering around in a very large area due to the spurious kicks (compare the scales of the inset plots in runs J and K). The lack of momentum conservation in such cases results in this contrasting behaviour of the two different mass particles. The symmetrization of the time-step criterion restores momentum conservation between the two particles involved in the gravitational scattering event.

3.3.4 Cosmological structure formation

We also tested the performance of the dynamical time-stepping scheme in a cosmological structure formation run. For this purpose, we used a fiducial simulation of the Virgo cluster [61] in a cosmological framework with $\Omega_M = 1$, no cosmological constant i.e. $\Omega_\Lambda = 0$ and $H_0 = 50 \text{ km s}^{-1} \text{ Mpc}^{-1}$. The simulation cube had a box length of $L = 100 \text{ Mpc}$ and the total mass in the cube was $M_{\text{tot}} = 6.937 \times 10^{16} \text{ M}_\odot$. The cluster was resolved using the standard refinement technique [77, 78] so that the particle mass in the highest resolution region was $8.604 \times 10^8 \text{ M}_\odot$ and the softening length of the lightest particles was $\epsilon = 5 \text{ kpc}$. The total number of particles was 1.314×10^6 . The simulation started at redshift $z = 69$ and we evolved the cluster to redshift $z = 0$ with three different time-stepping schemes: one dynamical and one standard time-stepping run and, for comparison, a fixed time-step scheme with 300000 time-steps from $z = 69$ to $z = 0$ (this corresponds to 20000 time-steps down to redshift $z = 5$ in the above described cosmology). With this choice, the fixed time-step length corresponds approximately to the smallest time-step chosen by the dynamical criterion during the whole run. Only for a few particles, the dynamical scheme did choose smaller steps than this fixed time-stepping run.

The virial radius of the resulting cluster was in all cases $r_{\text{vir}} \approx 2 \text{ Mpc}$ (overdensity ≈ 200) and had a final mass of $M_{\text{cluster}} \approx 4.3 \times 10^{14} \text{ M}_\odot$. In figure 3.8, we plot on the top panel the radial density profile for the three runs at redshift $z = 0$. Here $\rho_D(r)$ is the radial density of the run with the dynamical time-stepping scheme, $\rho_S(r)$ the density profile of the run with the standard time-stepping scheme and $\rho_F(r)$ the profile of the fixed time-step run. In the lower panel, the relative difference $(\rho(r) - \rho_F(r))/\rho_F(r)$ is also plotted. The softening of the highest resolution particles correspond to $\epsilon = 5 \text{ kpc} \approx 2.5 \times 10^{-3} r_{\text{vir}}$. As we can see in figure 3.8, the same radial density profile is obtained for the final cluster in this cosmological simulation.

We also compared the substructure mass function at redshifts $z = 0$ and $z = 5$ for the three runs. For that, we used the group finding software skid⁴ with a linking length of $20 \text{ kpc} = 4 \epsilon$ and a density and number cut so that only structures that are virialised and which are represented by at least 100 particles are accepted. In figure 3.9, we plot the mass function $n(M)$ (number of substructures of mass M) as a function of substructure mass M for output at redshifts $z = 5$ and $z = 0$. There is no substantial difference between the mass functions for the different time-stepping schemes.

For these low resolution runs we do not expect to see a significant difference between the three runs since the scale at which the standard scheme begins to take an insufficient

⁴www-hpcc.astro.washington.edu/tools/skid.html

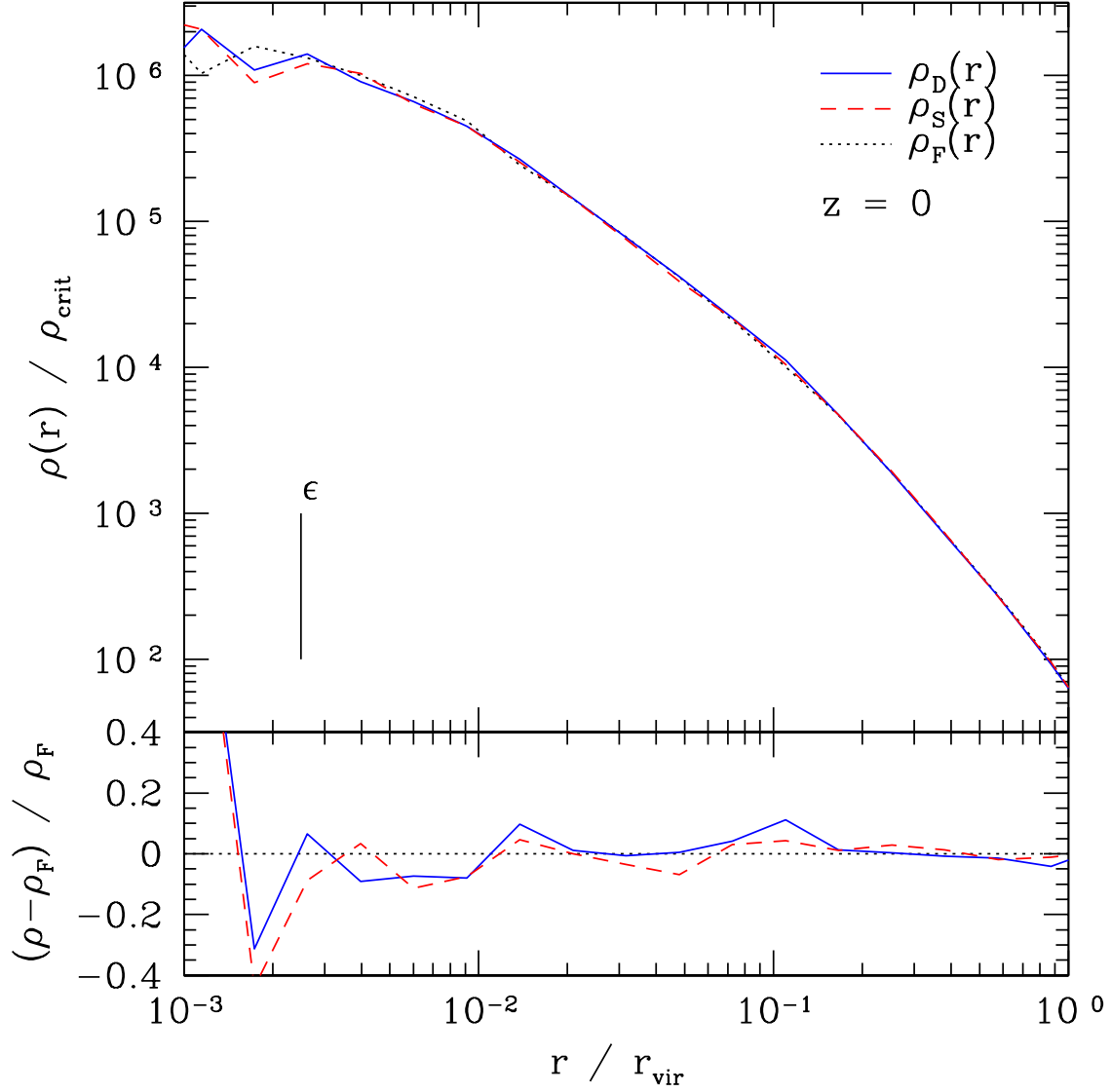


Figure 3.8: Density profiles of the three runs of the Virgo cluster with the different time-stepping schemes at final redshift $z = 0$: $\rho_D(r)$ is the radial density of the run with the dynamical time-stepping scheme, $\rho_S(r)$ the density profile of the run with the standard time-stepping scheme and $\rho_F(r)$ the profile of the fixed time-step run. The profiles are normalised with respect to the critical density ρ_{crit} . On the top panel, the absolute values and on the lower panel the relative differences $(\rho(r) - \rho_F(r)) / \rho_F(r)$ are plotted.

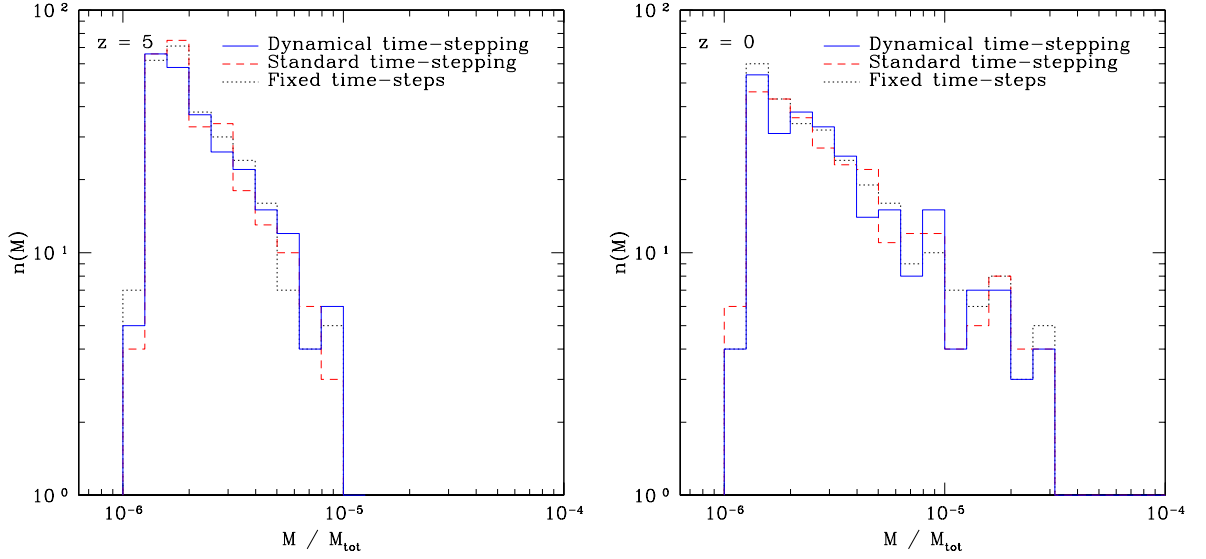


Figure 3.9: Substructure mass function of the Virgo cluster run at redshift $z = 5$ (left) and $z = 0$ (right). There is no substantial difference between the runs with different time-stepping schemes visible.

number of time-steps corresponds approximately to the resolution scale of this simulation. This is just a confirmation that the dynamical time-stepping scheme also works for the extreme dynamics of a cosmological structure formation run.

3.3.5 Dependence on parameters

Softening length ϵ

The standard time-step criterion (3.25) depends directly on the artificial simulation parameter softening length ϵ . There is however no physical basis for this definition. Furthermore, the functional form of the acceleration in centrally flat ($\gamma < 1$) haloes is problematic and can lead to nonsensical time-steps if the resolution is high enough (see figure 3.2). Even a simple 2-body problem is not treated properly by the standard time-stepping scheme, since the time-steps depend on acceleration which is not symmetric and again there is the meaningless dependence on the softening of the particles.

The dynamical time-stepping scheme only depends indirectly on the softening length. If two particles are close enough such that their forces are softened, we also use the softened values for the ρ_{enc} . In this way the scheme also determines an appropriate dynamical time-step when the Green's function deviates from the Newtonian $1/r$. Furthermore, the new dynamical time-stepping scheme may be used without modification in simulations where the softening is set to zero, i.e., where the interactions are never softened.

Force opening angle θ

The opening angle θ determines the weighting of directly calculated forces to force contributions coming from the multipole expansion. This parameter mainly determines the accuracy of the force. By including the terms in the particle-bucket list, the dynamical scheme does not show a significant dependence on the choice of the force opening angle θ .

Cone viewing angle α

We normalised the viewing angle α so that the volume of the sphere and the cone in figure 3.1 are equal. We also tried larger values of $\cos(\alpha) > 0.75$ (i.e. smaller angles) but the resulting time-step distribution did not follow the theoretical curves as well as for the case of $\cos(\alpha) = 0.75$ (especially close to the centre).

Number of maxima

Ideally, one would scan the particle's whole sky for the gravitationally dominating structure. But this would be computationally very expensive. With our choice of the 0.5 percentile largest ρ_{enc} cells in each of the cell and particle-bucket lists we find a good compromise between getting the correct dominating structure (i.e. low scattering of the enclosed density values) and computational speed. Having to consider multiple maxima is the main factor which makes the dynamical time-stepping scheme more expensive than the simple schemes used to-date. However, if we loosen the strict geometrical definition of the viewing cone, then faster schemes which rely on the hierarchical tree structure when scanning the sky for maxima and their surrounding mass become realisable. Such algorithmic improvements are being investigated and will be discussed in future work.

Prefactor η_D

Stadel [144] performed stability tests for a leapfrog scheme in the drift-kick-drift mode. The result was that 2-body orbits became unstable for choices of $\eta_D \geq 0.1$. For these tests, the choice of time-steps was also based on the dynamical time of the 2-body problem.

We performed similar tests with the kick-drift-kick leapfrog scheme and found that $e = 0.9$ orbits become unstable in the mean field regime (i.e. without eccentricity correction) for choices of η_D too large. Of course by choosing a smaller value of η_D , one always gets better precision but the computational costs become larger. With the choice of $\eta_D = 0.03$ we found a compromise between stability and computational costs.

3.3.6 Efficiency

In order to quantify the efficiency of the dynamical time-stepping criterion in comparison with the standard criterion, we can compare the number of force evaluations for a given

problem. In a spherically symmetric halo, the number of particles in a shell at radius r with thickness dr is given by

$$dN_P = \frac{4\pi\rho(r)r^2dr}{M_{\text{vir}}/N_{\text{vir}}} . \quad (3.35)$$

The number of time-steps per time interval τ for each of these dN_P particles at radius r is given by

$$N_D = \frac{\tau}{\eta_D} \sqrt{G\rho_{\text{enc}}(r)} = \frac{\tau}{\eta_D} \sqrt{\frac{GM(r)}{r^3}} \quad (3.36)$$

in the dynamical case. In the case of the standard time-stepping scheme, this is instead given by

$$N_S = \frac{\tau}{\eta_S} \sqrt{\frac{|a(r)|}{\epsilon}} = \frac{\tau}{\eta_S} \sqrt{\frac{GM(r)}{\epsilon r^2}} . \quad (3.37)$$

We do not account for the actual block time-stepping scheme used in PKDGRAV for this numerical estimation.

The number of force evaluations in that infinitesimal thin shell is now simply given by

$$dF_S = dN_P N_S \quad (3.38)$$

respectively

$$dF_D = dN_P N_D . \quad (3.39)$$

The ratio

$$R_E \equiv \frac{dF_S}{dF_D} = \frac{\eta_D}{\eta_S} \sqrt{\frac{r}{\epsilon}} , \quad (3.40)$$

shows that above r_{eq} defined by equation (3.28), i.e. the radius where both time-stepping criteria give the same value, the number of force evaluations at a given radius is always a factor $R_E \propto \sqrt{r}$ larger.

In figure 3.10, we plot the number of force evaluations per Gyr per radius dF_D/dr and dF_S/dr for a dark matter halo with central profile $\gamma = 1.0$ used also in figure 3.2 with $N_{\text{vir}} = 7.5 \times 10^6$. The figure shows the asymptotic behaviour of the curves in the central region given by

$$\frac{dF_D}{dr} \propto r^{2-\frac{3}{2}\gamma} \stackrel{\gamma=1}{\propto} r^{\frac{1}{2}} \quad (3.41)$$

respectively

$$\frac{dF_S}{dr} \propto r^{\frac{5}{2}-\frac{3}{2}\gamma} \stackrel{\gamma=1}{\propto} r^1 . \quad (3.42)$$

In the inner region, i.e at distances smaller than r_{eq} from the centre, more force evaluations are done in the dynamical time-stepping scheme, as expected. Here the standard scheme does not give small enough time-steps to follow the dynamics. Since in most cases of low resolution simulations r_{eq} (due to a clever choice of softening or η_S) is around the resolution scale, the error is typically small. High resolution simulations can however become very slow if one wants to resolve the central region correctly with the standard time-stepping scheme.

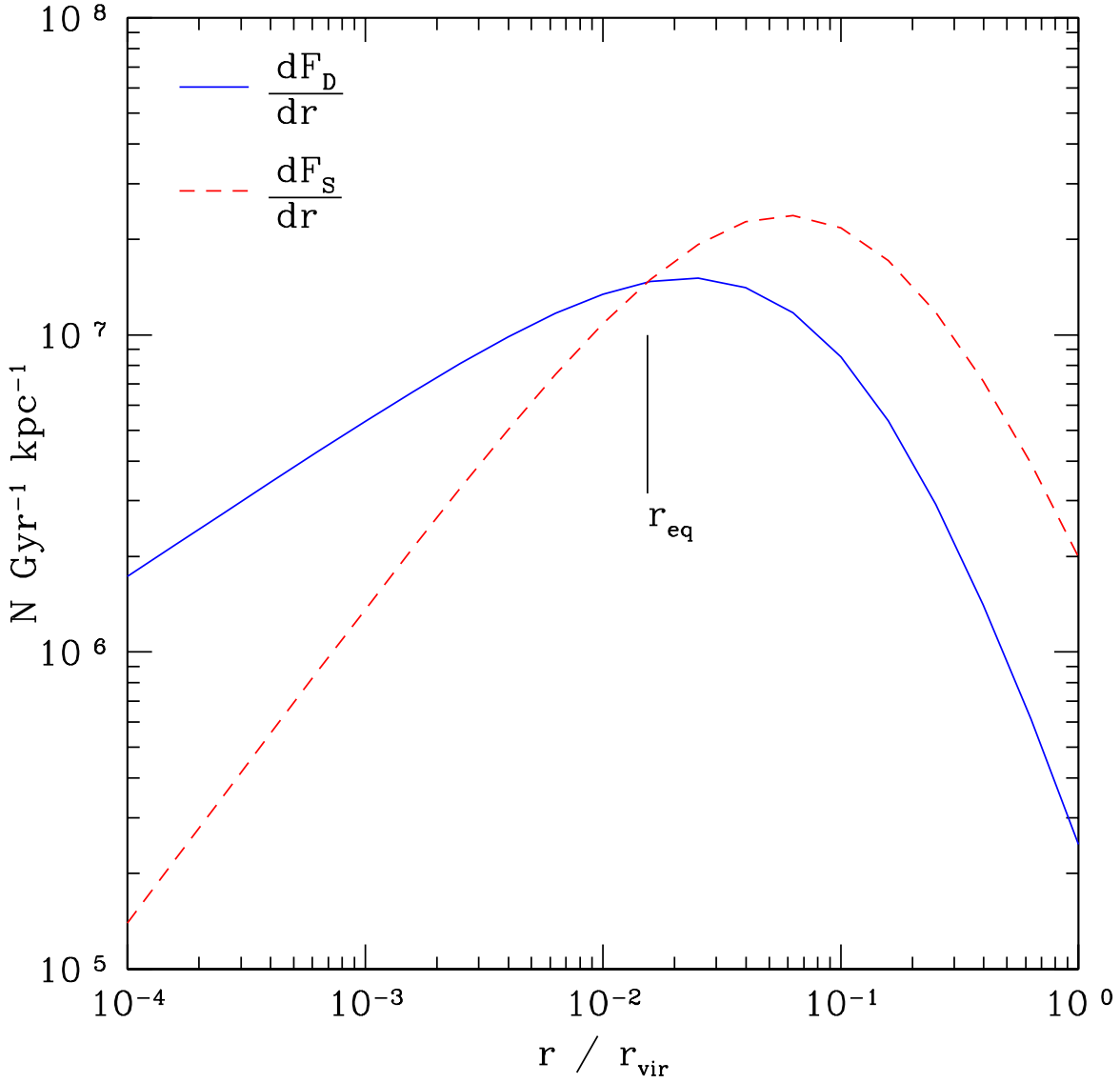


Figure 3.10: Number of force evaluations N per Gyr per radius for the dynamical scheme dF_D/dr respectively dF_S/dr for the standard scheme for a dark matter halo with central profile $\gamma = 1.0$. For infinitesimal thin shells at radii larger than r_{eq} , the standard time-stepping scheme has always a factor R_E (given by equation (3.40)) more force evaluations per Gyr. The inner slope is $\gamma = 1$ and we have therefore the following asymptotic behaviour in the centre: $dF_D/dr \propto r^{\frac{1}{2}}$ and $dF_S/dr \propto r^1$.

N_{vir}	7.5×10^6	7.5×10^8	7.5×10^{10}
F_{D}	7.612×10^8	7.612×10^{10}	7.612×10^{12}
F_{S}	2.336×10^9	7.388×10^{11}	2.336×10^{14}
$\frac{F_{\text{S}}}{F_{\text{D}}}$	3.069	9.705	30.69

Table 3.1: Number of force evaluations per Gyr for an halo with $\gamma = 1.0$ and different resolutions N_{vir} .

In order to illustrate the efficiency gain, we calculate the number of force evaluations per Gyr for three different haloes with central slope $\gamma = 1.0$ that have the same profile and specifications as the one used in figure 3.2 and 3.10. We only changed the number of particles: they are $N_{\text{vir}} = 7.5 \times 10^6$, 7.5×10^8 and 7.5×10^{10} particles within the virial radius. For the first halo we chose a softening length of $\epsilon_1 = 100$ pc $\approx 3.5 \times 10^{-4} r_{\text{vir}}$ and we scaled the softening of the other haloes according to the scaling of r_{imp} given by the solution of

$$r_{\text{imp}} = h(r_{\text{imp}}) , \quad (3.43)$$

where $h(r)$ is the mean particle separation defined by

$$h(r) \equiv \sqrt[3]{\frac{M_{\text{vir}}/N_{\text{vir}}}{\rho(r)}} . \quad (3.44)$$

See also section 2.1 for further details. In other words, r_{imp} is the distance of the innermost particle to the geometrical centre of the halo and scales as

$$r_{\text{imp}} \propto \sqrt[3-\gamma]{\frac{1}{N_{\text{vir}}}} \stackrel{\gamma=1}{\propto} \sqrt{\frac{1}{N_{\text{vir}}}} \quad (3.45)$$

resulting in $\epsilon_2 = 10$ pc and $\epsilon_3 = 1$ pc for the other softenings.

The number of force evaluations per Gyr ($\tau = 1$ Gyr) is given by

$$F_{\text{D}} = \int_{r_{\text{imp}}}^{r_{\text{vir}}} dF_{\text{D}} \quad \text{respectively} \quad F_{\text{S}} = \int_{r_{\text{imp}}}^{r_{\text{vir}}} dF_{\text{S}} , \quad (3.46)$$

and the numerical results can be found in table 3.1. We see that F_{D} scales as $F_{\text{D}} \propto N_{\text{vir}}$ whereas F_{S} scales approximately as $F_{\text{S}} \propto N_{\text{vir}}^{1.25}$ in the case of a halo profile with $\gamma = 1.0$. This specific scaling of F_{S} is due to the scaling of the softening length $\epsilon \propto r_{\text{imp}}$ resulting in the general scaling of

$$F_{\text{S}} \propto N_{\text{vir}}^{1+\frac{1}{2(3-\gamma)}} . \quad (3.47)$$

For a different scaling of the softening, one gets of course a different scaling of F_{S} , e.g. $\epsilon \propto N_{\text{vir}}^{-1/3}$ results in $F_{\text{S}} \propto N_{\text{vir}}^{7/6}$ independent of γ . This again shows the strong dependence of the standard scheme on the softening length ϵ and that the dynamical time-stepping scheme is much more efficient than the standard scheme for high resolution simulations.

3.4 Conclusions

We have developed a physically motivated time-stepping scheme that is based on the true dynamical time of the particle. We also derive an eccentricity correction for a general leapfrog integration scheme. The combination of these schemes allows us to follow quite general dynamical systems that may contain a mixture of collisionless and collisional interacting components. Compared to the standard time-stepping scheme used in many N-body codes it has the following advantages:

- It does not depend directly on ad-hoc parameters such as the softening length ϵ .
- It gives physically correct time-steps in dark matter haloes with arbitrary central cusp slopes.
- It is faster in high resolution simulations.
- It allows orbits with eccentricity $e \rightarrow 1$ to be followed correctly.
- It allows us to follow complex dynamical systems where scattering events may be important.

The main conclusion is that one should use a time-step criterion that is based on the dynamical time. This scheme shows the optimum scaling with the number of particles and always gives a physically motivated time-step.

Run	M_1/M_2	e	T_K	E_0	$(E_{1000} - E_0)/ E_0 $	N	time-stepping scheme	compare with run
a)	1	0	4.443	-5×10^{-1}	2.238×10^{-9}	256	D / ec	
b)	1	0.9	4.443	-5×10^{-1}	-7.278×10^{-4}	2110	D / ec	m), n), o)
c)	1	0.99	4.443	-5×10^{-1}	6.648×10^{-3}	9394	D / ec	
d)	1	0.999	4.443	-5×10^{-1}	2.804×10^{-3}	39143	D / ec	
e)	10^3	0	1.985×10^{-1}	-5×10^2	2.254×10^{-9}	256	D / ec	
f)	10^3	0.9	1.985×10^{-1}	-5×10^2	-7.014×10^{-4}	2110	D / ec	
g)	10^3	0.99	1.985×10^{-1}	-5×10^2	6.648×10^{-3}	9394	D / ec	
h)	10^3	0.999	1.985×10^{-1}	-5×10^2	2.804×10^{-3}	39142	D / ec	
i)	10^6	0	6.283×10^{-3}	-5×10^5	2.242×10^{-9}	256	D / ec	
j)	10^6	0.9	6.283×10^{-3}	-5×10^5	-7.218×10^{-4}	2110	D / ec	p)
k)	10^6	0.99	6.283×10^{-3}	-5×10^5	6.653×10^{-3}	9394	D / ec	
l)	10^6	0.999	6.283×10^{-3}	-5×10^5	2.802×10^{-3}	39142	D / ec	
m)	1	0.9	4.443	-5×10^{-1}	1.730×10^{-1}	398	D / nec	b)
n)	1	0.9	4.443	-5×10^{-1}	-1.263	316	S	b)
o)	1	0.9	4.443	-5×10^{-1}	1.895×10^{-3}	2107	S / $\eta_S = 0.029$	b)
p)	10^6	0.9	6.283×10^{-3}	-5×10^5	1.913	3197	S	j)

Table 3.2: Summary of elliptic 2-body orbit runs a) - p). The columns are mass ratio M_1/M_2 , eccentricity e , orbital time T_K , initial energy E_0 , relative energy change $(E_{1000} - E_0)/|E_0|$, number of steps during the first orbit N , time-stepping scheme: D - dynamical, S - standard, ec - eccentricity correction, nec - no eccentricity correction, run to compare with: b) with m), n) and o) and j) with p).

Run	M_1/M_2	e	T_H	E_0	$(E_{1000} - E_0)/ E_0 $	N	time-stepping scheme	compare with run
A)	1	1.1	2.150	5×10^{-1}	3.009×10^{-3}	1713	D / ec	
B)	1	1.01	2.274×10^{-2}	5×10^{-1}	2.119×10^{-3}	4935	D / ec	
C)	1	1.001	6.709×10^{-4}	5×10^{-1}	-1.298×10^{-2}	15177	D / ec	
D)	10^3	1.1	9.610×10^{-2}	5×10^2	3.009×10^{-3}	1713	D / ec	
E)	10^3	1.01	1.017×10^{-3}	5×10^2	2.119×10^{-3}	4935	D / ec	
F)	10^3	1.001	2.999×10^{-5}	5×10^2	-1.298×10^{-2}	15178	D / ec	
G)	10^6	1.1	3.041×10^{-3}	5×10^5	3.009×10^{-3}	1713	D / ec	J), K)
H)	10^6	1.01	3.216×10^{-5}	5×10^5	2.118×10^{-3}	4935	D / ec	
I)	10^6	1.001	9.488×10^{-7}	5×10^5	-1.298×10^{-2}	15177	D / ec	
J)	10^6	1.1	3.041×10^{-3}	5×10^5	8.336×10^{-1}	296	D / nec	G)
K)	10^6	1.1	3.041×10^{-3}	5×10^5	1.360×10^{-1}	333	S	G)

Table 3.3: Summary of hyperbolic 2-body orbit runs A) - K). The columns are mass ratio M_1/M_2 , eccentricity e , time to reach the pericentre T_H , initial energy E_0 , relative energy change $(E_{1000} - E_0)/|E_0|$, number of steps during the first orbit N , time-stepping scheme: D - dynamical, S - standard, ec - eccentricity correction, nec - no eccentricity correction, run to compare with: G) with J) and K).

Chapter 4

Applications

The development of the multi-mass technique and especially the time-stepping scheme were very time consuming. The author of this thesis was therefore involved in the first application projects that used these new developments as a co-author. In Diemand et al. [38], the multi-mass technique was used in a cosmological structure formation run in order to resolve the resulting density profile of a high resolution cluster down to one per mill of the virial radius. Goerdt et al. [64] used multi-mass models in order to test a potential explanation of the presence of the five globular clusters at approximately 1 kpc distance from the centre of the Fornax dwarf spheroidal galaxy. In this chapter we present a summary of these projects.

4.1 Cusps in cold dark matter haloes¹

4.1.1 Introduction

Recently a great deal of effort has gone into high resolution simulations which have revealed density profiles of cold dark matter haloes down to scales well below one per cent of the virial radius [34, 54, 117, 129, 149]. But the form of the profile below approximately 0.5 per cent of the virial radius remained unclear and there was no clear evidence for a cusp in the centre, i.e. no significant inner region with a constant logarithmic slope. Galaxy cluster haloes would be the ideal systems to resolve cusps numerically because of their low concentration. In a galaxy or dwarf halo the inner power law is much harder to resolve because it lies at a smaller radius relative to the size of the system.

The existence of a core or a cusp in the centre of cold dark matter haloes has important observational consequences and is the crucial point in many tests of the cold dark matter theory. Comparisons of dark matter simulations to rotation curves of low surface brightness galaxies seem to favour constant density cores for most observed systems [28, 48, 107, 134, 139, 148, 157]. But these comparisons still depend to some extent on extrapolations of the simulated profiles toward the centre: Stoehr [145] extrapolate to a constant density core and claim that the discrepancy to low surface brightness galaxy rotation curves is much smaller than previously believed.

The strength of the γ -ray signal from dark matter annihilation depends on the square of the dark matter density and the calculated flux values spread over several orders of

¹Original publication: MNRAS, 364, 665 (2005) [38]

magnitude, depending on how one extrapolates the density profiles from the known, resolved regions down into the centres of the galactic halo and its subhaloes [12, 18, 126, 146]. Small, very abundant, Earth to Solar mass subhaloes could be very luminous in γ -rays if they are cuspy [37].

The highest resolutions in cosmological simulations are reached with the widely used refinement procedure [13]: first one runs a simulation at uniform, low resolution and selects haloes for re-simulation. Then one generates a new set of initial conditions using the same large scale fluctuations at higher resolution and additional small scale fluctuations in the selected region. With this technique Navarro et al. [116] were able to resolve many haloes with a few ten thousand particles and to infer their average density profile which asymptotes to an $\rho(r) \propto r^{-1}$ cusp. Other authors used fitting functions with steeper ($\rho(r) \propto r^{-1.5}$) cusps [52, 62, 110, 112]. Small mass cold dark matter haloes have higher concentrations due to their earlier collapse [116] but the slopes of the inner density profiles are independent of halo mass [27, 113]. Open, standard and lambda cold dark matter (Λ CDM) cosmologies, i.e. models with $(\Omega_M, \Omega_\Lambda) = (0.3, 0.0)$, $(1.0, 0.0)$ and $(0.3, 0.7)$ yield equal inner profiles [53, 54]. There is some indication that models with less small scale power like warm dark matter lead to shallower inner profiles [26, 129]. Different equations of state of the dark energy component lead to different collapse times and halo concentrations but it is not clear yet if it also affects slopes well inside of the scale radius [86, 92]. Most current simulations do not resolve a large enough radial range to determine both the concentration and the inner slope; at the current resolution these parameters show some degeneracy [84].

Recently a large sample of Λ CDM haloes resolved with a million and more particles was simulated [57, 117, 129, 142, 149] and the best resolved systems contain up to 25 million particles [34, 54]. But even these very large, computationally expensive simulations resolved no inner region with a constant logarithmic slope.

Navarro et al. [117], Stoehr [145], Stoehr et al. [146] introduced cored profiles which seem to fit the simulation data better than the cuspy profiles proposed earlier by Navarro et al. [116] and Moore et al. [112]. This better fit was interpreted as indication against cuspy inner profiles. However these cored profiles have one additional parameter and therefore it is not surprising that they fit the data better. Diemand et al. [34] showed that an $\alpha\beta\gamma$ -profile (see equation (2.1)) with the inner slope as additional free parameter fits the highest resolution profiles just as well as cored profiles. Some theoretical arguments seem to favour cusps [14, 67] but make only vague predictions about the inner slopes. A recent model combines simulation results and analytical arguments to predict an inner slope of -1.27 [6]. At the moment higher resolution simulations seem to be the only way to decide the core versus cusp controversy.

We present simulations of one of the galaxy clusters from Diemand et al. [34] with two orders of magnitude better mass resolution. Our results give strong support to cuspy inner profiles. This increase in resolution was made possible with only a moderate increase in computational cost by using the multi-mass refinement technique (see section 2).

Name	D5	D12	DM25	DM50
$N_{\text{vir}}^{\text{eff}}$	1.0×10^6	1.4×10^7	1.3×10^8	1.0×10^9
Multi-mass refinement	no	no	yes	yes
z_{Start}	52.4	43.3	52.4	59.3
z_{End}	0	0	0.8	4.4

Table 4.1: Summary of cluster models. The rows are effective number of particles within virial radius $N_{\text{vir}}^{\text{eff}}$, application of multi-mass refinement, start redshift z_{Start} and end redshift z_{End} .

4.1.2 Numerical methods

Often in cosmological N-body simulations one uses high resolution particles only where one halo forms and heavier particles in the surroundings to account for the external tidal forces. One usually tries to define a large enough high resolution region to minimize or avoid mixing of different mass particles within the region of interest. Here we apply the multi-mass technique to increase the resolution in the centre of one cluster halo in a cosmological N-body simulation.

The refinement procedure is usually applied to entire virialised systems, i.e. one marks all particles inside the virial radius of the selected halo and traces them back to the initial conditions. Then one refines the region that encloses the positions of the marked particles. Usually the region is further increased to prevent any mixing of low resolution particles into the virial radius of the final system. But with this procedure only between one fourth to one third of all the high resolution particles end up in the cluster.

If one is only interested in the inner regions of a halo it is possible to use the multi-mass technique: instead of refining the whole virialised system we only refine the region where the inner particles come from. This allows to reduce the size of the high resolution region considerable, because most of particles that end up near the centre of the system start in a very small region, compared to the region which one finds by tracing back all the particles inside the virial radius. Using this technique it is possible to reduce the computational cost of a cold dark matter cluster simulation by at least one order of magnitude at equal force and mass resolution in the inner region.

Here, we applied the multi-mass refinement to the cluster D from Diemand et al. [34]. This cluster is well relaxed and isolated at $z = 0$ and has an average density profile and inner slope close to the mean value. First we marked all particles within one per cent of the virial radius in the final halo and traced them back to the initial conditions. Then we added all particles within one comoving Mpc of a marked particle to the set of marked particles, and finally we added all particles which lie on intersections of any two already marked particles on the unperturbed initial grid positions. After these two steps there was a region with a fairly regular triaxial boundary which contained only marked particles. The number of marked particles grew by almost a factor of eight during these additions, but it was still more than a factor of two smaller than the number of particles in the final cluster and a factor of ten smaller than the original high resolution volume

used in Diemand et al. [34].

With an effective mass resolution corresponding to 1.3×10^8 and 1.0×10^9 particles inside the virial radius of a cluster, the models DM25 and DM50 are the highest resolution Λ CDM simulation performed so far. Due to the large number of particles and the corresponding high force and time resolution these runs took a large amount of run time. Fortunately the inner profiles of cold dark matter clusters are already in place around redshift $z = 1$ and evolve little between $z = 4$ and $z = 0$ [54, 129, 149]. Therefore one does not have to run the simulations to $z = 0$ to gain insight into the inner density profile. We stop DM50 at $z = 4.4$, DM25 at $z = 0.8$ and use the medium resolution runs D5 and D12 (for which the multi-mass technique was not applied) to quantify the low redshift evolution of the density profile of the same cluster. The D5 model has a resolution of 1.0×10^6 particles and the D12 version was resolved with 1.4×10^7 equal mass particles.

All the runs were evolved with PKDGRAV (see section 1.3.5) from redshift z_{Start} to z_{End} given in the summary of the models in table 4.1.

4.1.3 Results

Run DM25 had an effective resolution corresponding to 127 million particles within the virial radius and a softening length of $0.48 \times 10^{-3} r_{\text{vir}}$. At this up to now unmatched resolution the inner slope is roughly constant from the resolved radius (see figure 4.1) out to about one per cent of the virial radius of the final cluster. Run D12 resolved the same cluster with 14 million particles and showed no convergence to a constant inner slope. This indicates that there is a cusp in the centres of cold dark matter clusters and it becomes apparent only at this very high numerical resolution. The non-constant slopes just near the convergence scale are probably due to the first signs of numerical flattening that set in at this scale. At higher densities below the resolved scales one cannot make any robust predictions yet, but if one has to extrapolate into this region figure 4.1 motivates the choice of a cusp $\rho(r) \propto r^{-\gamma}$ with $\gamma \simeq 1.2$.

Mass accretion histories show that the inner part of cold dark matter haloes is assembled in an early phase of fast accretion [156, 163, 175] and recent high resolution simulations revealed that the inner density profile does not evolve at low redshift [54, 129, 149]. Figure 4.1 confirms that the inner density profile of runs D12 does not change from $z = 0.8$ to $z = 0$.

Therefore in run DM50 we focused our computational effort even more on the early evolution of the inner profile. We refined the inner region of the most massive progenitor identified in run DM25 at $z = 4.4$. Since the refinement region needed is much smaller than the one of DM25 and we only ran the simulation to $z = 4.4$, it is feasible to go to a much better mass and force resolution. The high resolution particles in run DM50 were a billion times lighter than the final cluster.

Figure 4.2 shows that the density profile of run DM50 at $z = 4.4$ is cuspy down to the resolved radius (one per mill of the final virial radius). As in run DM25 the slopes begin to shallow just at the converged scale due to numerical flattening. The profile of DM50 at $z = 4.4$ supports the finding from run DM25 that the inner profile follows a

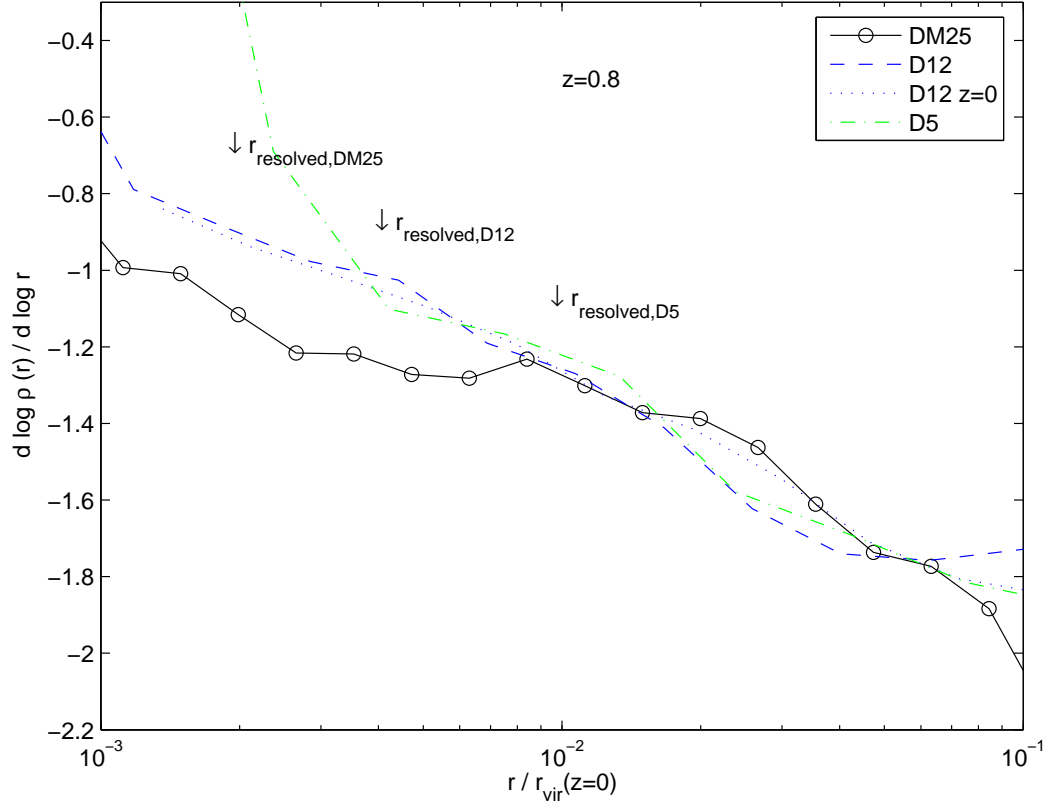


Figure 4.1: Logarithmic slope of the density profile of run DM25 at $z = 0.8$. The slopes of runs D5 and D12 at $z = 0.8$ and $z = 0$ for D 12 are also shown for comparison. The arrows indicates the estimated convergence radii. Note that although the densities at the converged scales are within ten per cent the density gradients can already be substantially smaller.

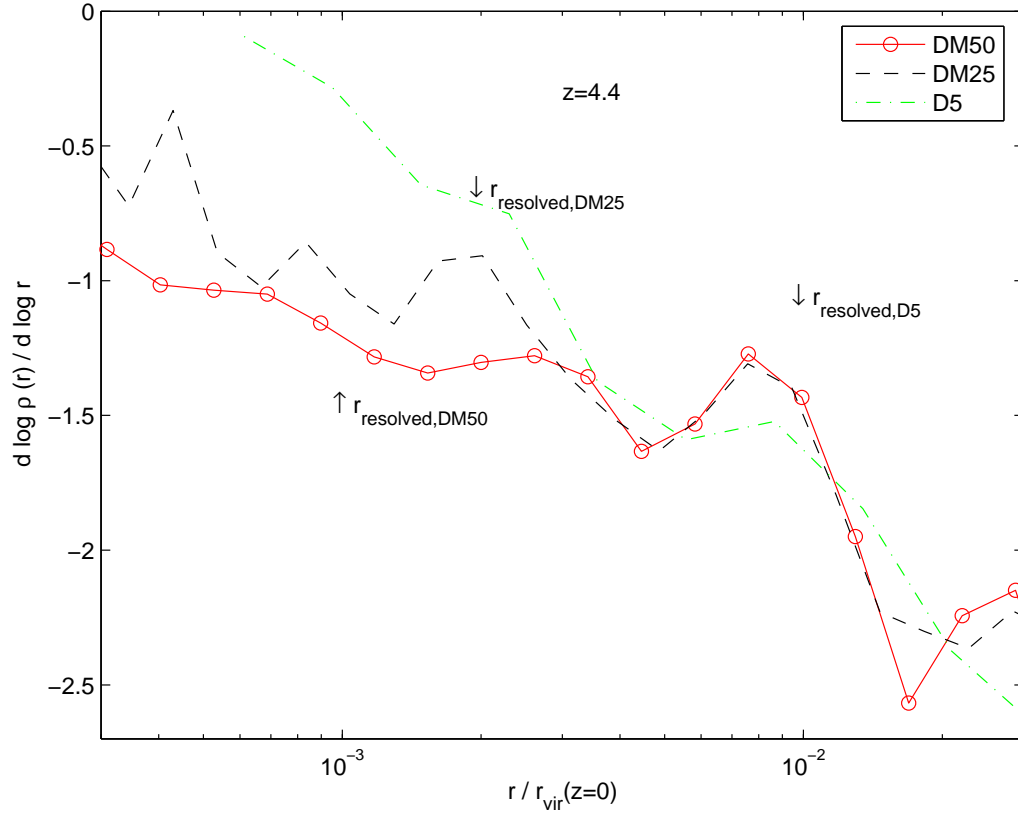


Figure 4.2: Logarithmic slope of the density profile of run D5, DM25 and DM50 at $z = 4.4$. The arrows indicates the estimated convergence radii. A constant inner slope of about -1.2 is evident in the highest resolution run DM50. The increase of the slopes around the resolved radii is due to the onset of numerical flattening.

steep power law $\rho \propto r^{-1.2}$. At the higher resolution of run DM50 we find substantially higher physical densities in the cluster centre at $z = 4.4$ compared to lower resolution runs like DM25. This suggests that a run like DM50 evolved to low redshift would also yield substantially higher central densities as currently resolved in the centres of runs like D12 and DM25.

Now we went one step further and used the information from all the D-series runs to try to estimate the density profile one would obtain if one simulates this cluster with a billion particle all the way to present time, a run which would be possible but extremely expensive with today's computational resources. From figure 4.3 one finds that the density profile of run DM25 near its resolution scale shifts upward by a constant factor of 1.4 from $z = 4.4$ to $z = 0.8$. The density around $0.01 r_{\text{vir}}(z = 0)$ is constant from $z = 0.8$ to $z = 0$, see run D5 in figure 4.3. The inner density profile slopes are constant even longer, i.e. from $z = 4.4$ to $z = 0$, see figures 4.1 and 4.2. Therefore we estimated the $z = 0$ profile of run DM50 by rescaling the $z = 4.4$ profile of DM50 by a factor 1.4 and using the $z = 0$ profile of run D12 outside of $0.005 r_{\text{vir}}(z = 0)$ (see figure 4.3). The extrapolated $z = 0$ profile of run DM50 should be regarded as a best guess for the density profile of an average cold dark matter cluster resolved with a billion particles. A (multi-mass) simulation with this (effective) resolution evolved to redshift zero would be needed to check the accuracy of the estimate performed here.

We fitted one cuspy and two recently proposed cored functions to the density profile of the tentative $z = 0$ extrapolation from run DM50. From the arguments above we expected the cuspy function to work better in the inner part but we tried to fit also the cored profiles for comparison.

As cuspy density profile, we used a general $\alpha\beta\gamma$ -profile given by equation (2.1). If one takes α , β and γ as free parameter one encounters strong degeneracies, i.e. very different combinations of parameter values can fit a typical density profile equally well [84]. Therefore we fixed the outer slope $\beta = 3$ and the turnover parameter $\alpha = 1$. We fitted the three parameters γ , r_s and ρ_0 to the data.

Navarro et al. [117] proposed a different fitting function which curves smoothly over to a constant density at small radii:

$$\ln(\rho_N(r)/\rho_0) = (-2/\alpha_N) [(r/r_s)^{\alpha_N} - 1] \quad (4.1)$$

α_N determines how fast this profile turns away from a power law in the inner part. Navarro et al. [117] found that α_N is independent of halo mass and $\alpha_N = 0.172 \pm 0.032$ for all their simulations, including galaxy and dwarf haloes.

Another profile that also curves away from power law behaviour in the inner part was proposed by Stoehr et al. [146]:

$$\rho_{\text{SWTS}}(r) = \frac{v_{\text{max}}^2}{4\pi G} 10^{-2a_{\text{SWTS}} [\log(\frac{r}{r_{\text{max}}})]^2} \frac{1}{r^2} \left[1 - 4a_{\text{SWTS}} \log\left(\frac{r}{r_{\text{max}}}\right) \right] \quad (4.2)$$

where v_{max} is the peak value of the circular velocity, r_{max} is the radius of the peak and a_{SWTS} determines how fast the profile turns away from an power law near the centre. Stoehr et al. [146] found that cluster profiles are well fitted with this formula using a_{SWTS} values between 0.093 and 0.15.

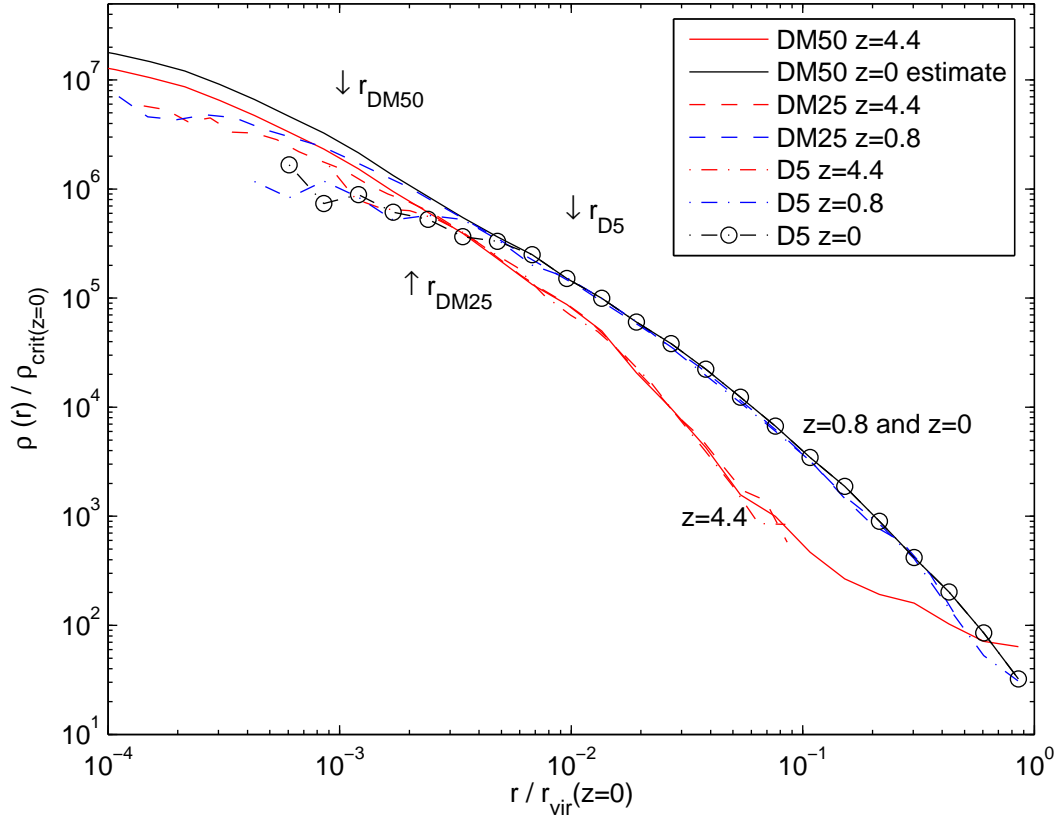


Figure 4.3: Density profiles in physical coordinates at redshifts 4.4, 0.8 and 0. Arrows mark the resolved scales of each run. The densities in the inner part do not evolve between $z = 0.8$ and $z = 0$ and the inner slopes remain constant even from $z = 4.4$ to $z = 0$. Using these observations we are able to estimate the final profile of a billion particle halo (upper solid line).

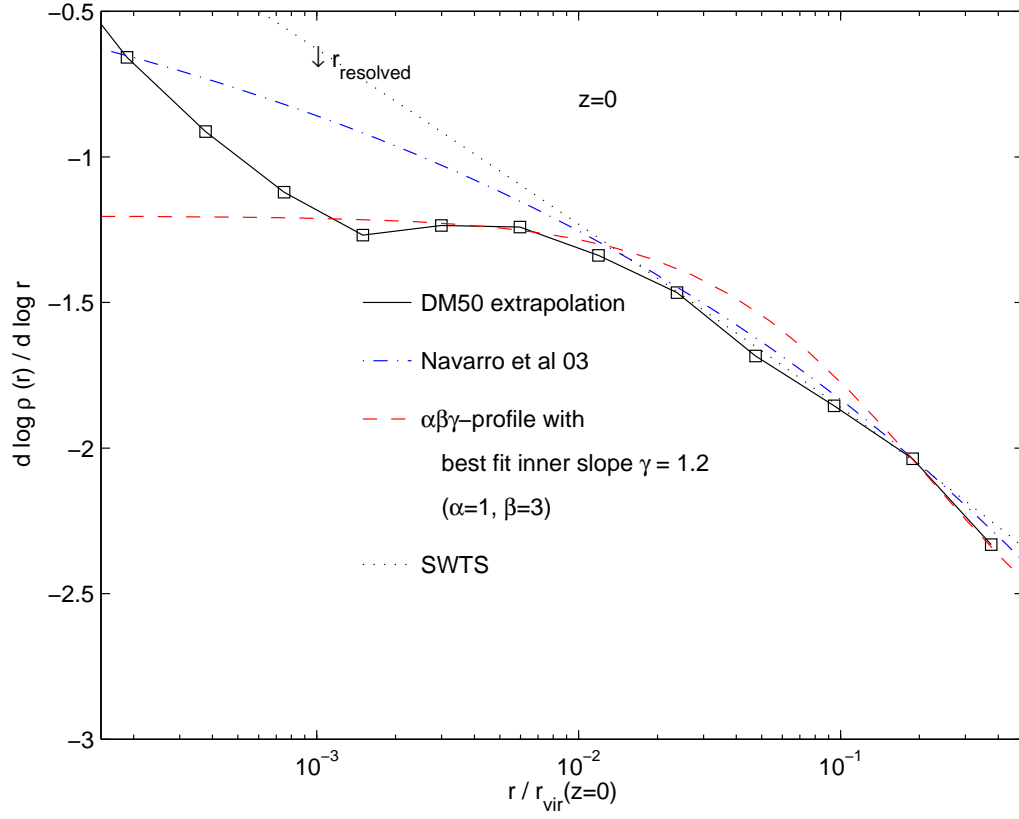


Figure 4.4: Logarithmic slope of the extrapolated DM50 density profile at $z = 0$ and of the fitted density profiles.

Figure 4.4 shows the slope of the extrapolated DM50 profile at $z = 0$ in comparison with the slopes of the best fits. It is evident that in the inner part the cuspy profile with $\gamma = 1.2$ describes the real density profile better.

4.2 Does the Fornax dwarf spheroidal have a central cusp or core?²

4.2.1 Introduction

The Fornax dwarf spheroidal is a dark matter dominated satellite orbiting the Milky Way. It has five globular clusters that are at a projected distance from the centre of 1.60, 1.05, 0.43, 0.24 and 1.43 kpc [93] as well as further substructure at a projected distance of 0.67 kpc [25]. These star clusters move within a dense background of dark matter and should therefore be affected by dynamical friction, causing them to lose energy and spiral to the centre of the galaxy. We will show later that, if Fornax has a cosmologically consistent density distribution of dark matter, the orbital decay time-scale of these objects from their current positions is approximately 5 Gyr. This is much shorter than the age of the host galaxy, presenting us with the puzzle of why these five globulars have not merged together at the centre forming a single nucleus [152, 153].

Several groups have studied the origin of nuclei in galaxies: e.g. Lotz et al. [91] carried out Monte-Carlo simulations, which show that some, but not all, of the nuclei of dwarf elliptical galaxies could indeed have formed through coalescence of their globular clusters. Additionally they observed several dwarf elliptical galaxies and found out that within the inner few scale lengths, their sample appeared to be depleted of bright clusters. Oh and Lin [118] used numerical simulations to show that in dwarf galaxies with relatively weak external tidal perturbations, dynamical friction can lead to significant orbital decay of globular clusters and the formation of compact nuclei within a Hubble time-scale.

Oh et al. [119] gave two possible models for the observed spatial distribution of Fornax globulars. One possibility they proposed is that the dark matter consists of massive black holes which transfer energy to the globulars, preventing them from sinking to the centre of the galaxy. Another possibility they investigated was to postulate a strong tidal interaction between the Milky Way and Fornax which also could inject energy into their orbits and the central core of the dwarf spheroidals. This latter idea is probably ruled out due to the proper motion observations of Fornax [39] which suggest it is already at closest approach on an extended orbit which never takes it close to the Milky Way.

Here we investigate another possibility for the lack of a nucleus in Fornax, namely that the central dark matter distribution has a very shallow cusp or core which dramatically increases the dynamical friction sinking time-scale [70]. This would be inconsistent with dark haloes that form within the cold dark matter cosmology which have cusps steeper than $\gamma = -1$ ($\rho(r) \propto r^{-\gamma}$) on all mass scales from $10^{-6} M_{\odot} - 10^{15} M_{\odot}$ [37, 40].

Controversial evidence for cored mass distributions in dwarf spiral galaxies has been

²Original publication: MNRAS, 368, 1073 (2006) [64]

debated for over a decade [107]. The inner structure of spheroidal galaxies is harder to determine, however Kley et al. [82] claimed that the second peak in the stellar number density in the nearby Ursa Minor dwarf spheroidal, is incompatible with cusped cold dark matter haloes. With their observations they show that this substructure has a cold kinematical signature and that its radial velocity with respect to its host galaxy is very small. Such a cold configuration could only survive intact if the stars orbited within a cored mass distribution where the orbital frequencies are all identical (harmonic potential) and phase mixing does not occur.

The stellar kinematical data for Fornax suggest that it is dark matter dominated with a mass to light ratio of order 20 within its optical extent. Due to the uncertainty on the orbital anisotropy, the mass distribution can only be weakly constrained - the data is consistent with either cusped or cored density distributions [90]. However the normalisation (or mass within the central 1 kpc) is better constrained. In the inner ~ 1 kpc of a cored halo the mean density is approximately six times lower than in a cusped halo. Furthermore the velocity distribution function of the background particles is hotter than a cusped halo. These facts conspire to significantly increase the dynamical friction time-scale in a cored mass distribution.

We constructed cored and cuspy dark matter potentials and calculated orbital decay and sinking times using high resolution numerical simulations together with analytic calculations [21]. The haloes were consistent with the kinematical data for Fornax. We followed circular and eccentric orbits of single and multiple globular clusters. Although many dynamical friction studies have been carried out before [19, 72, 165], we are not aware of any studies within constant density cores at the resolution used in this study, although a recent study explored the effects of sinking objects on various cusp structures [105].

4.2.2 Numerical methods

We carried out a series of self consistent simulations to examine the orbital behaviour of massive particles moving within a dark matter or stellar background. All the runs were evolved with PKDGRAV (see section 1.3.5). For our simulations we used $\alpha\beta\gamma$ -models described by equation (2.1) with $\alpha = 0.5 - 1.5$, $\beta = 3.0$ and $\gamma = 0.5 - 1.5$, or cored haloes with $\alpha = 0.5 - 1.5$, $\beta = 3.0$ and $\gamma = 0.0$.

In the former case we have $\rho_0 = 0.0058 \text{ M}_\odot \text{ pc}^{-3}$ and $r_s = 2.4 \text{ kpc}$. This cuspy halo has a virial mass of $2.0 \times 10^9 \text{ M}_\odot$. The concentration parameter is $c = 15$ but our results would not change with a lower concentration, since in either case we are within the asymptotic cusp part of the density profile. We used the multi-mass technique: 10^5 particles for the innermost sphere with 100 pc radius, 10^5 particles for the shell between 100 and 500 pc and 10^5 particles for the rest of the halo. The softening lengths of the particles in these shells are 1, 10 and 100 pc respectively. The results were found not to be sensitive to these values. The particle masses are 58 M_\odot , 569 M_\odot and $3.2 \times 10^4 \text{ M}_\odot$. These models are stable in isolation but allow us to achieve very high resolution at the halo centre where we wish to follow the dynamical friction.

For a small cored halo we have $\rho_0 = 0.10 \text{ M}_\odot \text{ pc}^{-3}$ and $r_s = 0.91 \text{ kpc}$ (n.b. the radius

at which the slope of the density profile is shallower than -0.1 is approximately 200 pc which defines the constant density region in this model). This halo has a virial mass of $2.0 \times 10^9 M_\odot$ and the concentration parameter is $c = 40$. Again, we use a three shell model that has 10^5 particles for the innermost sphere with 300 pc radius, 10^5 particles for the shell between 0.3 and 1.1 kpc and 3×10^5 particles for the rest of the halo. The softening lengths of the particles in these shells are 3, 30 and 300 pc respectively. The particle masses are $89 M_\odot$, $1640 M_\odot$ and $7572 M_\odot$. For a big cored dark matter halo we have basically the same parameters as for the halo with the small core, except for the scale length $r_s = 2.2$ kpc (here the constant density region is approximately 1 kpc), the virial mass $M_{\text{vir}} = 3.0 \times 10^{10} M_\odot$ and the particle masses, which are in this case $106 M_\odot$, $3625 M_\odot$ and $1.2 \times 10^5 M_\odot$.

4.2.3 Results

Single globular clusters

From the Chandrasekhar dynamical friction formula [15, 21], we can derive an expression for the radial sinking velocity of the globular cluster with mass M_{GC} at radius r

$$\frac{dr}{dt} = -\frac{4\pi \ln \Lambda(r) \rho(r) G^2 M_{\text{GC}} r}{v_c^2(r) d[rv_c(r)]/dr} \left[\text{erf} \left(\frac{v_c(r)}{\sqrt{2}\sigma(r)} \right) - \frac{2v_c(r)}{\sqrt{2\pi}\sigma(r)} \exp \left(-\frac{v_c^2(r)}{2\sigma^2(r)} \right) \right] \quad (4.3)$$

where G is Newtons constant of gravity, $v_c(r)$ is the local circular velocity, $\sigma(r)$ is the local velocity dispersion, $\rho(r)$ is the local density and $\ln \Lambda(r) = b_{\text{max}} \sigma^2(r)/GM_{\text{GC}}$ is the Coulomb logarithm.

In figure 4.5, we plot the numerical fits from equation (4.3) for different haloes and initial radii for the orbital decay of a single globular cluster where b_{max} was used as a free fitting parameter. The globular clusters are modelled as single particles of mass $M_{\text{GC}} = 2 \times 10^5 M_\odot$ with a softening of 10 pc. We do not expect our conclusions to change if we used a particle model for each globular since they are stable against tidal disruption within Fornax. We start the globulars outside the core, mostly on circular orbits and let them orbit, expecting them to spiral in to the centre of their respective host haloes due to dynamical friction. For the cuspy halo the analytic calculation agrees very well with the numerical simulation. Haloes with a core give a poorer agreement. After an initial sinking rate that agrees well with the analytic expectation, the globulars sink faster as they approach twice the core radius, and then stop sinking at the core radius. The stalling results are apparent in both of the cored halo simulations (small core and big core). We note, however, that it is not trivially due to the fact that the globular is of comparable mass to that enclosed by its orbit; the radius at which $M(r) = M_{\text{GC}}$ is approximately three times smaller than the core radius (see figure 4.7). We conclude that the presence of a central density core leads to a stopping of the infall of the clusters at approximately the core radius.

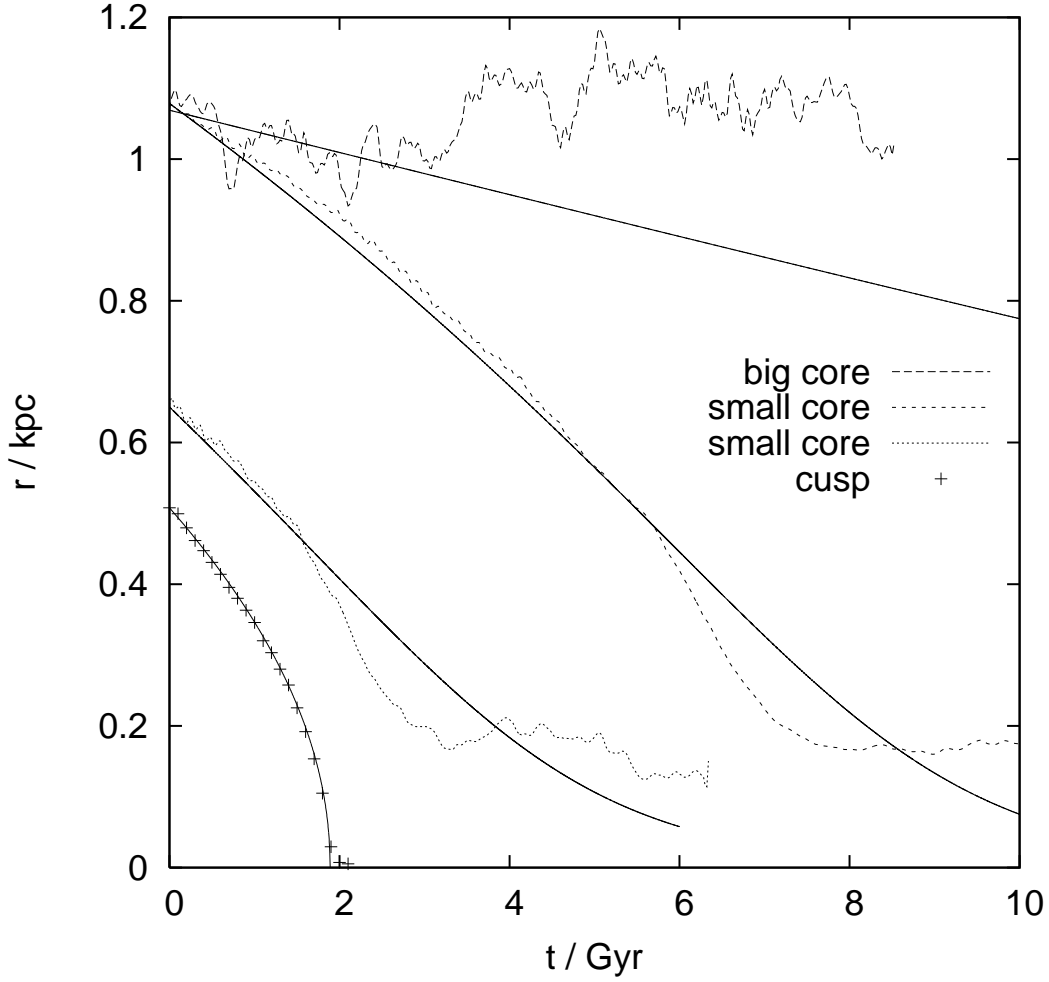


Figure 4.5: Radial distance of a single globular cluster from the centre of its host halo as a function of time. We start the calculations with the globular at different initial radii for clarity. Solid curves are the numerical fits, dashed curves are from the N-body simulations.

Multiple globular clusters

We re-ran these simulations using five globulars to study the effect of having multiple sinking objects. Perhaps interactions between the globulars themselves may prevent them from sinking to the central cusp and merging. We distribute the globulars randomly, what position and plane of the orbit concerns, with distances to the centre between 0.2 and 1.2 kpc. The clusters are again placed on circular orbits around the centre of their host halo.

Interestingly, the clusters do not prevent one another from falling to the centre, but instead create an interesting prediction. Figure 4.6 shows the infall as a function of time for the five globulars in the cuspy dark matter halo. Notice that all of the clusters fall to the centre within 5 Gyr. However, clusters which start out at very similar radii arrive approximately 1 Gyr apart. At any given time, even for very similar initial conditions, the clusters occupy a range of radii.

By contrast, for the case with a central dark matter core (see figure 4.7), although the globulars still arrive at different times due to interactions, they stall at the core radius; they do not sink to the centre even within 18 Gyr. Thus, if Fornax does have a central constant density core we should expect the clusters to stall at some minimum radius. No globular cluster could possibly get any closer to the centre of the halo than the core radius. The lower limit of the core size is constrained by the smallest observed projected cluster distances to be 0.24 kpc.

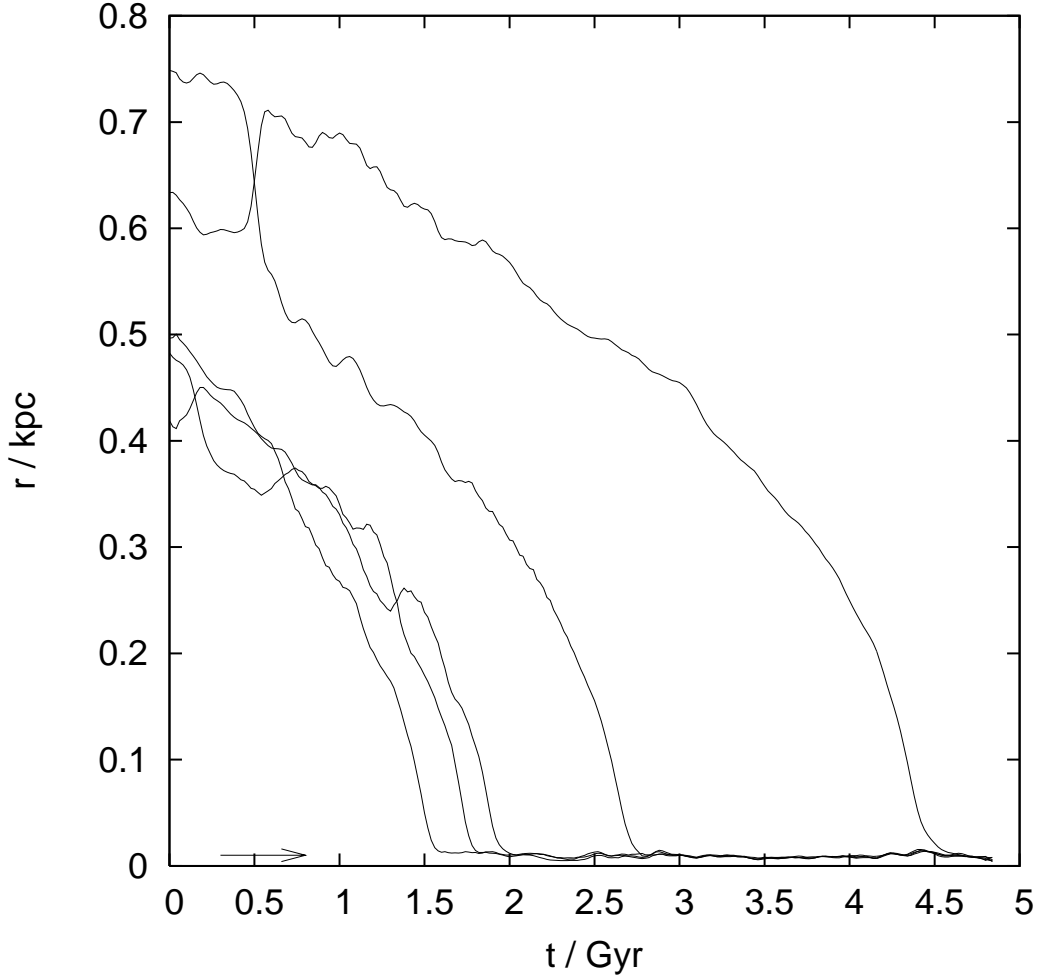


Figure 4.6: Radial distance of the five globular clusters from the centre of their host halo as function of time, as they orbit within a cuspy halo. The arrow indicates the radius at which $M_{GC} = M(r)$.

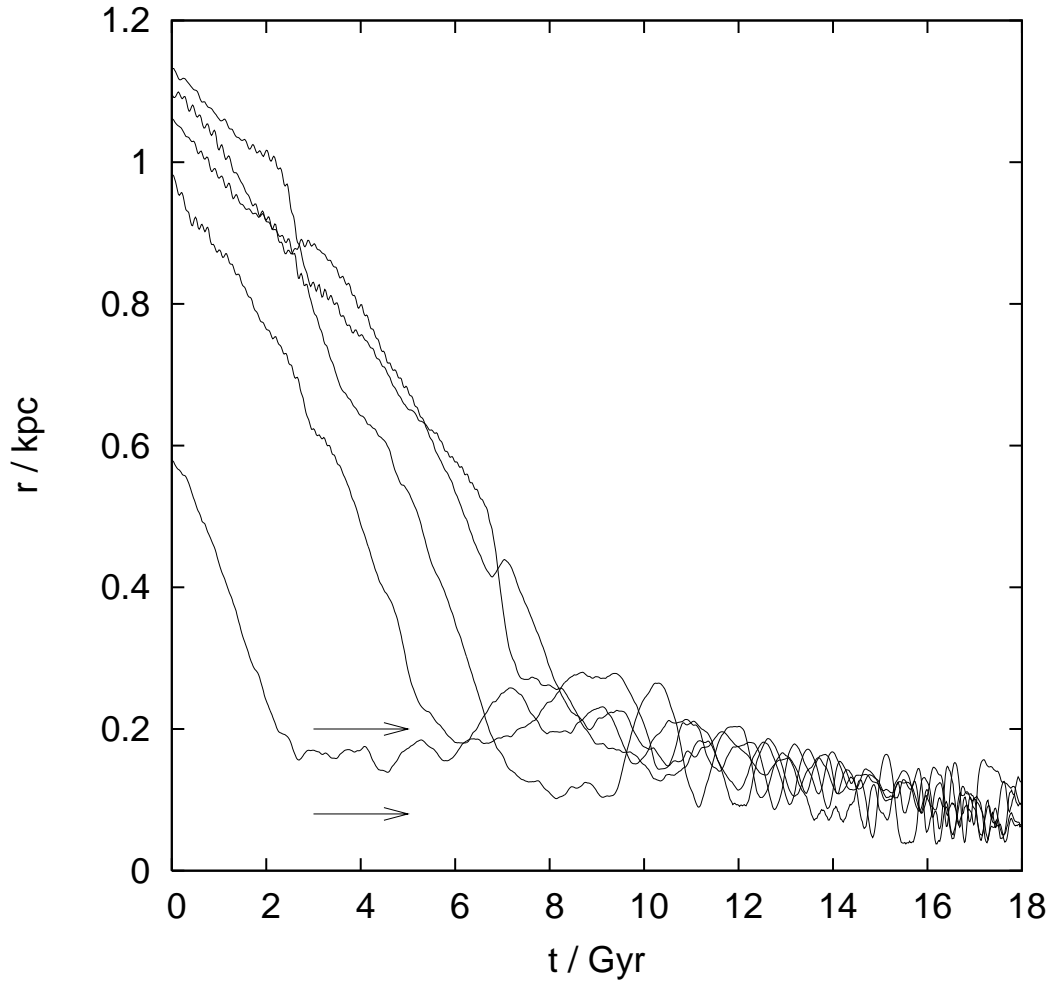


Figure 4.7: Radial distance of the five globular clusters from the centre of their host halo as function of time, as they orbit within a cored halo. The upper arrow indicates the size of the core and the lower arrow indicates the radius at which $M_{\text{GC}} = M(r)$.

Chapter 5

Summary and perspective

Summary

Resolving the fast dynamics in the centres of galaxies requires reconsidering the time-stepping method that is used to integrate the equations of motion. The standard time-stepping criterion used by most of the numerical codes so far is based on the acceleration of a particle. Unfortunately, with this method, one is only able to resolve regions of dark matter haloes down to approximately one per cent of the virial radius. Below that scale, the standard criterion fails completely to follow the dynamics of the simulations with the standard parameters normally used. It even gives an incorrect, in fact unphysical selection of time-steps in regions where the local density profile is flat, e.g. time-steps stay constant or even increase for particles closer to the centre due to the functional form of the acceleration with radius. This can only be adjusted by choosing a small prefactor η_s but as a consequence, the simulations become very slow.

The new time-step criterion determines the true dynamical time of each particle and sets this as the time-step. In the case of hard gravitational scattering events, an eccentricity correction for the integration method is used in order to follow the orbits precisely. With this method, we are able to resolve the dynamics at the centres of dense self-gravitating systems. By choosing an appropriate softening length for the particles, we can even resolve high eccentricity orbits during gravitational scattering events allowing the method to handle collisionless as well as collisional dynamics simultaneously.

In addition to correctly treating the physics the new method results in a substantial speed-up compared to traditional approaches since the dynamical time-step criterion is much more adaptive with radius, preventing particles from being integrated on overly conservative small time-steps. Also, the method does not directly depend on non-physical parameters like the softening length.

In order to resolve parsec scales in dark matter haloes, one would need billions of particles for a single halo model, a requirement that is still prohibitive with existing computational resources. The development of a multi-mass technique for generating high resolution dark matter haloes allows to resolve the scales where the dynamics of, e.g., a super-massive black hole binary becomes dominant and interacts significantly with its surroundings. Such studies were so far only possible for restricted cases and low resolution.

The multi-mass technique was already used in several applications that needed high

spatial resolution. In a test case for the multi-mass technique, we confirm earlier findings and predictions that core-core mergers lead to a cored merger remnant while cusp-cusp mergers lead to a cuspy merger remnant with high resolution multi-mass N-body simulations. In cusp-core merges, the merger remnant has a final profile corresponding to the steepest progenitor. In a cosmological structure formation simulation, the multi-mass technique was used to resolve the dark matter halo of a galaxy cluster down to one per mill of the virial radius which corresponds to an effective resolution of one billion particles. We found that the central profile still follows a power law with slope of approximately $\gamma = -1.2$, where $\rho(r) \propto r^{-\gamma}$. A further application tested a model that can explain the presence of the five globular clusters at approximately 1 kpc distance from the centre of the Fornax dwarf spheroidal galaxy.

Perspective

These new techniques enable the exploration of an unknown area of N-body simulations. Therefore, the main goals for the future are to apply these techniques in the primary application it was designed for: in mergers of galaxies with super-massive black holes and study the dynamical effects involved in this process.

Once the black hole binary is formed through the merger of the galaxies it may also have an influence on the density profile of the surrounding dark matter halo. The black hole binary may transfer energy to the surrounding particles in the high-density central region through the slingshot-effect, which leads to a shallower central density profile of the dark matter. The question of the central density is very important, since one of the observational consequences of this is an observable flux of gamma-rays from the inner few parsecs of the halo due to self-annihilation of dark matter [63]. The flux is very sensitive to the central dark matter density. Establishing the stability of the central dark matter cusp to dynamical perturbations is therefore of paramount importance to planning and interpreting the data that will be soon provided by major facilities, such as the 17 m MAGIC¹ telescope, which are designed to measure such a signal. There were previous studies of this problem [101, 104], which were limited in resolution. We intend to address this issue by performing simulations in a self-consistent way, with the needed resolution that includes the large-scale dynamics from the dark matter halo and the small-scale collisional physics in the centre of the galaxies.

Yu and Tremaine [172] postulated that a possible mechanism for the origin of hyper-velocity stars (i.e. stars moving with incredible high velocity such that they possibly will escape the galaxy) is the gravitational scattering by massive binaries (black hole or stars or a combination of the two) in the centre of galaxies. Studying the characteristics of these hyper-velocity stars is important to predict the expected parameter space for future observational programs that would allow detecting these fast stars systematically. We plan to study this in a self-consistent way and examine the dependence of the orbits of the ejected stars on the triaxiality of the halo.

¹magic.mppmu.mpg.de

In the hierarchical paradigm, successive mergers between spheroids that host black holes may lead to the accelerated formation of super-massive black holes at the centres of galaxies [75, 94]. This process has interesting and potentially observable consequences, including a large population of black holes orbiting within and through the galaxy that ejected them through 3-body encounters. Using high resolution N-body simulations of structure formation in a cold dark matter universe, we can test two distinct scenarios for the formation of super-massive black holes: (i) A final central black hole may form due to the hierarchical merger of thousands of small dark matter haloes. Through some process, each of the progenitor haloes may contain a small black hole. As the mergers take place the black holes spiral inwards in the cuspy dark matter potentials, eventually merging together through energy loss from gravitational radiation. (ii) Black holes form in a population of globular clusters that form within the rare dark matter mini-haloes at a redshift $z = 10 - 20$. These undergo a rapid merging process to create a single central super-massive black hole. In such a calculation it is important to be able to closely follow the dynamical interactions between the black holes, which is why it is important to employ the new time-stepping algorithm and study these interactions within a self-consistently modelled cosmological context. Our aim is to investigate whether it is possible to form a single central super-massive black hole, and to study the spatial and kinematical distribution of ejected black holes.

A possible drawback might be the enormous amount of computer run time that is needed for such simulations. Possible solutions like introducing hierarchies of trees where some parts of the simulations are frozen while only particles in very-active regions of the simulation are evolved or loosening the strict geometrical definition of the dynamical time are already under development.

But for future high resolution N-body simulations, the only efficient time-stepping scheme has to be based on the true dynamical time since it shows the optimum scaling with the number of particles used and always gives a physically correct time-step.

Appendix

Appendix A

Hamiltonian formalism

For a physical system that is described by the state $\mathbf{z} = (\mathbf{q}, \mathbf{p})$, where \mathbf{q} is the coordinate and \mathbf{p} the conjugate momentum vector, and this system is evolved under a Hamiltonian H , we can write the formal time evolution (Hamilton equations) as [15, 132, 171]

$$\frac{d\mathbf{z}}{dt} = \dot{\mathbf{z}} = \{\mathbf{z}, H\} \quad (\text{A.1})$$

where $\{, \}$ denote the Poisson brackets defined by

$$\{g, h\} \equiv \sum_i^f \left(\frac{\partial g}{\partial q_i} \frac{\partial h}{\partial p_i} - \frac{\partial g}{\partial p_i} \frac{\partial h}{\partial q_i} \right) . \quad (\text{A.2})$$

We can define the operator \hat{H} by

$$\hat{H}\mathbf{z} \equiv \{\mathbf{z}, H\} \quad (\text{A.3})$$

and write down a formal solution to the time evolution

$$\mathbf{z}(t) = e^{t\hat{H}} \mathbf{z}_0 . \quad (\text{A.4})$$

In computer simulations, the system is evolved by using a specific scheme in order to update positions and velocities. In PKDGRAV, the following leapfrog scheme is used: during a time-step ΔT , first the velocities are updated (kick mode) with a time step of $\Delta T/2$ then the new positions are calculated (drift mode) using the new velocities with a time-step of ΔT and finally the velocities are updated to the final values at ΔT with again a half-step of $\Delta T/2$ but with the acceleration calculated from the new positions. This scheme can be written as

$$\mathbf{v}(t + \Delta T/2) = \mathbf{v}(t) + \Delta T/2 \mathbf{a}(t) \quad (\text{A.5})$$

$$\mathbf{x}(t + \Delta T) = \mathbf{x}(t) + \Delta T \mathbf{v}(t + \Delta T/2) \quad (\text{A.6})$$

$$\mathbf{v}(t + \Delta T) = \mathbf{v}(t + \Delta T/2) + \Delta T/2 \mathbf{a}(t + \Delta T) \quad (\text{A.7})$$

and is therefore called the kick-drift-kick mode. We can write it in the operator formalism as

$$\mathbf{z}(\Delta T) = e^{\frac{\Delta T}{2} \hat{H}_K} e^{\Delta T \hat{H}_D} e^{\frac{\Delta T}{2} \hat{H}_K} \mathbf{z}_0 \quad (\text{A.8})$$

Appendix A Hamiltonian formalism

where we have split the true Hamiltonian into a drift and a kick part

$$\hat{H} = \hat{H}_D + \hat{H}_K . \quad (\text{A.9})$$

By using the Baker-Campbell-Hausdorff series, where we can calculate the higher order terms by an elegant method developed by Reinsch [130], we can write the approximate operator \hat{H}_A under which the system is evolved

$$\mathbf{z}(\Delta T) = e^{\frac{\Delta T}{2} \hat{H}_K} e^{\Delta T \hat{H}_D} e^{\frac{\Delta T}{2} \hat{H}_K} \mathbf{z}_0 = e^{\Delta T \hat{H}_A} \mathbf{z}_0 \quad (\text{A.10})$$

by

$$\hat{H}_A = \hat{H}_0 + \Delta T^2 \hat{H}_2 + \Delta T^4 \hat{H}_4 + O(\Delta T^6) \quad (\text{A.11})$$

where

$$\hat{H}_0 = \hat{H}_D + \hat{H}_K = \hat{H} \quad (\text{A.12})$$

$$\hat{H}_2 = \frac{1}{12} \left[[\hat{H}_K, \hat{H}_D], \hat{H}_D \right] - \frac{1}{24} \left[[\hat{H}_D, \hat{H}_K], \hat{H}_K \right] \quad (\text{A.13})$$

$$\begin{aligned} \hat{H}_4 = & \frac{7}{5760} \left[\left[\left[[\hat{H}_D, \hat{H}_K], \hat{H}_K \right], \hat{H}_K \right], \hat{H}_K \right] \\ & \frac{7}{1440} \left[\left[\left[[\hat{H}_D, \hat{H}_K], \hat{H}_D \right], \hat{H}_K \right], \hat{H}_K \right] \\ & - \frac{1}{360} \left[\left[[\hat{H}_D, \hat{H}_K], \hat{H}_K \right], [\hat{H}_D, \hat{H}_K] \right] \\ & - \frac{1}{180} \left[\left[\left[[\hat{H}_K, \hat{H}_D], \hat{H}_K \right], \hat{H}_D \right], \hat{H}_D \right] \\ & - \frac{1}{360} \left[\left[[\hat{H}_K, \hat{H}_D], \hat{H}_D \right], [\hat{H}_K, \hat{H}_D] \right] \\ & - \frac{1}{720} \left[\left[\left[[\hat{H}_K, \hat{H}_D], \hat{H}_D \right], \hat{H}_D \right], \hat{H}_D \right] . \end{aligned} \quad (\text{A.14})$$

Here, $[\cdot, \cdot]$ denote the commutator brackets defined by

$$[A, B] = AB - BA \quad (\text{A.15})$$

for non-commutative operators A and B . By using the definitions of the operators and the Jacobi identity for Poisson brackets

$$\{\{A, B\}, C\} + \{\{B, C\}, A\} + \{\{C, A\}, B\} = 0 , \quad (\text{A.16})$$

we can calculate the approximate Hamiltonian

$$H_A = H_0 + \Delta T^2 H_2 + \Delta T^4 H_4 + O(\Delta T^6) \quad (\text{A.17})$$

where

$$H_0 = H_D + H_K = H \quad (\text{A.18})$$

$$H_2 = \frac{1}{12} \{ \{ H_K, H_D \}, H_D \} - \frac{1}{24} \{ \{ H_D, H_K \}, H_K \} \quad (\text{A.19})$$

$$\begin{aligned} H_4 = & \frac{7}{5760} \{ \{ \{ \{ H_D, H_K \}, H_K \}, H_K \}, H_K \} \\ & \frac{7}{1440} \{ \{ \{ \{ H_D, H_K \}, H_D \}, H_K \}, H_K \} \\ & - \frac{1}{360} \{ \{ \{ H_D, H_K \}, H_K \}, \{ H_D, H_K \} \} \\ & - \frac{1}{180} \{ \{ \{ \{ H_K, H_D \}, H_K \}, H_D \}, H_D \} \\ & - \frac{1}{360} \{ \{ \{ \{ H_K, H_D \}, H_D \}, \{ H_K, H_D \} \} \\ & - \frac{1}{720} \{ \{ \{ \{ H_K, H_D \}, H_D \}, H_D \}, H_D \} . \end{aligned} \quad (\text{A.20})$$

Note that the replacement of the commutator brackets by the Poisson brackets is not trivial. The term H_4 is not used in our method. However, since H_4 is not explicitly given in the recent literature we present it here for completeness.

Appendix B

Further projects

This chapter is a short summary of further projects in which the author of this thesis was involved as a co-author. These projects are not related to the main developments of the thesis.

B.1 A universal velocity distribution of relaxed collisionless structures¹

B.1.1 Introduction

The last few years have shown remarkable progress in the understanding of pure dark matter structures. This has been provided initially by numerical simulations which have observed general trends in the behaviour of the radial density profile of equilibrated dark matter structures from cosmological simulations, which roughly follow an NFW profile [110, 112, 116, see also equation (2.1)] with central density profile slope $\gamma = 1.0$. General trends in the radial dependence of the velocity anisotropy has also been suggested [20, 24]. More recently have more complex relations been identified, which even hold for systems which do not follow the most simple radial behaviour in density. These relations are first that the phase-space density, ρ/σ^3 , is a power-law in radius [150], and second that there is a linear relationship between the density slope and the anisotropy [67].

All of these are integrated quantities, and still very little is known about the underlying velocity distribution function of real collisionless systems. We initiated such a study by performing a set of different simulations of purely collisionless systems.

B.1.2 Numerical methods and results

The first controlled simulation were head-on collision between two equal spherical NFW structures. We created three different initial conditions. The first model had an isotropic velocity structure. For the other two models we kept the kinetic energy of a particle from the isotropic model fix but rotated the velocity vector so that it pointed to the centre (radial initial conditions) or were tangential (tangential initial conditions). For

¹Original publication: JCAP, 1, 14 (2006) [69]

the construction of the initial structures, we used the method as described in Kazantzidis et al. [80]. We created an initial NFW structure containing one million particles. The parameters were chosen corresponding to a total mass of $10^{12} M_{\odot}$ (concentration of $c = 10$), and half of the particles were within 160 kpc.

We placed two such structures with equal velocity structure very far apart with 2000 kpc between the centres, which is well beyond the virial radius. Using a softening of 0.2 kpc, we let these two structures collide head-on with an initial relative velocity of 100 km s^{-1} towards each. After several crossings the resulting blob relaxed into a prolate structure. We run all simulations until there was no further time variation in the radial dependence of the anisotropy and density. We checked that there is no (local) rotation. We run this simulation for 150 Gyr, which meant that a very large part of the resulting structure is fully equilibrated.

We now took the resulting structure (now containing two million particles, in a prolate shape) and collided two copies together, again with their centres separated by 2000 kpc, and with initial relative velocity of 100 km s^{-1} . We used softening of 1 kpc. The resulting structure is even more prolate when observed in density contours, and we evolved this for another 150 Gyr. All simulations were carried out using PKDGRAV (see section 1.3.5).

In order to analyse the resulting structure we divided it into bins in potential energy, linearly distributed from the softening length to beyond the region which is fully equilibrated. For the analysis and figures presented here, we always only included a region outside three times the softening. We centred the structure on the centre of potential (using potential as weight-function instead of mass as done for centre of mass). Most other analyses are centring on either the centre of mass, or on the most bound particle, but the difference is very small. We calculated the local density for each particle from its nearest 32 neighbours, and we averaged the density for all the particles in the potential bin. Similarly, each particle had a radius from the centre of potential, and we can averaged this over all the particles in the potential bin. The resulting density profile, $\langle \rho \rangle$ as a function of $\langle r \rangle$, was very similar to an NFW profile.

For each bin we can also defined the radial derivative of the density (the density slope)

$$\alpha \equiv \frac{d \ln \langle \rho \rangle}{d \ln \langle r \rangle} , \quad (\text{B.1})$$

and we can extracted the radial velocity distribution function for each potential bin. We present the radial velocity distribution function for bins with $\alpha \approx -2.6, -2$ and -1.1 in figure B.1. The red (open) stars are from a bin in the region with shallow density slope ($\alpha \approx -1.1$), the green (open) squares are from an intermediate bin (slope close to -2), and the blue (filled) triangles are from a bin in the outer region (slope close to -2.6). There seems to be a clear trend, namely that the velocity distribution function from bins in the inner region have longer high energy tails than velocity distribution functions from bins in the outer region. The high energy tail of the radial velocity distribution function

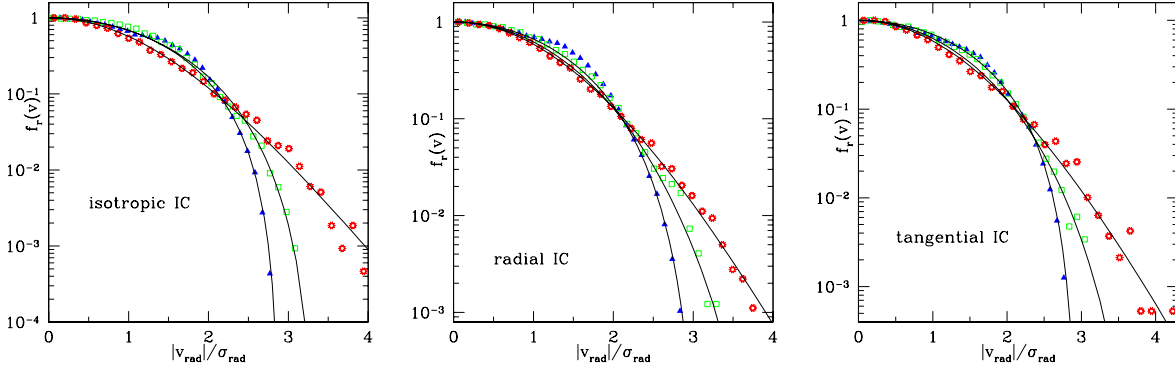


Figure B.1: The radial velocity distribution function for three potential bins in the simulation of repeated head-on collisions between NFW structures with very different initial conditions: isotropic (left), radial (middle) and tangential (right) velocity distributions. The potential bins are chosen near density slope of $\alpha \approx -1.1$ (open red stars), $\alpha \approx -2$ (open green squares) and $\alpha \approx -2.6$ (filled blue triangles). The thin (solid) lines are of the shape given by equation (B.2), using q 's of 0.75, 0.81 and 1.08 (isotropic); $q = 0.79, 0.91$ and 1.05 (radial) and $q = 0.75, 0.89$ and 1.045 (tangential).

is well approximated by the shape given by

$$f_r(v) = \left(1 - (1 - q) \left(\frac{v}{\kappa_{\text{rad}} \sigma_{\text{rad}}} \right)^2 \right)^{\frac{q}{1-q}}, \quad (\text{B.2})$$

where q and κ_{rad} are free parameters. This is of the Tsallis form [154] and depends on the entropic index q . For $q = 1$, equation B.2 reduces to the Gaussian shape $f(v) \propto \exp(-(v/v_0)^2)$. This functional form is chosen partly for simplicity (and because it includes the classical exponential) and partly because some simple structures are known to have velocity distribution functions of exactly this form [68, 124]. In particular do we see that the resulting velocity distribution functions do not have the shape of Gaussians with a cut-off at the escape velocity. It is clear from figure B.1 above, that the simple shape of equation (B.2) provides a reasonable fit to the tails of the radial velocity distribution functions.

The two-dimensional generalisation of the form (B.2) is given by

$$f_t(v) = v \left(1 - (1 - q) \left(\frac{v}{\kappa_{\text{tan}} \sigma_{\text{tan}}} \right)^2 \right)^{\frac{q}{1-q}}. \quad (\text{B.3})$$

The tangential velocity distributions $f_t(v)$ can be fitted by two such shapes: one in the small velocity region, and another in the high velocity region. It was argued in Hansen and Moore [67] that the tangential velocity distribution functions could have the shape of equation (B.3) with $q = 5/3$, and the small velocity region is very well fit with exactly this shape for all the bins in potential.

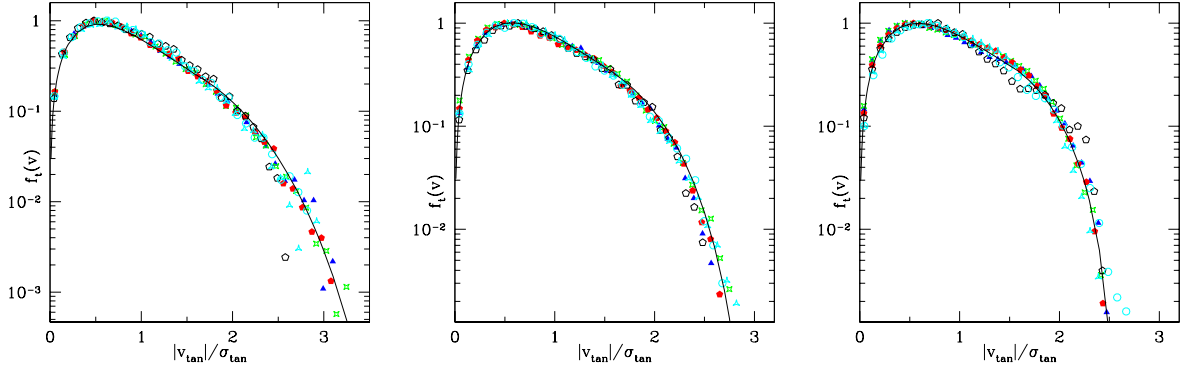


Figure B.2: The tangential velocity distribution functions from all the simulations described. The black (solid) line has two parts (separated at $v_{\text{tan}} = 1.6 \sigma_{\text{tan}}$), each fitted with the shape given in equation (B.3), where the low energy part uses $q = 5/3$, and the outer region (high energy part) has a free q . Left: using a potential bin near the density slope of $\alpha = -1.1$, and the black (solid) line uses $q = 0.9$ in the high energy part. Middle: $\alpha = -2$, $q = 0.86$. Right: $\alpha = -2.6$, $q = 0.76$.

We pick the position $v_{\text{tan}} = 1.6 \sigma_{\text{tan}}$ as the transition velocity for all figures, and fit the high energy region with the shape of equation (B.3), but with q as a free parameter. The combined fit is shown as black (solid) lines in figure B.2.

But not only the velocity distribution functions from the resulting remnants of these controlled head-on collisions can be described by the functional form given by (B.2) respectively (B.3). We also examined haloes from cosmological structure formation runs or remnants of radial infall simulations and their velocity distribution functions have the same shape as already described.

Hence, we have identified a universality of the velocity distribution function of equilibrated structures of collisionless, self-gravitating systems through a set of numerical experiments. The radial and tangential velocity distribution functions are universal in the sense that they depend only on the dispersion (radial or tangential) and the local slope of the density. There is a general trend, namely that a steeper density slope implies small q . The actual shape of the velocity distribution functions is not understood yet. These numerical results may hopefully inspire further theoretical understanding of the velocity distribution function of collisionless particles.

B.2 Globular clusters, satellite galaxies and stellar haloes from early dark matter peaks²

B.2.1 Introduction

The Milky Way is a typical bright spiral galaxy. Its disk of stars and gas is surrounded by an extended halo of old stars, globular star clusters and a few dark matter dominated old satellite galaxies. For the past 30 years two competing scenarios for the origin of galaxies and their stellar components have driven much observational and theoretical research. Eggen et al. [43] proposed a monolithic collapse of the Galaxy whilst Searle and Zinn [136] advocated accretion of numerous proto-galactic fragments.

Enormous progress has been made in understanding the structure and origin of the Milky Way, as well as defining a standard cosmological model for structure formation that provides us with a framework within which to understand our origins [51, 122]. Hierarchical growth of galaxies is a key expectation within a universe whose mass is dominated by a dark and nearly cold particle, yet evidence for an evolving hierarchy of merging events can be hard to find, since much of this activity took place over ten billion years ago. The origin of the luminous Galaxy depends on the complex assembly of its approximately $10^{12} M_{\odot}$ dark matter halo that extends beyond 200 kpc, and on how stars form within the first dark matter structures massive enough to cool gas to high densities [166].

The Galactic halo contains about 100 old metal poor globular clusters (i.e. Forbes et al. [50]) each containing up to 10^6 stars. Their spatial distribution falls off as $r^{-3.5}$ at large radii and half the globulars lie within 5 kpc from the centre of the Galaxy [147]. There is no evidence for dark matter within the globular clusters today [108, 123]. The old stellar halo population has a similar spatial distribution and a total luminosity of $10^8 - 10^9 L_{\odot}$ ³ [76, 95]. The stellar populations, ages and metallicities of these components are very similar [51].

Also orbiting the Galaxy are several tiny spheroidal satellite galaxies, each containing an old population of stars, some showing evidence for more recent star-formation indicating that they can hold on to gas for a Hubble time [55, 65]. Half of the dwarf satellites lie within 85 kpc, have luminosities in the range $10^6 - 10^8 L_{\odot}$ and are surrounded by dark matter haloes at least 50-200 times as massive as their baryonic components [98]. Cold dark matter models have had a notoriously hard time at reconciling the observed low number of satellites with the predicted steep mass function of dark matter haloes [79, 83, 111].

We wish to explore the hypothesis that cold dark matter dominates structure formation, the haloes of galaxies and clusters are assembled via the hierarchical merging and accretion of smaller progenitors [88]. This process violently causes structures to come to a new equilibrium by redistributing energy among the collisionless mass components. Early stars formed in these progenitors behave as a collisionless system just like the dark

²Original publication: MNRAS, 368, 563 (2006) [115]

³ L_{\odot} stands for the luminosity (radiated energy per unit time) of the Sun. $L_{\odot} = 3.826 \times 10^{26} \text{ J s}^{-1}$.

matter particles in their host haloes, and they undergo the same dynamical processes during subsequent mergers and the buildup of larger systems like massive galaxies or clusters.

In a recent study, Diemand et al. [36] used cosmological N-body simulations to explore the distribution and kinematics in present-day cold dark matter haloes of dark matter particles that originally belonged to rare peaks in the matter density field. These properties are particularly relevant for the baryonic tracers of early cold dark matter structures, for example the old stellar halo which may have originated from the early disruption of numerous dwarf proto-galaxies [17], the old halo globular clusters and also giant ellipticals [56].

Since rare, early haloes are strongly biased towards overdense regions [137], i.e. towards the centres of larger scale fluctuations that have not collapsed yet, we might expect that the contribution at $z = 0$ from the earliest branches of the merger tree is much more centrally concentrated than the overall halo. Indeed, a non-linear peaks biasing has been discussed by previous authors [109, 110, 167]. Diemand et al. [36] showed that the present-day distribution and kinematics of material depends primarily on the rareness of the peaks of the primordial density fluctuation field that the selected matter originally belonged to, i.e. when selecting rare density peaks above $\nu\sigma(M, z)$ (where $\sigma(M, z)$ is the linear theory rms density fluctuations smoothed with a top-hat filter of mass M at redshift z), their properties today depend on ν and not on the specific values of selection redshift z and minimal mass M .

B.2.2 The first stellar systems

We propose that ordinary Population II stars and globular clusters first appeared in significant numbers at redshift $z > 12$, as the gas within protogalactic haloes with virial temperatures above 10^4 K (corresponding to masses comparable to those of present-day dwarf spheroidals) cooled rapidly due to atomic processes and fragmented.

It is this second generation of subgalactic stellar systems, aided perhaps by an earlier generation of metal-free (Population III) stars and by their remnant black holes, which generated enough ultraviolet radiation to reheat and reionize most of the hydrogen in the Universe by a redshift $z = 12$, thus preventing further accretion of gas into the shallow potential wells that collapsed later. The impact of a high redshift ultraviolet radiation background on structure formation has been invoked by several authors [7, 10, 17, 66, 109, 155] to explain the flattening of the faint end of the luminosity function and the missing satellites problem within our Local Group. Here we use high resolution numerical simulations that follow the full non-linear hierarchical growth of galaxy mass haloes to explore the consequences and predictions of this scenario.

Dark matter structures will collapse at different times, depending on their mass, but also on the underlying larger scale fluctuations. At any epoch, the distribution of masses of collapsed haloes is a steep power law towards low masses with $n(m) \propto m^{-2}$. To make quantitative predictions we calculate the non-linear evolution of the matter distribution within a large region of a Λ CDM universe. The entire well resolved region is about 10 comoving Mpc across and contains 61 million dark matter particles of mass $5.85 \times 10^5 M_\odot$.

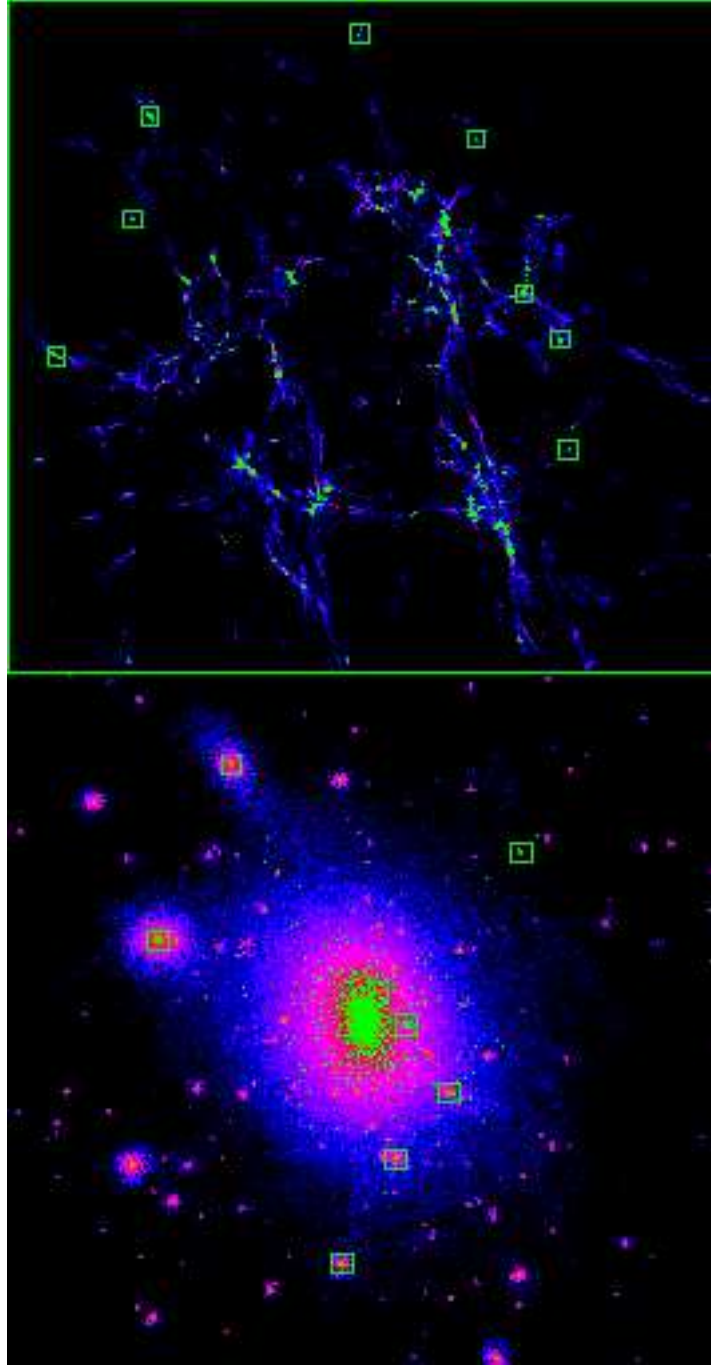


Figure B.3: The high redshift and present day mass distribution in a region that forms a single galaxy in a hierarchical cold dark matter universe.

and force resolution of 0.27 kpc. This region is embedded within a larger 90 Mpc cube that is simulated at lower resolution such that the large scale tidal field is represented. Figure B.3 shows the high-redshift and present-day mass distribution of a single galaxy mass halo taken from this large volume. The upper panel shows the density distribution at a redshift $z = 12$ from a region that will form a single galaxy at $z = 0$ (lower panel). The rare peaks collapsing at high redshift that have had sufficient time to cool gas and form stars, can be identified, followed and traced to the present day. Because small fluctuations are embedded within a globally larger perturbation, the small rarer peaks that collapse first are closer to the centre of the final potential and they preserve their locality in the present day galaxy. The strong correlation between initial and final position results in a system where the oldest and rarest peaks are spatially more concentrated than less rare peaks. The present day spatial clustering of the material that was in collapsed structures at a higher redshift only depends on the rarity of these peaks [36].

Our simulation contains several well resolved galactic mass haloes which we use to trace the evolution of progenitor haloes that collapse at different epochs. The first metal free Population III stars form within minihaloes already collapsed by $z > 25$, where gas can cool via roto-vibrational levels of H_2 and contract. Their evolution is rapid and local metal enrichment occurs from stellar evolution. Metal-poor Population II stars form in large numbers in haloes above $M_H \approx 10^8 [(1+z)/10]^{-3/2} M_\odot$ (virial temperature 10^4 K), where gas can cool efficiently and fragment via excitation of hydrogen $Ly\alpha$. At $z > 12$, these correspond to $> 2.5\sigma$ peaks of the initial Gaussian overdensity field: most of this material ends up within the inner few kpc of the Galaxy. Within the approximately 1 Mpc turn-around region, a few hundred such protogalaxies are assembling their stellar systems [85]. Typically 95% of these first structures merge together within a time-scale of a few Gyr, creating the inner Galactic dark matter halo and its associated old stellar population.

With an efficiency of turning baryons into stars and globular clusters of the order $f_* = 10\%$ we successfully reproduce the total luminosity of the old halo population and the old dwarf spheroidal satellites. The fraction of baryons in dark matter haloes above the atomic cooling mass at redshift $z = 12$ exceeds $f_c = 1\%$. A normal stellar population with a Salpeter-type initial mass function emits about 4000 hydrogen-ionizing photons per stellar baryon. A star formation efficiency of 10% therefore implies the emission of $4000 \times f_* \times f_c \sim$ a few Lyman-continuum photons per baryon in the Universe. This may be enough to photoionize and drive to a higher adiabat vast portions of the intergalactic medium, thereby quenching gas accretion and star formation in nearby low-mass haloes.

B.2.3 Connection to globular clusters and halo stars

The globular clusters that were once within the merging proto-galaxies are so dense that they survive intact and will orbit freely within the Galaxy. The surviving proto-galaxies may be the precursors of the old satellite galaxies, some of which host old globular clusters such as Fornax, whose morphology and stellar populations are determined by ongoing gravitational and hydrodynamical interactions with the Milky Way [100].

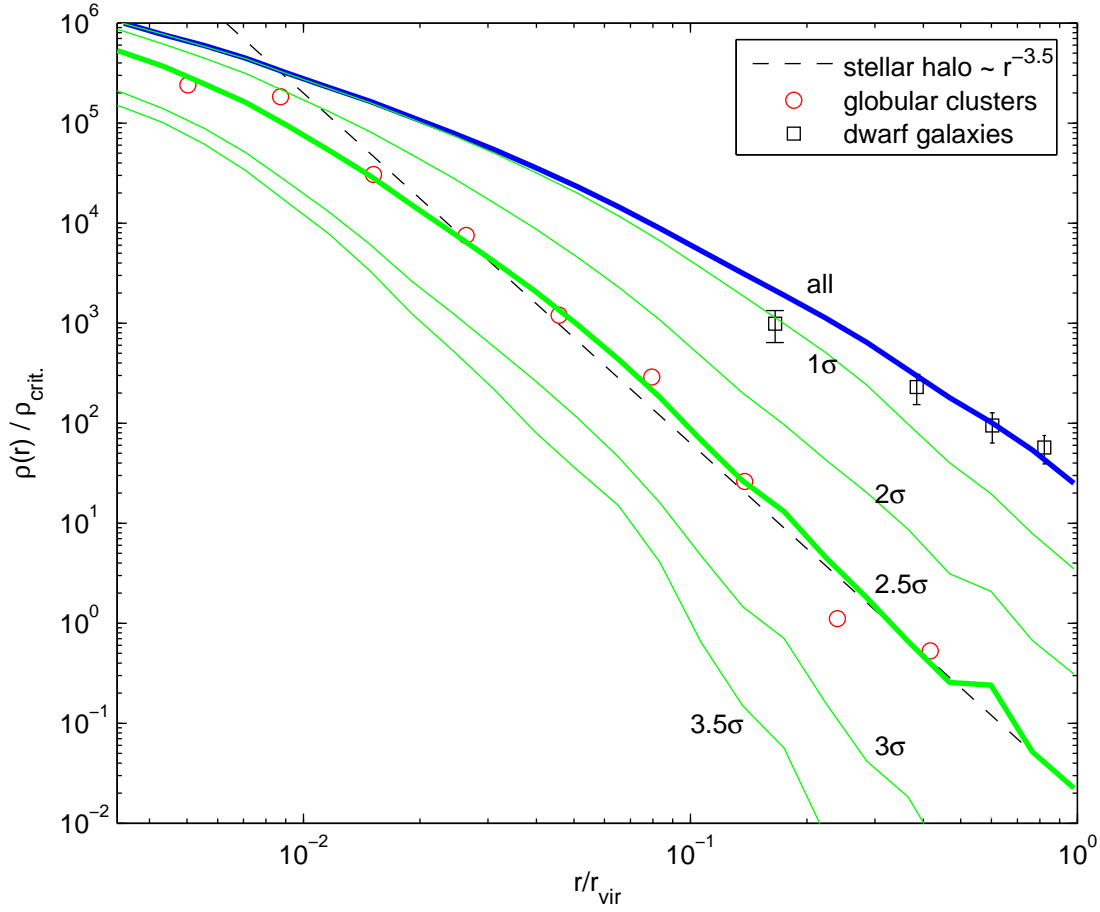


Figure B.4: The radial distribution of old stellar systems compared with rare peaks within a $z = 0$ Λ CDM galaxy. The thick blue curve is the total mass distribution today. The labeled green curves show the present day distribution of material that collapsed into $1, 2, 2.5, 3$ and 3.5σ peaks at a redshift $z = 12$. The circles show the observed spatial distribution of the Milky Way’s old metal poor globular cluster system. The dashed line indicates a power law $\rho(r) \propto r^{-3.5}$ which represents the old halo stellar population. The squares show the radial distribution of surviving 2.5σ peaks which are slightly more extended than the overall NFW-like mass distribution, in good agreement with the observed spatial distribution of the Milky Way’s satellites.

Recent studies have attempted to address the origin of the spatial distribution of globular clusters [120, 121]. Most compelling for this model and one of the key results in this paper, is that we naturally reproduce the spatial clustering of each of these old components of the galaxy. The radial distribution of material that formed from $> 2.5\sigma$ peaks at $z > 12$ now falls off as $\rho(r) \propto r^{-3.5}$ within the Galactic halo - just as the observed old halo stars and metal poor globular clusters (see figure B.4). Cosmological hydrodynamical simulations are also beginning to attain the resolution to resolve the formation of the old stellar haloes of galaxies [3]. Because of the steep fall off with radius, we note that we do not expect to find any isolated globular clusters beyond the virial radius of a galaxy.

These first collapsing structures infall radially along filaments and end up significantly more flattened than the mean mass distribution. They also have colder velocity distributions and their orbits are isotropic in the inner halo and increasingly radially anisotropic in the outer part. Material from these rare peaks has $\beta_{\text{std}} = 1 - \frac{1}{2}(\sigma_{\text{tan}}^2/\sigma_{\text{rad}}^2) \approx 0.45$ at our position in the Milky Way, in remarkable agreement with the recently measured anisotropy and velocity dispersion of halo stars [9, 22, 151]. Diemand et al. [36] show that the radial distribution of rarer peaks is even more highly biased - thus the oldest population III stars and their remnant black holes are found mainly within the inner kpc of the Galaxy, falling off with radius steeper than r^{-4} .

The observational evidence for tidal stellar streams from globular clusters suggests that they are not embedded within extended dark matter structures today [108]. This does not preclude the possibility that the globular clusters formed deep within the central region of $10^8 M_{\odot}$ dark matter haloes which have since merged together. (Massive substructure within the inner $\sim 0.2 r_{\text{vir}}$ of galactic mass haloes is tidally disrupted [61].) This is what we expect within our model which would leave the observed globulars freely orbiting without any trace of the original dark matter component. However, it is possible that the most distance halo globulars may still reside within their original dark matter halo. If the globular cluster is located at the centre of the cold dark matter cusp, then observations of their stellar kinematics may reveal rising dispersion profiles. If the globular cluster is orbiting within a cold dark matter mini-halo then we would expect to see symmetric tidal streams orbiting within the potential of the cold dark matter substructure halo rather than being stripped by the Galaxy.

B.2.4 Connection to satellite galaxies and the missing satellites problem

The remaining $\sim 5\%$ of the proto-galaxies form sufficiently far away from the mayhem that they fall into the assembling galaxy late ($z \approx 1 - 2$, about one Gyr after the formation of the inner Galaxy at $z \approx 5$). This leaves time to enhance their α/Fe element ratios from Type II supernovae [127, 169, 170]. Recent studies including chemical modeling of this process support this scenario [49, 131].

The proto-galaxies highlighted with boxes in Figure B.3 are those few systems that survive until the present epoch - they all form on the outskirts of the collapsing region,

ending up tracing the total mass distribution as is also observed within the Milky Way's and M31's satellite systems. Each of our four high resolution galaxies contains about ten of these surviving proto-galaxies which have a radial distribution that is slightly shallower than that of the total mass distribution (see figure B.4) but more concentrated than the distribution of all surviving (or $z = 0$ mass selected) subhaloes. This is consistent with the spatial distribution of surviving satellites in the Milky Way and in other nearby galaxies in the 2dF [133, 158] and DEEP2 samples [23] and with galaxy groups like NGC5044 [46].

The total number of dark matter substructures in the Local Group is over an order of magnitude larger than the observations. Reionisation and photo-evaporation must play a crucial role in suppressing star formation in less rare peaks, thus keeping most of the low mass haloes that collapse later devoid of baryons. The surviving population of rare peaks had slightly higher masses just before accretion, tidal stripping inside the Galaxy halo then reduced their masses and they match the observations at $z = 0$.

Likewise to the radial distribution, the kinematics of the surviving visible satellite galaxies resembles closely the one of the dark matter while the same properties for all the surviving subhaloes differ. In the inner part our model satellite galaxies are hotter than the dark matter background, especially in the tangential component. This is consistent with the observed radial velocities of Milky Way satellites. For the inner satellites also the tangential motions are known (with large uncertainties however) [98, 168] and just as in our simple model they are larger than the typical tangential velocities of dark matter particles in the inner halo.

The total (mostly dark) surviving subhalo population is more extended and hotter than the dark matter while the distribution of orbits is similar [33]. Subhaloes tend to avoid the inner halo and those who lie near the centre at $z = 0$ move faster (both in the tangential and radial directions) than the dark matter particles, i.e. these inner subhaloes have large orbital energies and spend most of their time further away from the centre (see also Diemand et al. [33]).

Bibliography

- [1] S. J. Aarseth. *Gravitational N-Body Simulations*. Cambridge, UK, Cambridge University Press, 1. edition, January 2003. ISBN 0521432723.
- [2] S. J. Aarseth and K. Zare. A regularization of the three-body problem. *Celestial Mechanics*, 10:185–205, October 1974.
- [3] M. G. Abadi, J. F. Navarro, and M. Steinmetz. Stars beyond galaxies: the origin of extended luminous haloes around galaxies. *Monthly Notices of the Royal Astronomical Society*, 365:747–758, January 2006. doi: 10.1111/j.1365-2966.2005.09789.x.
- [4] H. Aceves and H. Velázquez. Preservation of Cuspy Profiles in Disk Galaxy Mergers. *Revista Mexicana de Astronomia y Astrofisica*, 42:41–46, April 2006.
- [5] F. C. Adams and G. Laughlin. A dying universe: the long-term fate and evolution of astrophysical objects. *Reviews of Modern Physics*, 69:337–372, 1997.
- [6] K. Ahn and P. R. Shapiro. Formation and evolution of self-interacting dark matter haloes. *Monthly Notices of the Royal Astronomical Society*, 363:1092–1110, November 2005. doi: 10.1111/j.1365-2966.2005.09492.x.
- [7] R. Barkana and A. Loeb. In the beginning: the first sources of light and the reionization of the universe. *Physics Reports.*, 349:125–238, July 2001.
- [8] J. Barnes and P. Hut. A Hierarchical $O(N \log N)$ Force-Calculation Algorithm. *Nature*, 324:446–449, December 1986.
- [9] G. Battaglia, A. Helmi, H. Morrison, P. Harding, E. W. Olszewski, M. Mateo, K. C. Freeman, J. Norris, and S. A. Sheckman. The radial velocity dispersion profile of the Galactic halo: constraining the density profile of the dark halo of the Milky Way. *Monthly Notices of the Royal Astronomical Society*, 364:433–442, December 2005. doi: 10.1111/j.1365-2966.2005.09367.x.
- [10] A. J. Benson, C. S. Frenk, C. G. Lacey, C. M. Baugh, and S. Cole. The effects of photoionization on galaxy formation - II. Satellite galaxies in the Local Group. *Monthly Notices of the Royal Astronomical Society*, 333:177–190, June 2002. doi: 10.1046/j.1365-8711.2002.05388.x.
- [11] J. L. Bentley. Multidimensional binary search trees used for associative searching. *Communications of the Association for Computing Machinery*, 18(9):509–517, 1975. ISSN 0001-0782. doi: 10.1145/361002.361007.

- [12] G. Bertone and D. Merritt. Dark Matter Dynamics and Indirect Detection. *Modern Physics Letters A*, 20:1021–1036, 2005. doi: 10.1142/S0217732305017391.
- [13] E. Bertschinger. Multiscale Gaussian Random Fields and Their Application to Cosmological Simulations. *Astrophysical Journal, Supplement*, 137:1–20, November 2001. doi: 10.1086/322526.
- [14] J. Binney. Discreteness effects in cosmological N-body simulations. *Monthly Notices of the Royal Astronomical Society*, 350:939–948, May 2004. doi: 10.1111/j.1365-2966.2004.07699.x.
- [15] J. Binney and S. Tremaine. *Galactic dynamics*. Princeton, NJ, Princeton University Press, 3. edition, 1987. ISBN 0691084459.
- [16] M. Boylan-Kolchin and C.-P. Ma. Major mergers of galaxy haloes: cuspy or cored inner density profile? *Monthly Notices of the Royal Astronomical Society*, 349:1117–1129, April 2004. doi: 10.1111/j.1365-2966.2004.07585.x.
- [17] J. S. Bullock, A. V. Kravtsov, and D. H. Weinberg. Reionization and the Abundance of Galactic Satellites. *Astrophysical Journal*, 539:517–521, August 2000. doi: 10.1086/309279.
- [18] C. Calcáneo-Roldán and B. Moore. Surface brightness of dark matter: Unique signatures of neutralino annihilation in the galactic halo. *Physical Review D*, 62(12):123005–+, December 2000.
- [19] R. Capuzzo-Dolcetta and A. Vicari. Dynamical friction on globular clusters in core-triaxial galaxies: is it a cause of massive black hole accretion? *Monthly Notices of the Royal Astronomical Society*, 356:899–912, January 2005. doi: 10.1111/j.1365-2966.2004.08433.x.
- [20] R. G. Carlberg, H. K. C. Yee, E. Ellingson, S. L. Morris, R. Abraham, P. Gravel, C. J. Pritchet, T. Smecker-Hane, F. D. A. Hartwick, J. E. Hesser, J. B. Hutchings, and J. B. Oke. The Average Mass Profile of Galaxy Clusters. *Astrophysical Journal, Letters*, 485:L13+, August 1997. doi: 10.1086/310801.
- [21] S. Chandrasekhar. Dynamical Friction. I. General Considerations: the Coefficient of Dynamical Friction. *Astrophysical Journal*, 97:255–+, March 1943.
- [22] M. Chiba and T. C. Beers. Kinematics of Metal-poor Stars in the Galaxy. III. Formation of the Stellar Halo and Thick Disk as Revealed from a Large Sample of Nonkinematically Selected Stars. *Astronomical Journal*, 119:2843–2865, June 2000. doi: 10.1086/301409.
- [23] A. L. Coil, B. F. Gerke, J. A. Newman, C.-P. Ma, R. Yan, M. C. Cooper, M. Davis, S. M. Faber, P. Guhathakurta, and D. C. Koo. The DEEP2 Galaxy Redshift Survey: Clustering of Groups and Group Galaxies at $z \sim 1$. *Astrophysical Journal*, 638:668–685, February 2006. doi: 10.1086/498885.

- [24] S. Cole and C. Lacey. The structure of dark matter haloes in hierarchical clustering models. *Monthly Notices of the Royal Astronomical Society*, 281:716–+, July 1996.
- [25] M. G. Coleman, G. S. Da Costa, J. Bland-Hawthorn, and K. C. Freeman. A Wide-Field Survey of the Fornax Dwarf Spheroidal Galaxy. *Astronomical Journal*, 129: 1443–1464, March 2005. doi: 10.1086/427966.
- [26] P. Colín, V. Avila-Reese, and O. Valenzuela. Substructure and Halo Density Profiles in a Warm Dark Matter Cosmology. *Astrophysical Journal*, 542:622–630, October 2000. doi: 10.1086/317057.
- [27] P. Colín, A. Klypin, O. Valenzuela, and S. Gottlöber. Dwarf Dark Matter Halos. *Astrophysical Journal*, 612:50–57, September 2004. doi: 10.1086/422463.
- [28] W. J. G. de Blok, S. S. McGaugh, A. Bosma, and V. C. Rubin. Mass Density Profiles of Low Surface Brightness Galaxies. *Astrophysical Journal, Letters*, 552: L23–L26, May 2001. doi: 10.1086/320262.
- [29] W. Dehnen. A Family of Potential-Density Pairs for Spherical Galaxies and Bulges. *Monthly Notices of the Royal Astronomical Society*, 265:250–+, November 1993.
- [30] W. Dehnen. Towards optimal softening in three-dimensional N-body codes - I. Minimizing the force error. *Monthly Notices of the Royal Astronomical Society*, 324:273–291, June 2001.
- [31] W. Dehnen. Phase-space mixing and the merging of cusps. *Monthly Notices of the Royal Astronomical Society*, 360:892–900, July 2005. doi: 10.1111/j.1365-2966.2005.09099.x.
- [32] J. Demmel. Applications of Parallel Computers. URL <http://www.cs.berkeley.edu/~demmel/cs267/>. Lecture Notes, 1996.
- [33] J. Diemand, B. Moore, and J. Stadel. Velocity and spatial biases in cold dark matter subhalo distributions. *Monthly Notices of the Royal Astronomical Society*, 352:535–546, August 2004. doi: 10.1111/j.1365-2966.2004.07940.x.
- [34] J. Diemand, B. Moore, and J. Stadel. Convergence and scatter of cluster density profiles. *Monthly Notices of the Royal Astronomical Society*, 353:624–632, September 2004. doi: 10.1111/j.1365-2966.2004.08094.x.
- [35] J. Diemand, B. Moore, J. Stadel, and S. Kazantzidis. Two-body relaxation in cold dark matter simulations. *Monthly Notices of the Royal Astronomical Society*, 348: 977–986, March 2004. doi: 10.1111/j.1365-2966.2004.07424.x.
- [36] J. Diemand, P. Madau, and B. Moore. The distribution and kinematics of early high- σ peaks in present-day haloes: implications for rare objects and old stellar populations. *Monthly Notices of the Royal Astronomical Society*, 364:367–383, December 2005. doi: 10.1111/j.1365-2966.2005.09604.x.

- [37] J. Diemand, B. Moore, and J. Stadel. Earth-mass dark-matter haloes as the first structures in the early Universe. *Nature*, 433:389–391, January 2005. doi: 10.1038/nature03270.
- [38] J. Diemand, M. Zemp, B. Moore, J. Stadel, and C. M. Carollo. Cusps in cold dark matter haloes. *Monthly Notices of the Royal Astronomical Society*, 364:665–673, December 2005. doi: 10.1111/j.1365-2966.2005.09601.x.
- [39] D. I. Dinescu, B. A. Keeney, S. R. Majewski, and T. M. Girard. Absolute Proper Motion of the Fornax Dwarf Spheroidal Galaxy from Photographic and Hubble Space Telescope WFPC2 Data. *Astronomical Journal*, 128:687–699, August 2004. doi: 10.1086/422491.
- [40] J. Dubinski and R. G. Carlberg. The structure of cold dark matter halos. *Astrophysical Journal*, 378:496–503, September 1991. doi: 10.1086/170451.
- [41] F. J. Dyson. Time without end: Physics and biology in an open universe. *Reviews of Modern Physics*, 51:447–460, July 1979.
- [42] A. Eckart, R. Genzel, T. Ott, and R. Schödel. Stellar orbits near Sagittarius A*. *Monthly Notices of the Royal Astronomical Society*, 331:917–934, April 2002. doi: 10.1046/j.1365-8711.2002.05237.x.
- [43] O. J. Eggen, D. Lynden-Bell, and A. R. Sandage. Evidence from the motions of old stars that the Galaxy collapsed. *Astrophysical Journal*, 136:748–+, November 1962.
- [44] S. Eidelman, K.G. Hayes, K.A. Olive, M. Aguilar-Benitez, C. Amsler, D. Asner, K.S. Babu, R.M. Barnett, J. Beringer, P.R. Burchat, C.D. Carone, C. Caso, G. Conforto, O. Dahl, G. D’Ambrosio, M. Doser, J.L. Feng, T. Gherghetta, L. Gibbons, M. Goodman, C. Grab, D.E. Groom, A. Gurtu, K. Hagiwara, J.J. Hernández-Rey, K. Hikasa, K. Honscheid, H. Jawahery, C. Kolda, Kwon Y., M.L. Mangano, A.V. Manohar, J. March-Russell, A. Masoni, R. Miquel, K. Mönig, H. Murayama, K. Nakamura, S. Navas, L. Pape, C. Patrignani, A. Piepke, G. Raffelt, M. Roos, M. Tanabashi, J. Terning, N.A. Törnqvist, T.G. Trippe, P. Vogel, C.G. Wohl, R.L. Workman, W.-M. Yao, P.A. Zyla, B. Armstrong, P.S. Gee, G. Harper, K.S. Lugovsky, S.B. Lugovsky, V.S. Lugovsky, A. Rom, M. Artuso, E. Barberio, M. Battaglia, H. Bichsel, O. Biebel, P. Bloch, R.N. Cahn, D. Casper, A. Cattai, R.S. Chivukula, G. Cowan, T. Damour, K. Desler, M.A. Dobbs, M. Drees, A. Edwards, D.A. Edwards, V.D. Elvira, J. Erler, V.V. Ezhela, W. Fetscher, B.D. Fields, B. Foster, D. Froidevaux, M. Fukugita, T.K. Gaiser, L. Garren, H.-J. Gerber, G. Gerbier, F.J. Gilman, H.E. Haber, C. Hagmann, J. Hewett, I. Hinchliffe, C.J. Hogan, G. Höhler, P. Igo-Kemenes, J.D. Jackson, K.F. Johnson, D. Karlen, B. Kayser, D. Kirkby, S.R. Klein, K. Kleinknecht, I.G. Knowles, P. Kreitz, Yu.V. Kuyanov, O. Lahav, P. Langacker, A. Liddle, L. Littenberg, D.M. Manley, A.D. Martin, M. Narain, P. Nason, Y. Nir, J.A. Peacock, H.R. Quinn, S. Raby, B.N. Ratcliff, E.A. Razuvaev, B. Renk, G. Rolandi,

- M.T. Ronan, L.J. Rosenberg, C.T. Sachrajda, Y. Sakai, A.I. Sanda, S. Sarkar, M. Schmitt, O. Schneider, D. Scott, W.G. Seligman, M.H. Shaevitz, T. Sjöstrand, G.F. Smoot, S. Spanier, H. Spieler, N.J.C. Spooner, M. Srednicki, A. Stahl, T. Stanev, M. Suzuki, N.P. Tkachenko, G.H. Trilling, G. Valencia, K. van Bibber, M.G. Vincter, D. Ward, B.R. Webber, M. Whalley, L. Wolfenstein, J. Womersley, C.L. Woody, O.V. Zenin, and R.-Y. Zhu. Review of Particle Physics. *Physics Letters B*, 592:1+, 2004. URL <http://pdg.lbl.gov>.
- [45] V. R. Eke, S. Cole, and C. S. Frenk. Cluster evolution as a diagnostic for Omega. *Monthly Notices of the Royal Astronomical Society*, 282:263–280, September 1996.
- [46] A. Faltenbacher and W. G. Mathews. On the dynamics of the satellite galaxies in NGC 5044. *Monthly Notices of the Royal Astronomical Society*, 362:498–504, September 2005. doi: 10.1111/j.1365-2966.2005.09334.x.
- [47] L. Ferrarese and D. Merritt. A Fundamental Relation between Supermassive Black Holes and Their Host Galaxies. *Astrophysical Journal, Letters*, 539:L9–L12, August 2000. doi: 10.1086/312838.
- [48] R. A. Flores and J. R. Primack. Observational and theoretical constraints on singular dark matter halos. *Astrophysical Journal, Letters*, 427:L1–L4, May 1994. doi: 10.1086/187350.
- [49] A. S. Font, K. V. Johnston, J. S. Bullock, and B. E. Robertson. Phase-Space Distributions of Chemical Abundances in Milky Way-Type Galaxy Halos. *Astrophysical Journal*, 646:886–898, August 2006. doi: 10.1086/505131.
- [50] D. A. Forbes, K. L. Masters, D. Minniti, and P. Barmby. The elliptical galaxy formerly known as the Local Group: merging the globular cluster systems. *Astronomy and Astrophysics*, 358:471–480, June 2000.
- [51] K. Freeman and J. Bland-Hawthorn. The New Galaxy: Signatures of Its Formation. *Annual Review of Astron and Astrophys*, 40:487–537, 2002. doi: 10.1146/annurev.astro.40.060401.093840.
- [52] T. Fukushige and J. Makino. On the Origin of Cusps in Dark Matter Halos. *Astrophysical Journal, Letters*, 477:L9+, March 1997. doi: 10.1086/310516.
- [53] T. Fukushige and J. Makino. Structure of Dark Matter Halos from Hierarchical Clustering. II. Dependence of Cosmological Models in Cluster-sized Halos. *Astrophysical Journal*, 588:674–679, May 2003. doi: 10.1086/374206.
- [54] T. Fukushige, A. Kawai, and J. Makino. Structure of Dark Matter Halos from Hierarchical Clustering. III. Shallowing of the Inner Cusp. *Astrophysical Journal*, 606:625–634, May 2004. doi: 10.1086/383192.
- [55] J. S. Gallagher, III and R. F. G. Wyse. Dwarf spheroidal galaxies: Keystones of galaxy evolution. *Publications of the ASP*, 106:1225–1238, December 1994.

- [56] L. Gao, A. Loeb, P. J. E. Peebles, S. D. M. White, and A. Jenkins. Early Formation and Late Merging of the Giant Galaxies. *Astrophysical Journal*, 614:17–25, October 2004. doi: 10.1086/423444.
- [57] L. Gao, S. D. M. White, A. Jenkins, C. S. Frenk, and V. Springel. Early structure in Λ CDM. *Monthly Notices of the Royal Astronomical Society*, 363:379–392, October 2005. doi: 10.1111/j.1365-2966.2005.09509.x.
- [58] K. Gebhardt, R. Bender, G. Bower, A. Dressler, S. M. Faber, A. V. Filippenko, R. Green, C. Grillmair, L. C. Ho, J. Kormendy, T. R. Lauer, J. Magorrian, J. Pinkney, D. Richstone, and S. Tremaine. A Relationship between Nuclear Black Hole Mass and Galaxy Velocity Dispersion. *Astrophysical Journal, Letters*, 539:L13–L16, August 2000. doi: 10.1086/312840.
- [59] R. Genzel, A. Eckart, T. Ott, and F. Eisenhauer. On the nature of the dark mass in the centre of the Milky Way. *Monthly Notices of the Royal Astronomical Society*, 291:219–234, October 1997.
- [60] A. M. Ghez, S. Salim, S. D. Hornstein, A. Tanner, J. R. Lu, M. Morris, E. E. Becklin, and G. Duchêne. Stellar Orbits around the Galactic Center Black Hole. *Astrophysical Journal*, 620:744–757, February 2005. doi: 10.1086/427175.
- [61] S. Ghigna, B. Moore, F. Governato, G. Lake, T. Quinn, and J. Stadel. Dark matter haloes within clusters. *Monthly Notices of the Royal Astronomical Society*, 300:146–162, October 1998.
- [62] S. Ghigna, B. Moore, F. Governato, G. Lake, T. Quinn, and J. Stadel. Density Profiles and Substructure of Dark Matter Halos: Converging Results at Ultra-High Numerical Resolution. *Astrophysical Journal*, 544:616–628, December 2000. doi: 10.1086/317221.
- [63] O. Y. Gnedin and J. R. Primack. Dark Matter Profile in the Galactic Center. *Physical Review Letters*, 93(6):061302–+, August 2004. doi: 10.1103/PhysRevLett.93.061302.
- [64] T. Goerdt, B. Moore, J. I. Read, J. Stadel, and M. Zemp. Does the Fornax dwarf spheroidal have a central cusp or core? *Monthly Notices of the Royal Astronomical Society*, 368:1073–1077, May 2006. doi: 10.1111/j.1365-2966.2006.10182.x.
- [65] E. K. Grebel, J. S. Gallagher, III, and D. Harbeck. The Progenitors of Dwarf Spheroidal Galaxies. *Astronomical Journal*, 125:1926–1939, April 2003. doi: 10.1086/368363.
- [66] F. Haardt and P. Madau. Radiative Transfer in a Clumpy Universe. II. The Ultraviolet Extragalactic Background. *Astrophysical Journal*, 461:20–+, April 1996. doi: 10.1086/177035.

- [67] S. H. Hansen and B. Moore. A universal density slope - Velocity anisotropy relation for relaxed structures. *New Astronomy*, 11:333–338, March 2006. doi: 10.1016/j.newast.2005.09.001.
- [68] S. H. Hansen, D. Egli, L. Hollenstein, and C. Salzmann. Dark matter distribution function from non-extensive statistical mechanics. *New Astronomy*, 10:379–384, April 2005. doi: 10.1016/j.newast.2005.01.005.
- [69] S. H. Hansen, B. Moore, M. Zemp, and J. Stadel. A universal velocity distribution of relaxed collisionless structures. *Journal of Cosmology and Astro-Particle Physics*, 1:14–+, January 2006. doi: 10.1088/1475-7516/2006/01/014.
- [70] X. Hernandez and G. Gilmore. Dynamical friction in dwarf galaxies. *Monthly Notices of the Royal Astronomical Society*, 297:517–525, June 1998.
- [71] L. Hernquist. An analytical model for spherical galaxies and bulges. *Astrophysical Journal*, 356:359–364, June 1990. doi: 10.1086/168845.
- [72] L. Hernquist and M. D. Weinberg. Simulations of satellite orbital decay. *Monthly Notices of the Royal Astronomical Society*, 238:407–416, May 1989.
- [73] P. F. Hopkins, L. Hernquist, T. J. Cox, T. Di Matteo, B. Robertson, and V. Springel. A Unified, Merger-driven Model of the Origin of Starbursts, Quasars, the Cosmic X-Ray Background, Supermassive Black Holes, and Galaxy Spheroids. *Astrophysical Journal, Supplement*, 163:1–49, March 2006. doi: 10.1086/499298.
- [74] J. N. Islam. Possible Ultimate Fate of the Universe. *Quarterly Journal of the Royal Astronomical Society*, 18:3–+, March 1977.
- [75] R. R. Islam, J. E. Taylor, and J. Silk. Massive black hole remnants of the first stars in galactic haloes. *Monthly Notices of the Royal Astronomical Society*, 340: 647–656, April 2003. doi: 10.1046/j.1365-8711.2003.06329.x.
- [76] Ž. Ivezić, J. Goldston, K. Finlator, G. R. Knapp, B. Yanny, T. A. McKay, S. Amrose, K. Krisciunas, B. Willman, S. Anderson, C. Schaber, D. Erb, C. Logan, C. Stubbs, B. Chen, E. Neilsen, A. Uomoto, J. R. Pier, X. Fan, J. E. Gunn, R. H. Lupton, C. M. Rockosi, D. Schlegel, M. A. Strauss, J. Annis, J. Brinkmann, I. Csabai, M. Doi, M. Fukugita, G. S. Hennessy, R. B. Hindsley, B. Margon, J. A. Munn, H. J. Newberg, D. P. Schneider, J. A. Smith, G. P. Szokoly, A. R. Thakar, M. S. Vogeley, P. Waddell, N. Yasuda, and D. G. York. Candidate RR Lyrae Stars Found in Sloan Digital Sky Survey Commissioning Data. *Astronomical Journal*, 120:963–977, August 2000. doi: 10.1086/301455.
- [77] N. Katz and S. D. M. White. Hierarchical galaxy formation - Overmerging and the formation of an X-ray cluster. *Astrophysical Journal*, 412:455–478, August 1993. doi: 10.1086/172935.

- [78] N. Katz, T. Quinn, E. Bertschinger, and J. M. Gelb. Formation of Quasars at High Redshift. *Monthly Notices of the Royal Astronomical Society*, 270:L71+, October 1994.
- [79] G. Kauffmann, S. D. M. White, and B. Guiderdoni. The Formation and Evolution of Galaxies Within Merging Dark Matter Haloes. *Monthly Notices of the Royal Astronomical Society*, 264:201–+, September 1993.
- [80] S. Kazantzidis, J. Magorrian, and B. Moore. Generating Equilibrium Dark Matter Halos: Inadequacies of the Local Maxwellian Approximation. *Astrophysical Journal*, 601:37–46, January 2004. doi: 10.1086/380192.
- [81] S. Khochfar and A. Burkert. Orbital parameters of merging dark matter halos. *Astronomy and Astrophysics*, 445:403–412, January 2006. doi: 10.1051/0004-6361:20053241.
- [82] J. T. Kleyna, M. I. Wilkinson, G. Gilmore, and N. W. Evans. A Dynamical Fossil in the Ursa Minor Dwarf Spheroidal Galaxy. *Astrophysical Journal, Letters*, 588: L21–L24, May 2003. doi: 10.1086/375522.
- [83] A. Klypin, A. V. Kravtsov, O. Valenzuela, and F. Prada. Where Are the Missing Galactic Satellites? *Astrophysical Journal*, 522:82–92, September 1999. doi: 10.1086/307643.
- [84] A. Klypin, A. V. Kravtsov, J. S. Bullock, and J. R. Primack. Resolving the Structure of Cold Dark Matter Halos. *Astrophysical Journal*, 554:903–915, June 2001. doi: 10.1086/321400.
- [85] A. V. Kravtsov and O. Y. Gnedin. Formation of Globular Clusters in Hierarchical Cosmology. *Astrophysical Journal*, 623:650–665, April 2005. doi: 10.1086/428636.
- [86] M. Kuhlen, L. E. Strigari, A. R. Zentner, J. S. Bullock, and J. R. Primack. Dark energy and dark matter haloes. *Monthly Notices of the Royal Astronomical Society*, 357:387–400, February 2005. doi: 10.1111/j.1365-2966.2005.08663.x.
- [87] K. Kuijken and J. Dubinski. Lowered Evans Models - Analytic Distribution Functions of Oblate Halo Potentials. *Monthly Notices of the Royal Astronomical Society*, 269:13–+, July 1994.
- [88] C. Lacey and S. Cole. Merger rates in hierarchical models of galaxy formation. *Monthly Notices of the Royal Astronomical Society*, 262:627–649, June 1993.
- [89] F. Leeuwin, F. Combes, and J. Binney. N-body simulations with perturbation particles. I - Method and tests. *Monthly Notices of the Royal Astronomical Society*, 262:1013–1022, June 1993.

- [90] E. L. Lokas. Dark matter distribution in dwarf spheroidal galaxies. *Monthly Notices of the Royal Astronomical Society*, 333:697–708, July 2002. doi: 10.1046/j.1365-8711.2002.05457.x.
- [91] J. M. Lotz, R. Telford, H. C. Ferguson, B. W. Miller, M. Stiavelli, and J. Mack. Dynamical Friction in DE Globular Cluster Systems. *Astrophysical Journal*, 552: 572–581, May 2001. doi: 10.1086/320545.
- [92] A. V. Macciò, C. Quercellini, R. Mainini, L. Amendola, and S. A. Bonometto. Coupled dark energy: Parameter constraints from N-body simulations. *Physical Review D*, 69(12):123516–+, June 2004. doi: 10.1103/PhysRevD.69.123516.
- [93] A. D. Mackey and G. F. Gilmore. Surface brightness profiles and structural parameters for globular clusters in the Fornax and Sagittarius dwarf spheroidal galaxies. *Monthly Notices of the Royal Astronomical Society*, 340:175–190, March 2003. doi: 10.1046/j.1365-8711.2003.06275.x.
- [94] P. Madau. From the Earliest Seeds to Today’s Supermassive Black Holes. In A. Merloni, S. Nayakshin, and R. A. Sunyaev, editors, *Growing Black Holes: Accretion in a Cosmological Context*, pages 3–540, 2005. doi: 10.1007/11403913_1.
- [95] S. R. Majewski, J. C. Ostheimer, R. J. Patterson, W. E. Kunkel, K. V. Johnston, and D. Geisler. Exploring Halo Substructure with Giant Stars. II. Mapping the Extended Structure of the Carina Dwarf Spheroidal Galaxy. *Astronomical Journal*, 119:760–776, February 2000. doi: 10.1086/301228.
- [96] J. Makino, T. Fukushige, M. Koga, and K. Namura. GRAPE-6: Massively-Parallel Special-Purpose Computer for Astrophysical Particle Simulations. *Publications of the ASJ*, 55:1163–1187, December 2003.
- [97] J. Makino, P. Hut, M. Kaplan, and H. Saygin. A time-symmetric block time-step algorithm for N-body simulations. *New Astronomy*, 12:124–133, November 2006. doi: 10.1016/j.newast.2006.06.003.
- [98] M. L. Mateo. Dwarf Galaxies of the Local Group. *Annual Review of Astron and Astrophys*, 36:435–506, 1998. doi: 10.1146/annurev.astro.36.1.435.
- [99] Max-Planck-Institut für Astrophysik. The Millennium Simulation Project. URL <http://www.mpa-garching.mpg.de/galform/virgo/millennium/>. Project webpage, 2005.
- [100] L. Mayer, C. Mastropietro, J. Wadsley, J. Stadel, and B. Moore. Simultaneous ram pressure and tidal stripping; how dwarf spheroidals lost their gas. *Monthly Notices of the Royal Astronomical Society*, 369:1021–1038, July 2006. doi: 10.1111/j.1365-2966.2006.10403.x.

- [101] D. Merritt. Evolution of the Dark Matter Distribution at the Galactic Center. *Physical Review Letters*, 92(20):201304–+, May 2004. doi: 10.1103/PhysRevLett.92.201304.
- [102] D. Merritt. Single and Binary Black Holes and their Influence on Nuclear Structure. In L. C. Ho, editor, *Coevolution of Black Holes and Galaxies*, pages 263–+, 2004.
- [103] D. Merritt and M. Milosavljević. Massive Black Hole Binary Evolution. *Living Reviews in Relativity*, 8:8–+, November 2005.
- [104] D. Merritt, M. Milosavljević, L. Verde, and R. Jimenez. Dark Matter Spikes and Annihilation Radiation from the Galactic Center. *Physical Review Letters*, 88(19):191301–+, May 2002.
- [105] D. Merritt, S. Piatek, S. Portegies Zwart, and M. Hemsendorf. Core Formation by a Population of Massive Remnants. *Astrophysical Journal, Letters*, 608:L25–L28, June 2004. doi: 10.1086/422252.
- [106] P. Monaco and F. Fontanot. Feedback from quasars in star-forming galaxies and the triggering of massive galactic winds. *Monthly Notices of the Royal Astronomical Society*, 359:283–294, May 2005. doi: 10.1111/j.1365-2966.2005.08884.x.
- [107] B. Moore. Evidence against Dissipationless Dark Matter from Observations of Galaxy Haloes. *Nature*, 370:629–+, August 1994. doi: 10.1038/370629a0.
- [108] B. Moore. Constraints on the Global Mass-to-Light Ratios and on the Extent of Dark Matter Halos in Globular Clusters and Dwarf Spheroidals. *Astrophysical Journal, Letters*, 461:L13+, April 1996. doi: 10.1086/309998.
- [109] B. Moore. The Dark Matter Crisis (Plenary Talk). In J. C. Wheeler and H. Martel, editors, *AIP Conf. Proc. 586: 20th Texas Symposium on relativistic astrophysics*, pages 73–+, 2001.
- [110] B. Moore, F. Governato, T. Quinn, J. Stadel, and G. Lake. Resolving the Structure of Cold Dark Matter Halos. *Astrophysical Journal, Letters*, 499:L5+, May 1998. doi: 10.1086/311333.
- [111] B. Moore, S. Ghigna, F. Governato, G. Lake, T. Quinn, J. Stadel, and P. Tozzi. Dark Matter Substructure within Galactic Halos. *Astrophysical Journal, Letters*, 524:L19–L22, October 1999. doi: 10.1086/312287.
- [112] B. Moore, T. Quinn, F. Governato, J. Stadel, and G. Lake. Cold collapse and the core catastrophe. *Monthly Notices of the Royal Astronomical Society*, 310:1147–1152, December 1999.

- [113] B. Moore, C. Calcáneo-Roldán, J. Stadel, T. Quinn, G. Lake, S. Ghigna, and F. Governato. Dark matter in Draco and the Local Group: Implications for direct detection experiments. *Physical Review D*, 64(6):063508–+, September 2001.
- [114] B. Moore, S. Kazantzidis, J. Diemand, and J. Stadel. The origin and tidal evolution of cuspy triaxial haloes. *Monthly Notices of the Royal Astronomical Society*, 354: 522–528, October 2004. doi: 10.1111/j.1365-2966.2004.08211.x.
- [115] B. Moore, J. Diemand, P. Madau, M. Zemp, and J. Stadel. Globular clusters, satellite galaxies and stellar haloes from early dark matter peaks. *Monthly Notices of the Royal Astronomical Society*, 368:563–570, May 2006. doi: 10.1111/j.1365-2966.2006.10116.x.
- [116] J. F. Navarro, C. S. Frenk, and Simon D. M. White. The Structure of Cold Dark Matter Halos. *Astrophysical Journal*, 462:563–+, May 1996. doi: 10.1086/177173.
- [117] J. F. Navarro, E. Hayashi, C. Power, A. R. Jenkins, C. S. Frenk, S. D. M. White, V. Springel, J. Stadel, and T. R. Quinn. The inner structure of Λ CDM haloes - III. Universality and asymptotic slopes. *Monthly Notices of the Royal Astronomical Society*, 349:1039–1051, April 2004. doi: 10.1111/j.1365-2966.2004.07586.x.
- [118] K. S. Oh and D. N. C. Lin. Nucleation of Dwarf Galaxies in the Virgo Cluster. *Astrophysical Journal*, 543:620–633, November 2000. doi: 10.1086/317118.
- [119] K. S. Oh, D. N. C. Lin, and H. B. Richer. Globular Clusters in the Fornax Dwarf Spheroidal Galaxy. *Astrophysical Journal*, 531:727–738, March 2000. doi: 10.1086/308477.
- [120] G. Parmentier and G. Gilmore. New light on the initial mass function of the Galactic halo globular clusters. *Monthly Notices of the Royal Astronomical Society*, 363:326–336, October 2005. doi: 10.1111/j.1365-2966.2005.09455.x.
- [121] G. Parmentier and E. K. Grebel. On the origin of the radial mass density profile of the Galactic halo globular cluster system. *Monthly Notices of the Royal Astronomical Society*, 359:615–623, May 2005. doi: 10.1111/j.1365-2966.2005.08925.x.
- [122] P. J. E. Peebles. Large-scale background temperature and mass fluctuations due to scale-invariant primeval perturbations. *Astrophysical Journal, Letters*, 263:L1–L5, December 1982. doi: 10.1086/183911.
- [123] P. J. E. Peebles. Dark matter and the origin of galaxies and globular star clusters. *Astrophysical Journal*, 277:470–477, February 1984. doi: 10.1086/161714.
- [124] A. R. Plastino and A. Plastino. Stellar polytropes and Tsallis’ entropy. *Physics Letters A*, 174:384–386, March 1993. doi: 10.1016/0375-9601(93)90195-6.

- [125] C. Power, J. F. Navarro, A. Jenkins, C. S. Frenk, Simon D. M. White, V. Springel, J. Stadel, and T. Quinn. The inner structure of Λ CDM haloes - I. A numerical convergence study. *Monthly Notices of the Royal Astronomical Society*, 338:14–34, January 2003. doi: 10.1046/j.1365-8711.2003.05925.x.
- [126] F. Prada, A. Klypin, J. Flix, M. Martínez, and E. Simonneau. Dark Matter Annihilation in the Milky Way Galaxy: Effects of Baryonic Compression. *Physical Review Letters*, 93(24):241301–+, December 2004. doi: 10.1103/PhysRevLett.93.241301.
- [127] B. J. Pritzl, K. A. Venn, and M. Irwin. A Comparison of Elemental Abundance Ratios in Globular Clusters, Field Stars, and Dwarf Spheroidal Galaxies. *Astronomical Journal*, 130:2140–2165, November 2005. doi: 10.1086/432911.
- [128] T. Quinn, N. Katz, J. Stadel, and G. Lake. Time stepping N-body simulations. *preprint (astro-ph/9710043)*, October 1997.
- [129] D. Reed, F. Governato, L. Verde, J. Gardner, T. Quinn, J. Stadel, D. Merritt, and G. Lake. Evolution of the density profiles of dark matter haloes. *Monthly Notices of the Royal Astronomical Society*, 357:82–96, February 2005. doi: 10.1111/j.1365-2966.2005.08612.x.
- [130] M. W. Reinsch. A simple expression for the terms in the Baker-Campbell-Hausdorff series. *Journal of Mathematical Physics*, 41:2434–2442, April 2000.
- [131] B. Robertson, J. S. Bullock, A. S. Font, K. V. Johnston, and L. Hernquist. A Cold Dark Matter, Stellar Feedback, and the Galactic Halo Abundance Pattern. *Astrophysical Journal*, 632:872–881, October 2005. doi: 10.1086/452619.
- [132] P. Saha and S. Tremaine. Long-term planetary integration with individual time steps. *Astronomical Journal*, 108:1962–1969, November 1994. doi: 10.1086/117210.
- [133] L. Sales and D. G. Lambas. Satellite number density profiles of primary galaxies in the 2dFGRS. *Monthly Notices of the Royal Astronomical Society*, 356:1045–1052, January 2005. doi: 10.1111/j.1365-2966.2004.08518.x.
- [134] P. Salucci and A. Burkert. Dark Matter Scaling Relations. *Astrophysical Journal, Letters*, 537:L9–L12, July 2000. doi: 10.1086/312747.
- [135] R. Schödel, T. Ott, R. Genzel, R. Hofmann, M. Lehnert, A. Eckart, N. Mouawad, T. Alexander, M. J. Reid, R. Lenzen, M. Hartung, F. Lacombe, D. Rouan, E. Gendron, G. Rousset, A.-M. Lagrange, W. Brandner, N. Ageorges, C. Lidman, A. F. M. Moorwood, J. Spyromilio, N. Hubin, and K. M. Menten. A star in a 15.2-year orbit around the supermassive black hole at the centre of the Milky Way. *Nature*, 419:694–696, October 2002.

- [136] L. Searle and R. Zinn. Compositions of halo clusters and the formation of the galactic halo. *Astrophysical Journal*, 225:357–379, October 1978. doi: 10.1086/156499.
- [137] R. K. Sheth and G. Tormen. Large-scale bias and the peak background split. *Monthly Notices of the Royal Astronomical Society*, 308:119–126, September 1999.
- [138] J. Silk. Ultraluminous starbursts from supermassive black hole-induced outflows. *Monthly Notices of the Royal Astronomical Society*, 364:1337–1342, December 2005. doi: 10.1111/j.1365-2966.2005.09672.x.
- [139] J. D. Simon, A. D. Bolatto, A. Leroy, L. Blitz, and E. L. Gates. High-Resolution Measurements of the Halos of Four Dark Matter-Dominated Galaxies: Deviations from a Universal Density Profile. *Astrophysical Journal*, 621:757–776, March 2005. doi: 10.1086/427684.
- [140] R. D. Skeel and C. W. Gear. Does variable step size ruin a symplectic integrator? *Physica D Nonlinear Phenomena*, 60:311–313, November 1992. doi: 10.1016/0167-2789(92)90247-K.
- [141] V. Springel. The cosmological simulation code GADGET-2. *Monthly Notices of the Royal Astronomical Society*, 364:1105–1134, December 2005. doi: 10.1111/j.1365-2966.2005.09655.x.
- [142] V. Springel, S. D. M. White, G. Tormen, and G. Kauffmann. Populating a cluster of galaxies - I. Results at $[formmu2]z=0$. *Monthly Notices of the Royal Astronomical Society*, 328:726–750, December 2001. doi: 10.1046/j.1365-8711.2001.04912.x.
- [143] V. Springel, S. D. M. White, A. Jenkins, C. S. Frenk, N. Yoshida, L. Gao, J. Navarro, R. Thacker, D. Croton, J. Helly, J. A. Peacock, S. Cole, P. Thomas, H. Couchman, A. Evrard, J. Colberg, and F. Pearce. Simulations of the formation, evolution and clustering of galaxies and quasars. *Nature*, 435:629–636, June 2005. doi: 10.1038/nature03597.
- [144] J. G. Stadel. Cosmological N-body simulations and their analysis. *Ph.D. Thesis, University of Washington*, 2001.
- [145] F. Stoehr. Circular velocity profiles of dark matter haloes. *Monthly Notices of the Royal Astronomical Society*, 365:147–152, January 2006. doi: 10.1111/j.1365-2966.2005.09676.x.
- [146] F. Stoehr, S. D. M. White, G. Tormen, and V. Springel. The satellite population of the Milky Way in a Λ CDM universe. *Monthly Notices of the Royal Astronomical Society*, 335:L84–L88, October 2002. doi: 10.1046/j.1365-8711.2002.05891.x.
- [147] J. Strader, J. P. Brodie, and D. A. Forbes. Metal-Poor Globular Clusters and Galaxy Formation. *Astronomical Journal*, 127:3431–3436, June 2004. doi: 10.1086/420995.

- [148] R. A. Swaters, B. F. Madore, F. C. van den Bosch, and M. Balcells. The Central Mass Distribution in Dwarf and Low Surface Brightness Galaxies. *Astrophysical Journal*, 583:732–751, February 2003. doi: 10.1086/345426.
- [149] A. Tasitsiomi, A. V. Kravtsov, S. Gottlöber, and A. A. Klypin. Density Profiles of Λ CDM Clusters. *Astrophysical Journal*, 607:125–139, May 2004. doi: 10.1086/383219.
- [150] J. E. Taylor and J. F. Navarro. The Phase-Space Density Profiles of Cold Dark Matter Halos. *Astrophysical Journal*, 563:483–488, December 2001. doi: 10.1086/324031.
- [151] C. Thom, C. Flynn, M. S. Bessell, J. Hänninen, T. C. Beers, N. Christlieb, D. James, J. Holmberg, and B. K. Gibson. Kinematics of the Galactic halo from horizontal branch stars in the Hamburg/ESO survey. *Monthly Notices of the Royal Astronomical Society*, 360:354–359, June 2005. doi: 10.1111/j.1365-2966.2005.09038.x.
- [152] S. D. Tremaine. The formation of the nuclei of galaxies. II - The local group. *Astrophysical Journal*, 203:345–351, January 1976.
- [153] S. D. Tremaine, J. P. Ostriker, and L. Spitzer, Jr. The formation of the nuclei of galaxies. I - M31. *Astrophysical Journal*, 196:407–411, March 1975.
- [154] C. Tsallis. Possible generalization of Boltzmann-Gibbs statistics. *Journal of Statistical Physics*, 52:479–487, July 1988. doi: 10.1007/BF01016429.
- [155] R. B. Tully, R. S. Somerville, N. Trentham, and M. A. W. Verheijen. Squelched Galaxies and Dark Halos. *Astrophysical Journal*, 569:573–581, April 2002. doi: 10.1086/339425.
- [156] F. C. van den Bosch. The universal mass accretion history of cold dark matter haloes. *Monthly Notices of the Royal Astronomical Society*, 331:98–110, March 2002. doi: 10.1046/j.1365-8711.2002.05171.x.
- [157] F. C. van den Bosch and R. A. Swaters. Dwarf galaxy rotation curves and the core problem of dark matter haloes. *Monthly Notices of the Royal Astronomical Society*, 325:1017–1038, August 2001. doi: 10.1046/j.1365-8711.2001.04456.x.
- [158] F. C. van den Bosch, X. Yang, H. J. Mo, and P. Norberg. The abundance and radial distribution of satellite galaxies. *Monthly Notices of the Royal Astronomical Society*, 356:1233–1248, February 2005. doi: 10.1111/j.1365-2966.2004.08407.x.
- [159] M. Volonteri and R. Perna. Dynamical evolution of intermediate-mass black holes and their observable signatures in the nearby Universe. *Monthly Notices of the Royal Astronomical Society*, 358:913–922, April 2005. doi: 10.1111/j.1365-2966.2005.08832.x.

- [160] M. Volonteri and M. J. Rees. Rapid Growth of High-Redshift Black Holes. *Astrophysical Journal*, 633:624–629, November 2005. doi: 10.1086/466521.
- [161] M. Volonteri and M. J. Rees. Quasars at $z=6$: The Survival of the Fittest. *Astrophysical Journal*, 650:669–678, October 2006. doi: 10.1086/507444.
- [162] J.-M. Wang, Y.-M. Chen, and C. Hu. Feedback Limits Rapid Growth of Seed Black Holes at High Redshift. *Astrophysical Journal, Letters*, 637:L85–L88, February 2006. doi: 10.1086/500557.
- [163] R. H. Wechsler, J. S. Bullock, J. R. Primack, A. V. Kravtsov, and A. Dekel. Concentrations of Dark Halos from Their Assembly Histories. *Astrophysical Journal*, 568:52–70, March 2002. doi: 10.1086/338765.
- [164] H. Weyl. *The Classical Groups: Their Invariants and Representations*. Princeton, NJ, Princeton University Press, 2. edition, October 1997. ISBN 0691057567.
- [165] S. D. M. White. Simulations of sinking satellites. *Astrophysical Journal*, 274: 53–61, November 1983. doi: 10.1086/161425.
- [166] S. D. M. White and M. J. Rees. Core condensation in heavy halos - A two-stage theory for galaxy formation and clustering. *Monthly Notices of the Royal Astronomical Society*, 183:341–358, May 1978.
- [167] S. D. M. White and V. Springel. Where Are the First Stars Now? In A. Weiss, T. G. Abel, and V. Hill, editors, *The First Stars: Proceedings of the MPA/ESO Workshop Held at Garching, Germany, 4-6 August 1999, ESO ASTROPHYSICS SYMPOSIA. ISBN 3-540-67222-2. Edited by A. Weiss, T.G. Abel, and V. Hill. Springer-Verlag, 2000, p. 327, pages 327–+, 2000. doi: 10.1007/10719504_62.*
- [168] M. I. Wilkinson and N. W. Evans. The present and future mass of the Milky Way halo. *Monthly Notices of the Royal Astronomical Society*, 310:645–662, December 1999.
- [169] R. F. G. Wyse and G. Gilmore. The Galactic spheroid - What is Population II? *Astronomical Journal*, 95:1404–1414, May 1988. doi: 10.1086/114738.
- [170] R. F. G. Wyse and G. Gilmore. Chemistry and Kinematics in the Solar Neighborhood: Implications for Stellar Populations and for Galaxy Evolution. *Astronomical Journal*, 110:2771–+, December 1995. doi: 10.1086/117729.
- [171] H. Yoshida. Recent Progress in the Theory and Application of Symplectic Integrators. *Celestial Mechanics and Dynamical Astronomy*, 56:27–+, 1993.
- [172] Q. Yu and S. Tremaine. Ejection of Hypervelocity Stars by the (Binary) Black Hole in the Galactic Center. *Astrophysical Journal*, 599:1129–1138, December 2003. doi: 10.1086/379546.

- [173] M. Zemp. The Stability of Dark Matter Cusps. *Diploma Thesis, ETH Zurich*, 2003. URL <http://e-collection.ethbib.ethz.ch/cgi-bin/show.pl?type=dipl&nr=236>.
- [174] M. Zemp, J. Stadel, B. Moore, and C. M. Carollo. An optimum time-stepping scheme for N-body simulations. *preprint (astro-ph/0606589)*, June 2006.
- [175] D. H. Zhao, H. J. Mo, Y. P. Jing, and G. Börner. The growth and structure of dark matter haloes. *Monthly Notices of the Royal Astronomical Society*, 339:12–24, February 2003. doi: 10.1046/j.1365-8711.2003.06135.x.
- [176] H. Zhao. Analytical models for galactic nuclei. *Monthly Notices of the Royal Astronomical Society*, 278:488–496, January 1996.

Curriculum vitae

Personal Details

Name	Marcel Zemp
Date of birth	June 7, 1977
Place of birth	Wolhusen (LU)
Citizenship	Risch (ZG) and Escholzmatt (LU)
Nationality	Swiss

Education

04/2003 - 09/2006	Doctorate in Physics, ETH Zurich
10/1997 - 03/2003	Diploma in Physics, ETH Zurich
08/1990 - 07/1997	Matura Typus C (Mathematics), Kantonsschule Zug

Teaching Experience

10/2003 - 07/2006	Diploma in Didactics, ETH Zurich
04/2003 - 09/2006	Teaching Assistant for physics courses

Job Experience

10/1999 - 10/2000	Technical Assistant, ATP Hydraulik AG
-------------------	---------------------------------------

Military Service

since 06/1999	Member of Swiss Army Brass Band
07/1997 - 10/1997	Basic Military Service in Swiss Army Band

Skills

Languages	Swiss German, German, English, French
Operating Systems	Linux, Unix, Windows
Programming	C, C++, Fortran

Publications

An optimum time-stepping scheme for N-body simulations

Marcel Zemp, Joachim Stadel, Ben Moore and C. Marcella Carollo
submitted to MNRAS, preprint astro-ph/0606589 (2006) [174]

Multi-mass halo models

Marcel Zemp, Ben Moore, Joachim Stadel and C. Marcella Carollo
in preparation, to be submitted to MNRAS (2007)

Does the Fornax dwarf spheroidal have a central cusp or core?

Tobias Goerdt, Ben Moore, Justin Read, Joachim Stadel and Marcel Zemp
MNRAS, 368, 1073–1077 (2006) [64]

Globular clusters, satellite galaxies and stellar haloes from early dark matter peaks

Ben Moore, Jürg Diemand, Piero Madau, Marcel Zemp and Joachim Stadel
MNRAS, 368, 563–570 (2006) [115]

A universal velocity distribution of relaxed collisionless structures

Steen Hansen, Ben Moore, Marcel Zemp and Joachim Stadel
JCAP, 1, 14 (2006) [69]

Cusps in cold dark matter haloes

Jürg Diemand, Marcel Zemp, Ben Moore, Joachim Stadel and C. Marcella Carollo
MNRAS, 364, 665–673 (2005) [38]

The Stability of Dark Matter Cusps

Marcel Zemp
Diploma Thesis, ETH Zurich (2003) [173]

Acknowledgment

Many people have helped me a lot during this doctorate and deserve thanks. First, I would like to thank Marcella Carollo for giving me the possibility to write this thesis and her continuous and always encouraging support during the doctorate. Especially also for teaching me a lot about the physical background of my work. I owe also a lot to Ben Moore who was always an inspiring person and had the initial ideas that lead to this thesis project. It was always a big pleasure to discuss with him - whether about physics during the day or other important things in life during night with a beer not too far away! A very special thanks goes to Joachim Stadel. Without him this project would not have been possible. He helped me enormously with all the detailed daily work and explained to me all the parts of his baby, PKDGRAV. He also contributed to this work with some great ideas that pushed the project forward.

I would like to thank all my colleagues at both the Institute of Astronomy at ETH Zurich and the Institute of Theoretical Physics at the University of Zurich. I enjoyed the discussions and work with many of you. Among these, I would like to mention Sabine Schilling and Beat Tödtli who were my office mates at University and with whom I had many philosophical discussions, Peder Norberg and Christiano Porciani - my office mates at ETH when I started the thesis, Laure Fouchet, Lucio Mayer, Pawel Kampczyk and Martin Bernet who shared at some time an office with me at ETH, Mark Sargent with whom it was a pleasure to work together in many courses I was a teaching assistant, Alejandro Daleo, Jürg Diemand, Aaron Dutton, Tobias Goerdts, Steen Hansen, Tobias Huber, Tobias Kaufmann, Simon Lilly, Andrea Macciò, Daniel Maitre, Christoph Meier, Francesco Miniati, Justin Read, Prasenjit Saha and Simone Weinmann for many interesting scientific and probably even more not so scientific discussions, George Lake for accepting the job as a co-examiner of my thesis, and finally Doug Potter for keeping zBox1 and zBox2 alive. I had the pleasure to get to know many of you personally and not only as a scientific collaborator which I enjoyed very much during my doctorate!

I also would like to thank my friends from my band, Musikgesellschaft Risch-Rotkreuz, who share a great hobby with me. They gave me a lot of pleasure and a regular change from my scientific activity. During carnival, I also enjoyed a lot the musical activities with my friends from the Guggenmusik Oohregröbber. I always had a good time with you guys!

Finally, my last thanks goes to my family - Marianne, Jakob, Sandra and Karin - for their continuous support in my chosen way. Without your help many things would not have been possible!